Cold-atomic ensemble implemented as an efficient optical quantum memory layer in a cryptographic protocol

Hadriel Mamann

THÈSE DE DOCTORAT
DE SORBONNE UNIVERSITÉ

Spécialité : Physique

École doctorale n°564: Physique en Île-de-France

réalisée

au Laboratoire Kastler Brossel

sous la direction de Julien Laurat et Eleni Diamanti

présentée par

Hadriel MAMANN

Pour obtenir le grade de :

DOCTEUR DE SORBONNE UNIVERSITÉ

Sujet de la thèse :

Cold-atomic ensemble implemented as an efficient optical quantum memory layer in a cryptographic protocol

Soutenue publiquement le : 17 Mai 2024

Devant le jury composé de :

M.	**Hugues DE RIEDMATTEN**, Professor, ICFO	Rapporteur
M^{me}	**Virginia D'AURIA**, Professeure, Université de Nice Sophia Antipolis	Rapportrice
M^{me}	**Catherine SCHWOB**, Professeure, Sorbonne Université	Présidente du jury
M^{me}	**Rosa TUALLE-BROURI**, Professeure, Université Paris-Saclay	Examinatrice
M.	**Nicolas FABRE**, Maître de Conférences, Télécom Paris	Examinateur
M.	**Julien LAURAT**, Professeur, Sorbonne Université	Directeur de thèse
M^{me}	**Eleni DIAMANTI**, Directrice de Recherche CNRS, Sorbonne Université	Co-directrice

REMERCIEMENTS

Dans un premier temps, je tiens à remercier mon directeur de thèse Julien Laurat pour m'avoir accueilli dans son groupe, supervisé pendant ces années de doctorat avec bienveillance, confiance et encouragement pour atteindre nos objectifs. Merci de m'avoir envoyé aux quatre coins du monde pour présenter notre travail en conférence et me permettre de rencontrer les principaux acteurs de notre communauté. Ensuite, je remercie ma co-directrice Eleni Diamanti pour son encadrement et son investissement sur le projet de cryptographie. Ton aide m'a permis de mieux comprendre les détails du "Quantum money" et d'autres notions propres au domaine de la cryptographie. Merci à Alban Urvoy, membre permanent de l'équipe, pour le soutien quotidien qu'il nous a apporté sur la partie expérimentale. Tes précieux conseils ont été indispensables pour la réussite de l'expérience.

Je remercie également les membres du jury Hugues de Riedmatten, Virginia d'Auria, Catherine Schwob, Rosa Tualle-Brouri et Nicolas Fabre pour le temps qu'ils ont consacré à lire mon manuscrit et pour l'intérêt qu'ils ont porté à mon travail. Un grand merci à Hugues de s'être déplacé depuis Barcelone pour assister à la soutenance.

Je tiens à remercier spécialement Thomas Nieddu avec qui j'ai partagé la quasi-totalité de mon doctorat sur l'expérience. On a traversé ensemble cette aventure oscillant entre des moments de doute, de remise en question et des moments de joie intense. C'était un vrai plaisir de travailler ces années avec toi. Ensuite, je remercie chaleureusement Félix Garreau de Loubresse pour la motivation et la bonne humeur qu'il m'a transmise durant la deuxième partie de ma thèse. Merci de t'être occupé de l'organisation de la soutenance et de m'avoir tant gâté avec des cadeaux si bien choisis. Un grand merci à Félix Hoffet qui m'a appris à faire fonctionner l'expérience lorsque je suis arrivé dans le groupe. Je souhaite remercier Beate Asenbeck pour sa gentillesse et la bonne énergie qu'elle a mise dans l'équipe. On a vécu un sacré périple en conférence à San Francisco que je n'oublierai jamais. Merci à Jérémy Berroir pour l'ambiance incroyable qu'il mettait en salle de manip avec des musiques de hard rock et des chansons de Philippe Katerine. Je tiens à exprimer mes remerciements à Adrien Bouscal que je connaissais bien avant de rentrer en doctorat, et qui a toujours

été si gentil avec moi. Je remercie Tridib Ray, Anaïs Chochon, Ambroise Boyer, Jean-Gabriel Pipelin, Ioanna Katsavou, Priyanka Giri, Huazhuo Dong, Rayan Si Ahmed et Joachim Guyomard pour tous les bons moments qu'on a passés ensemble au laboratoire. Merci également à Mathieu Bozzio, responsable de la partie théorique de notre expérience de cryptographie, avec qui j'ai pu avoir de nombreux échanges très intéressants et instructifs sur la preuve de sécurité du protocole.

Je remercie toute l'administration du LKB, Stéphanie Dubois, David Noël, Laetitia Morel et Céline Le Helley pour l'accueil chaleureux qu'ils m'ont fait à mon arrivée et l'aide précieuse qu'ils m'ont apportée pour l'organisation des conférences. J'adresse mes sincères remerciements à Antoine Heidmann, directeur du laboratoire, pour son écoute, sa bienveillance et sa disponibilité.

À mes parents Laurence et Gil, je vous aime tant. Vous êtes des parents formidables, avec des qualités humaines exceptionnelles. Vous m'avez toujours soutenu dans mes projets, et je ne pourrais jamais exprimer à quel point je suis reconnaissant de vous avoir dans ma vie. À mon frère jumeau Aaron, tu es bien plus qu'un frère pour moi, tu es mon ami le plus proche, mon confident et mon complice de toujours. Nos chemins sont inséparables et je nous souhaite de vivre de belles aventures ensemble, main dans la main. Ensuite, je remercie infiniment mes grand-parents maternels, Cota et Henri, qui se sont occupés de moi depuis mon enfance et avec qui je partage des week-ends mémorables en famille. Un très grand merci à ma grand-mère paternelle Julie qui nous transmet constamment sa joie de vivre et son optimisme. Je remercie mes oncles Michel, Dan et Léon qui sont des grands frères à mes yeux. Enfin, j'ai une pensée pour mon grand-père Moshé qui nous a quitté trop tôt et qui veille sur nous de là-haut.

À la mémoire de mon grand-père Moshé Mamann

CONTENTS

LIST OF FIGURES

INTRODUCTION

Quantum information

Quantum information theory was developed between the 1980s and 1990s, with significant contributions from Richard Feynman on simulations of quantum mechanics problems with quantum computers [Feynman, 1982], and also from Peter Shor and Lov Grover with the development of quantum algorithms [Grover, 1996; Shor, 1994]. The fundamental unit of quantum information is the qubit (quantum bit). Classical bits are binary digits equal to 0 or 1 whereas qubits can exist in two states simultaneously (0 and 1) using a principle called quantum superposition. The qubit state can be written as $\alpha|0\rangle + \beta|1\rangle$ with α and β the amplitudes of $|0\rangle$ and $|1\rangle$ ($|\alpha|^2 + |\beta|^2 = 1$).

Another property of quantum mechanics is quantum entanglement. When two particles (A and B) become entangled, the state of particle A cannot be described independently of the state of particle B. One possible entangled state is:

$$|\Psi\rangle_{AB} = \frac{1}{\sqrt{2}}(|0\rangle_A|0\rangle_B + |1\rangle_A|1\rangle_B). \tag{1}$$

The above expression implies that if the particle A is measured in the state $|0\rangle$, B is also in $|0\rangle$ and if A is measured in the state $|1\rangle$, B is also in $|1\rangle$. More generally, the measurement of A instantly determines the state of B regardless of the distance between the two particles. The first experimental demonstration of this phenomenon was done in [Freedman and Clauser, 1972] with entangled photon pairs. However, Clauser and Freedman's measurement method had a loophole: the polarizers in their detection setup were adjusted before the emission of the photon pairs. Alain Aspect's team closed this loophole by changing randomly the direction of polarizers during the experiment [Aspect et al., 1982]. Fifteen years later, the group of Anton Zeilinger used entanglement to perform quantum teleportation between photons [Bouwmeester et al., 1997]. Entanglement plays a key role in quantum information science, including for quantum computing, quantum communication and sensing.

Quantum networks

Nowadays, optical fibers are used by telecommunication companies to transmit data over long distances. They enable high-speed and high-capacity communication, supporting the growing demand for broadband internet and multimedia services. The signals propagating inside optical fibers inevitably experience attenuation (typically 0.2 dB/km), leading to a decrease in the information rate received by the users. For example, we consider Alice and Bob separated by a fiber with a length $L = 1000$ km. If Alice sends data with a rate of 1 Gbit/s, Bob would receive 1 bit per 300 years. As a result, telecommunication companies are using repeaters to address this issue. Indeed, repeaters act as signal amplifiers in order to compensate for optical losses. However, this solution only works for classical communication. The amplification of one message encoded in classical bits is an operation that consists in creating many identical copies of the message. The no-cloning theorem [Wootters and Zurek, 1982] prevents this operation on quantum bits due to the fundamental principles of quantum mechanics.

The key idea to exchange quantum information is to establish entanglement between two nodes. One basic approach would be to create an entangled photon pair, send one photon from the pair to Alice and the other to Bob. Nevertheless, propagation losses in optical fibers reduce the creation of entanglement between the two ending nodes of the communication line. One solution is to divide this communication line into multiple segments and implement entangled photon pair sources (EPPS) in each segment. Photons are going to propagate on shorter distances (one segment's length instead of the whole line) and are thus less attenuated. In this case, entanglement has to be established between segments in order to be distributed between Alice and Bob.

Architectures of quantum networks relying on this method were proposed in [Briegel et al., 1998; Cirac et al., 1997]. One of them is presented in figure 0.1. An elementary segment can be composed of two EPPS, one Bell-state measurement platform (BSM) and two quantum memories (QMs) at the two ends of the segment (see figure 0.1(a)). We suppose that each EPPS creates two entangled photons described by the Bell state $|\Phi^+\rangle_{AB} = \frac{1}{\sqrt{2}}(|0\rangle_A|0\rangle_B + |1\rangle_A|1\rangle_B)$, the indices $\{\mathrm{A}, \mathrm{B}\}$ pointing the first or second photon of this entangled state. The global state of the two entangled pairs before the BSM is:

$$|\Psi\rangle = \frac{1}{2}(|0\rangle_A|0\rangle_B + |1\rangle_A|1\rangle_B) \otimes (|0\rangle_C|0\rangle_D + |1\rangle_C|1\rangle_D) \tag{2}$$

with $\otimes$ the Kronecker product, and the indices $\{\mathrm{C}, \mathrm{D}\}$ pointing the photons of the second pair. Photons A and D are stored in quantum memories while photons B and C are sent to the BSM. The Bell-state measurement consists in projecting the states of photons B and C on one of the four maximally entangled Bell states. In this

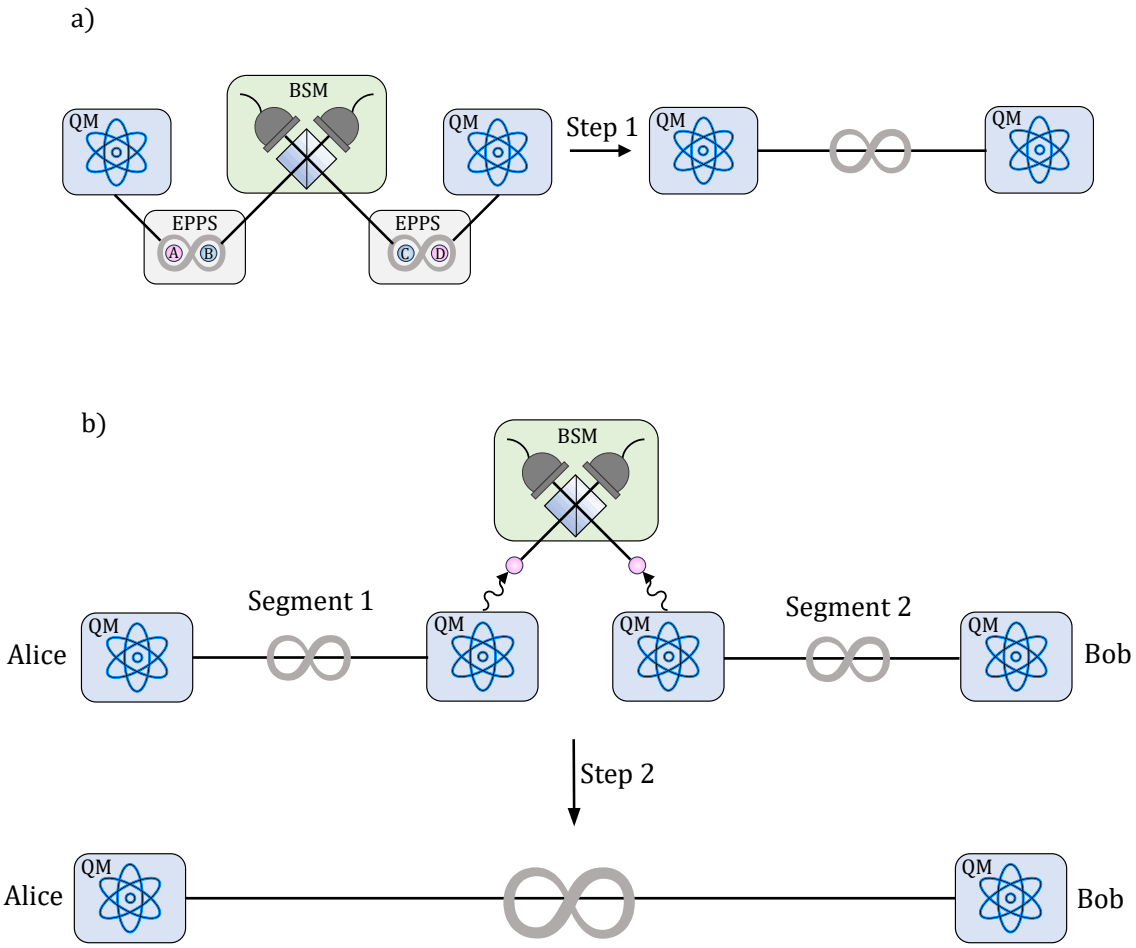

FIGURE 0.1: **Quantum network architecture.** *a*) An elementary segment is composed of two entangled photon pair sources (EPPS), one Bell-state measurement platform (BSM) and two quantum memories (QMs). One photon of each entangled pair is stored in a QM while the other is sent to the BSM. The Bell-state measurement heralds the entanglement of the two QMs located at the segment ends (Step 1). *b*) We consider a communication line composed of two segments for simplification. Assuming that one segment succeeds step 1 before the other, the entanglement is stored in the quantum memories until both achieve it. When it is the case, a BSM is performed between the adjacent QMs of the two segments to distribute entanglement between Alice and Bob (Step 2). The purpose of quantum memories in this architecture is thus to synchronize segments with each other.

example, we assume the BSM is projecting on $|\Phi^+\rangle_{BC} = \frac{1}{\sqrt{2}}(|0\rangle_B|0\rangle_C + |1\rangle_B|1\rangle_C)$. The resulting state after projection of $|\Psi\rangle$ on $|\Phi^+\rangle_{BC}$ is:

$$|\Psi\rangle = \frac{1}{\sqrt{2}}(|0\rangle_A|0\rangle_D + |1\rangle_A|1\rangle_D). \tag{3}$$

As the photons A and D were stored in the quantum memories, the expression (3) shows the entanglement of two QMs heralded by the BSM (Step 1 in figure 0.1(a)). The second step is to distribute entanglement between segments. However, there is a low probability that all segments succeed step 1 at the same time as the EPPS are probabilistic sources in practice. The purpose of quantum memories in this architecture is to synchronize segments with each other. Figure 0.1(b) illustrates the example of a communication line composed of two segments for simplification. Assuming that one of them succeeds the first step before the other, entanglement is stored in the quantum memories until both achieve it. When it is the case, a BSM is performed between the adjacent QMs of the two segments to distribute entanglement between Alice and Bob (Step 2). Step 1 and step 2 are called entanglement swapping operations. The required time to establish entanglement between the ends of the line is polynomial in the number of elementary segments with quantum memories instead of exponential without them.

Quantum memories can be used in different contexts than quantum repeaters: for instance, they can be implemented as a memory layer in a cryptographic protocol. However, experimental demonstrations combining these synchronization devices with cryptographic protocols are lacking due to the very demanding constraints in terms of memory efficiency and fidelity to operate in a secure regime. The goal of my work is to perform such a demonstration.

Context

After my master thesis done at the Cavendish Laboratory on semiconductor quantum dots, I decided to change platforms and move to cold atoms. I joined Julien Laurat's group at Laboratoire Kastler-Brossel in October 2020 with the aim of acquiring experimental and theoretical knowledge about cold-atomic quantum memories. When I arrived in the group, a highly efficient memory was recently demonstrated and an important goal was now to use it as a memory layer in a cryptographic protocol. At that time, Thomas Nieddu was a post-doctoral fellow and Felix Hoffet was a PhD student. They taught me how to run the experiment on a daily basis. The implementation of the cryptographic protocol was just starting but modifications on the experimental setup had to be done to improve its performances. These critical improvements were time-consuming to implement (one full year) but they were needed to meet the requirements of the protocol. In this project, we collaborated closely with Mathieu Bozzio, who developed the security analysis of the quantum money during his PhD in Eleni Diamanti's group. We are currently writing a paper together about

the implementation of this cryptographic protocol using our cold-atom-based quantum memory. In parallel, another project was to spatially multiplex the memory with Hermite-Gaussian modes of light in order to store many qubits at the same time. Experimental demonstration of multiplexing could not be done due to time constraints. However, we performed numerical simulations to evaluate the multimode capacity of our storage platform and found the optimal parameters to maximize this capacity.

In addition to my doctoral research, I was teaching during two years at Sorbonne Université to third-year bachelor students. My mission includes tutorials in electromagnetism (electric and magnetic dipoles, dipole radiation) and practical works in optics and electronics (Michelson interferometer, laser diodes, electronic filters). I had the opportunity to write tutorial and exam subjects for some teaching modules.

Outline

Chapter 1
The first chapter gives an overview of the main storage platforms with the key parameters to benchmark their performances. The storage-and-retrieval process is studied in the case of EIT-based quantum memories with an analysis of their decoherence sources. The trapping and cooling methods employed to obtain our cold-atomic ensemble are discussed at the end of the chapter.

Chapter 2
The second chapter introduces the implementation of our quantum memory based on cold atoms. The magneto-optical trap is presented with the cooling lasers and the new coils generating large magnetic-field gradients. The locking methods of the signal and control lasers are detailed. The optimization procedures for the memory efficiency and lifetime are specified, with a new system compensating for the residual magnetic field. Additional apparatus (glass chamber, dispensers and detection setup) are discussed at the end of the chapter.

Chapter 3
The third chapter focuses on the use of quantum memories in crytographic protocols. The quantum money protocol is explained with its security analysis in the presence of noise and storage losses. The experimental setup is presented with specific details on the generation of random polarization states and the optimization of their fidelity. This chapter reports the first demonstration of the unforgeable quantum money including an intermediate quantum memory layer, taking advantage of our high-efficiency and low-noise storage platform.

Chapter 4
The fourth chapter is about the study of spatial multiplexing. Two multiplexing

methods are considered: a combination of spatially-superposed Hermite-Gaussian beams and a 2D array of Gaussian beams addressing different micro-ensembles of the cloud. The multimode capacity of our quantum memory is simulated for these two techniques and the optimal parameters to maximize it are provided.

CHAPTER 1

THEORETICAL DESCRIPTION OF QUANTUM MEMORIES AND COLD ATOMS

Contents

Quantum memories are devices capable of storing and retrieving quantum information. The figures of merit to evaluate their performances are listed with an overview

of the main storage platforms used in the community and their specific advantages. We then focus on the understanding of the mechanisms involved in the storage-and-retrieval process for EIT-based quantum memories. The efficiency and the decoherence of this process are part of the analysis. This chapter concludes with a detailed description of the cooling and trapping methods that enable the preparation of our cold atomic ensemble.

1.1 Quantum memories

In our study, we only consider optical quantum memories, i.e. physical systems storing and retrieving quantum information carried by light. The performances of quantum memories can be evaluated by several key parameters: the memory efficiency, lifetime, fidelity and multimode capacity. These figures of merit enable the comparison between memories based on different platforms.

1.1.1 Key parameters of quantum memories

The following parameters are the main figure of merits to evaluate the performances of quantum memories.

Memory efficiency

An input light pulse is sent to the quantum memory with an energy $\mathcal{E}_{\text{in}}$. This pulse is stored inside the memory and retrieved after a defined storage time. The output pulse leaves the memory with an energy $\mathcal{E}_{\text{out}}$. The storage-and-retrieval efficiency is defined as[1]:

$$\eta = \frac{\mathcal{E}_{\text{out}}}{\mathcal{E}_{\text{in}}}. \tag{1.1}$$

In the context of quantum networks, entanglement is stored in quantum memories and retrieved later to synchronize repeater segments between each others [Kimble, 2008]. The entanglement rate between the two ends of a communication line highly depends on η as the memory efficiency affects the rate of entanglement swapping operations. The impact of η on the scalability of quantum networks is thoroughly discussed in [Sangouard et al., 2011]. Moreover, achieving a high memory efficiency enables a range of cryptographic protocols to operate in the secure regime as losses introduced by the memory can be exploited by malicious parties. This last point is deeply detailed in Chapter 3.

Conditional fidelity

The fidelity evaluates the overlap between the input and detected output states. In mathematical terms, if the input state $|\Psi_{\text{in}}\rangle$ and output state $|\Psi_{\text{out}}\rangle$ are pure states, the fidelity can be easily calculated with the expression $\mathcal{F} = |\langle\Psi_{\text{in}}|\Psi_{\text{out}}\rangle|^2$. In the

[1] This efficiency can also be divided in two steps: the storage efficiency η_s and the retrieval efficiency η_r, which leads to an overall efficiency $\eta = \eta_s\eta_r$.

general case of mixed states, the input pulse is described by a density matrix $\hat{\rho}_{\text{in}}$ and the output pulse by a density matrix $\hat{\rho}_{\text{out}}$. The fidelity is thus defined as:

$$\mathcal{F} = \text{Tr}\left(\sqrt{\sqrt{\hat{\rho}_{\text{in}}}\hat{\rho}_{\text{out}}\sqrt{\hat{\rho}_{\text{in}}}}\right)^2. \tag{1.2}$$

The square roots of these matrices exist as they are positive semidefinite matrices. The fidelity is equal to 1 if the output state is the same as the input one and equal to 0 if the two states are orthogonal. This figure of merit can also separate the classical memories from the quantum memories. Indeed, if the input state contains N photons, [Massar and Popescu, 1995] demonstrated that the classical limit is $(N+1)/(N+2)$, leading to 2/3 in the case of a single photon.

Memory lifetime

The memory efficiency decreases with storage time due to decoherence mechanisms (the decoherence sources in our experiment are specified in 1.2.4). The lifetime τ of a quantum memory can be defined as the storage time for which the memory efficiency drops at $1/e \approx 37\%$ of its initial value. In a quantum network, the lifetime of quantum memories should at least be equal to the propagation time of light along the entire communication line. Therefore, τ should be at least on the order of ten milliseconds to perform quantum communication between nodes separated by a thousand kilometers.

Multimode capacity

As for classical communication, multiplexing is useful for the field of quantum communication. A critical challenge is to go beyond single-mode quantum memories. The aim is to store many modes at the same time. It could be used to improve the achievable rates for creating entanglement between light and quantum memories in a quantum network, as it is equivalent to running the protocol described in figure 0.1 for each mode in parallel. Several multiplexing methods can be explored depending on the degree of freedoms available for a specific storage platform, such as multiplexing in time, frequency, and space. The multimode capacity characterises the number of modes that a memory can store-and-retrieve with a high efficiency ($\eta > 50\,\%$ for instance). Numerical simulations of this multimode capacity for our cold-atom based quantum memory are presented in Chapter 4 of this manuscript.

These are the most important figures of merits to benchmark the performances of quantum memories. Other additional parameters may be taken into account including the ability to retrieve information on-demand as it is required in order to synchronize elementary links in a quantum network. Another important parameter is the memory bandwidth which determines the smallest pulse duration that the memory can store.

1.1.2 Presentation of the main memory platforms

The quantum memory field is quite diversified in terms of memory platforms. The following paragraphs introduce the main storage media with their associated protocols, and an assessment of their performance based on the criteria outlined in the previous section.

Cold atomic ensembles

Cold atomic ensembles are atomic gases that have been cooled to temperatures typically on the order of microkelvins. They are manipulated in vacuum chambers (pressure around 10^{-10} Torr) and prepared using laser cooling in magneto-optical traps. The cold atomic ensembles considered in this study are composed of alkali atoms (mostly cesium and rubidium). The protocols mainly employed for quantum memories based on cold atoms are the EIT and DLCZ schemes. Memories using DLCZ scheme are called "emissive" as they are used to generate single photons on-demand with a good retrieval efficiency whereas EIT based quantum memories are called "absorptive" as they are used to store-and-retrieve externally generated quantum states.

Electromagnetically induced transparency (EIT) is a phenomenon first observed in [Boller et al., 1991]. A light pulse (named the signal) can propagate through an atomic ensemble without being absorbed thanks to a bright additional laser (called the control beam) that opens a transparency window in the medium. The signal inside the ensemble is slow down (slow light) and cannot be considered only as photonic state but a dark state polariton [Fleischhauer and Lukin, 2000] which is a superposition between a photonic state and a collective atomic state. By turning off and on the control beam, one can store and retrieve the signal pulse (see section 1.2.3). This dynamical-EIT was implemented for the first time in [Liu et al., 2001].

The main benefit of EIT cold-atom based quantum memories are their storage-and-retrieval efficiencies which are the highest achieved among all the memory platforms: it could reach about 90% [Cao et al., 2020; Wang et al., 2019] as demonstrated in our group. The lifetime of such a memory can be optimized with an optical lattice to avoid motional dephasing, clock transitions to be insensitive to residual magnetic field and the application of a magic-valued magnetic field to reduce the differential light shift induced by the lattice (see section 1.2.4). 16 s lifetime was reached [Dudin et al., 2013] for bright pulses after application of these three improvements. Moreover, the intrinsic fidelity of these memories can attain 99.5% [Vernaz-Gris et al., 2018]. The EIT scheme is compatible with spatial multiplexing (see Chapter 4) as [Jiang et al., 2019] demonstrated by addressing 210 different memory cells. Temporal multiplexing is not compatible with EIT scheme due to the control field that cannot store an excitation without reading the previous one. Variations of this scheme relying on large B-field gradients enable to use the temporal degree of freedom.

The DLCZ scheme was proposed by Duan, Lukin, Cirac and Zoller in [Duan et al., 2001]. It consists in sending a write pulse to the ensemble to create an excitation (not driven by any additional bright beam as for the EIT protocol). The excitation is heralded as it releases a photon which is detected. After a controllable time, the read pulse is sent to the atomic medium and converts this excitation into a single photon leaving the ensemble in a direction given by the phase matching conditions of this four-wave mixing process. DLCZ was implemented in our experiment [Cao et al., 2020] as a single photon source, in the low excitation regime to suppress the two-photon component.

In terms of performances, cold-atom groups working with DLCZ scheme achieved spatial multiplexing such as [Pu et al., 2017] who addressed up to 225 accessible memory cells. 100 ms lifetime has been reported in [Wang et al., 2021] by implementing an optical lattice and clock transitions. The only efficiency which can be evaluated for these emissive memories is the retrieval one, which can attain 50 % in free space [Laurat et al., 2006] and 84 % in a cavity system [Simon et al., 2007] (albeit inside the cavity mode).

Warm atomic vapors

Warm atomic vapors are atomic ensembles at room temperature contained in glass cells. Unlike cold atomic ensembles, they do not require vacuum systems or laser cooling apparatus but only a resistance wire coiled around the cell to heat up the gas above its melting point (28.5°C for cesium and 39°C for rubidium). The room-temperature memories presented are only composed of alkali atoms. The protocols mainly employed for warm atomic vapors are Raman-EIT and Raman-DLCZ schemes.

The Raman-EIT scheme can be described as an EIT far-detuned from resonance in order to avoid the Doppler broadening. Therefore, the power of the control beam must be much higher than in the resonant case leading to an important noise added by the control light. Moreover, the two fields must be colinear in order to have a decent lifetime as the motional dephasing increases with the temperature of atoms (see section 1.2.4). However the benefit of these warm atomic memories is their high bandwidth which enables to store pulses with temporal length under the nanosecond. The first implementation of this Raman scheme was done in [Reim et al., 2010] with 300 ps pulses. The memory efficiency achieved for these system is up to 67% using a cavity [Ma et al., 2022] with a microsecond lifetime. Some demonstrations pushed the fidelity to 97% [England et al., 2012].

The Raman-DLCZ scheme is similar to DLCZ scheme with electromagnetic fields far-detuned from resonance in order to avoid the Doppler broadening. The write and read pulses must also be colinear to suppress the motional dephasing. Therefore multiple filtering cavities need to be implemented to filter out the read pulse from the single photons. Retrieval efficiencies up to 70 % have been reported with a 0.89

ms lifetime [Dideriksen et al., 2021].

Rare-earth doped crystals

Rare-earth doped crystals are materials that have been doped with rare-earth ions, i.e. elements from the lanthanide series of the periodic table. Rare-earth doped crystals were at the center of interest because of their 4f–4f intra-shell transitions that are isolated from the crystalline environment due to screening effect [Macfarlane, 2002]. Most groups work with these crystals at cryogenic temperatures to improve their coherence time. The protocol mainly employed for rare-earth ions is AFC.

The AFC (atomic frequency comb) scheme was first proposed in [Afzelius et al., 2009] and experimentally implemented in [Afzelius et al., 2010]. This method takes advantage of an inhomogeneous broadening absorption profile to create a spectral comb with periodic and highly absorptive peaks. Indeed, the atoms in the ground state are optically pumped to an auxiliary state to obtain absorption peaks spaced by a frequency Δ. When the frequency comb is set, the input light pulse drives the atoms to an excited state. The excitation will dephase due to the multiple frequencies of the comb and rephase after a pre-programmed delay $2\pi/\Delta$ resulting in a photon-echo emission. As a result, memories using AFC with two levels do not have the ability to retrieve information on-demand which limits their applications: they cannot be used as synchronization devices in quantum networks. A three-level system is required in order to achieve on-demand retrieval. In this case, an additional control beam is sent to the crystal to drive the atoms from the excited state to a long-lived spin state.

The maximum efficiency reached for rare-earth doped crystals using two-level AFC is 62% in a cavity [Duranti et al., 2023] with 95% fidelity. This is the highest memory efficiency in the quantum regime among all solid state devices. Then, storage in the spin state (on-demand memory) is less efficient: 12% in [Jobez et al., 2014]. 20 ms lifetime was demonstrated [Ortu et al., 2022] in the quantum regime (with single photons) using decoupling sequences to suppress decoherence of the spin wave. The main advantage of these AFC-based memories is their multimode capacity as they are compatible with frequency, temporal and spatial multiplexing. Temporal multiplexing was implemented with 62 modes in [Lago-Rivera et al., 2021] and 100 modes for [Jobez et al., 2016] with pre-programmed delay but also on-demand with 50 modes. Temporal and frequency multiplexing combined were achieved in [Seri et al., 2019] with 15 spectral modes and 9 temporal modes (135 modes in total).

1.2 EIT-based quantum memories

In this section, we focus on quantum memories based on atomic ensembles using EIT. We consider atoms in a gaz which are not interacting. Optical quantum memories rely on the information transfer between photons and atoms. In order to optimize

the efficiency of this transfer, we need to understand the physical mechanisms involved in the memory process.

1.2.1 Classical description of light-matter interaction

The first element to consider in order to achieve a high storage efficiency is the absorptive properties of the medium. This absorption process can be simply described in the classical regime, providing an introduction to the concept of optical depth.

Susceptibility of an atomic medium

We take the simplified picture of an atom composed of one single electron and a nucleus. The electron motion is modeled as a damped harmonic oscillator with a oscillation frequency ω_0 and a damping coefficient Γ. The electron motion is modified by the presence of an external electric field $\vec{E} = \vec{E}_0 e^{-i\omega t}$ according to the following equation:

$$\frac{d^2\vec{r}}{dt^2} + \Gamma\frac{d\vec{r}}{dt} + \omega_0^2\vec{r} = \frac{q\vec{E}_0}{m}e^{-i\omega t} \tag{1.3}$$

with $\vec{r}$ the electron position around the nucleus, q its charge and m is mass. This equation can be solved in the steady state regime leading to the expression:

$$\vec{r}_0 = \frac{q\vec{E}_0}{m}\frac{1}{\omega_0^2 - \omega^2 - i\Gamma\omega}. \tag{1.4}$$

As the dipolar moment of the electron is equal to $\vec{d_0} = q\vec{r}_0 = \epsilon_0\alpha\vec{E}_0$ with ϵ_0 the electric permittivity of vacuum, we can deduce the atom polarizability α. The polarizability α is a microscopic quantity whereas the susceptibility χ is a macroscopic quantity. As a reminder, we consider atoms in a gaz which are not interacting between each others (the density of atoms $\mathcal{N}$ is low). In this particular case, the relation between χ and α can be simplified to $\chi = \mathcal{N}\alpha$:

$$\chi = \mathcal{N}\frac{q^2}{m\epsilon_0}\frac{1}{\omega_0^2 - \omega^2 - i\Gamma\omega}. \tag{1.5}$$

Optical depth of an atomic medium

We consider light as a plane wave propagating along the z-axis. Its electric field is described by: $\vec{E}(z,t) = \vec{E}_0 e^{-i\omega t + ikz}$ with k the wavevector, n the complex refractive index of the medium. The refractive index is determined by the susceptibility χ: $n = (1+\chi)^{1/2}$ with $\chi = \mathrm{Re}(\chi) + i\,\mathrm{Im}(\chi)$. As the atomic density is low, we can consider $\mathrm{Re}(\chi) \ll 1$ and $\mathrm{Im}(\chi) \ll 1$, and expand the refractive index at the first order:

$$n \approx 1 + \frac{1}{2}\mathrm{Re}(\chi) + \frac{i}{2}\mathrm{Im}(\chi). \tag{1.6}$$

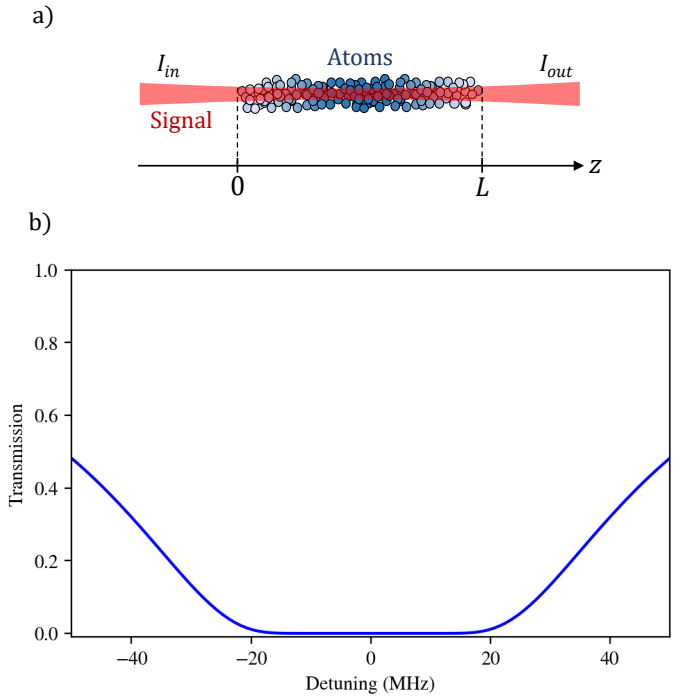

FIGURE 1.1: **Transmission of a light beam through an atomic cloud.** *a*) A light beam (the signal) propagates along the z-axis through an atomic medium. I_{in} represents the intensity before interacting with the atoms ($z < 0$) and I_{out} after propagation in an atomic medium ($z > L$). *b*) The transmission factor ($T = I_{\text{out}}/I_{\text{in}}$) is calculated for a range of detunings around the resonance. This curve corresponds to an optical depth on resonance equal to 350 for $\Gamma = 2\pi \cdot 4.575$ GHz (Cesium D1 line).

The imaginary part of the susceptibility can be calculated thanks to equation (1.5). We can make the approximation $\omega_0^2 - \omega^2 \approx 2\omega_0(\omega_0 - \omega)$ as we assume the frequency of light is close to the atomic resonance. It leads to the following result:

$$\text{Im}(\chi) = \mathcal{N}\frac{q^2}{m\epsilon_0}\frac{\Gamma\omega}{4\omega_0^2(\omega_0-\omega)^2 + \Gamma^2\omega^2}. \tag{1.7}$$

The intensity of the plane wave inside the atomic cloud can be expressed as $I(z) = |\vec{E}(z,t)\cdot\vec{e}_z|^2 = I_0 e^{-\text{Im}(\chi)kz}$. As it is shown in figure 1.1(a), I_{in} represents the intensity before interacting with the atoms ($z < 0$) and I_{out} after propagation in an atomic medium ($z > L$). The transmission factor T is thus equal to:

$$T(\delta) = \frac{I_{\text{out}}(\delta)}{I_{\text{in}}(\delta)} = \exp(-\text{Im}(\chi)kL) \tag{1.8}$$

$$= \exp(-\frac{d_0}{1+4(\frac{\delta}{\Gamma})^2}) \tag{1.9}$$

with d_0 the optical depth at resonance of the medium and $\delta = \omega_0 - \omega$ the detuning of the light frequency from the resonance. The optical depth (OD) is a key parameter for quantum memories as high values of OD enable high storage efficiencies. The OD

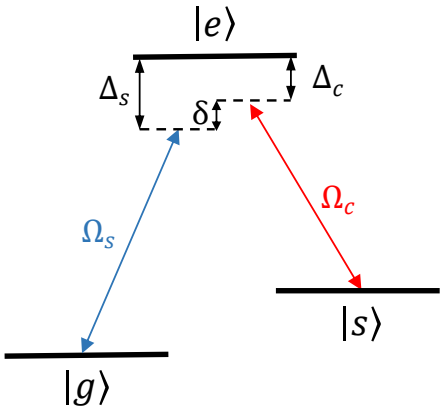

FIGURE 1.2: **EIT in a three-level system with a lambda configuration.** $|g\rangle$ is the ground state, $|s\rangle$ is a long-lived spin state, and $|e\rangle$ the excited state . The transition frequencies are noted ω_{sg}, ω_{eg} and ω_{es}. The Rabi frequencies associated to the signal and control fields are respectively Ω_s and Ω_c. The signal field is detuned from the transition $|g\rangle \rightarrow |e\rangle$ by Δ_s and the control field is detuned from the transition $|s\rangle \rightarrow |e\rangle$ by Δ_c. The two-photon detuning δ is equal to the difference $\Delta_s - \Delta_c$.

reflects the absorption capacity of the cloud. d_0 can be determined by measuring the transmission factor thanks to the equation (1.9). Figure 1.1(b) represents the transmission for a range of detunings around the resonance. This curve corresponds to an optical depth on resonance equal to 350 for $\Gamma = 2\pi \cdot 4.575$ GHz (Cesium D1 line [Steck, 1998]).

1.2.2 EIT for three-level systems in the semi-classical regime

The storage process does not only rely on the signal absorption as atoms would be transferred from the ground state to a short-lived excited level. An additional field (called the control) is required to drive the transition to a third level: a long-lived spin state. This additional classical light modifies the dispersion and transmission properties of the atomic ensemble at the signal wavelength. This section is a comprehensive study of these properties in the semi-classical regime.

Lindblad master equation

We consider a three-level system in a lambda configuration (see figure 1.2) involving one ground state $|g\rangle$, a long-lived spin state $|s\rangle$, and an excited state $|e\rangle$. The transition frequencies are noted ω_{sg}, ω_{eg} and ω_{es}. The signal field is modelled by $\vec{E}_s = \vec{E}_{0s}\cos(\omega_s t)$ and the control field by $\vec{E}_c = \vec{E}_{0c}\cos(\omega_c t)$. Their respective Rabi frequencies are $\Omega_s = \vec{d}_{ge} \cdot \vec{E}_{0s}/\hbar$ and $\Omega_c = \vec{d}_{se} \cdot \vec{E}_{0c}/\hbar$ ($\vec{d}_{ge}$ and $\vec{d}_{se}$ being the electric dipole moment of the two transitions). The signal field is detuned from the transition $|g\rangle \rightarrow |e\rangle$ by $\Delta_s = \omega_s - \omega_{eg}$ and the control field is detuned from the transition

$|s\rangle \rightarrow |e\rangle$ by $\Delta_c = \omega_c - \omega_{es}$. The two-photon detuning δ indicated in figure 1.2 is equal to the difference $\Delta_s - \Delta_c$.

The semi-classical approach consists in the quantization of the atomic levels with classical light (the electromagnetic fields are not quantized). Therefore the Hamiltonian of our system $\hat{H}$ can be decomposed in two different terms: $\hat{H}_{\text{at}}$ representing the atomic internal levels and $\hat{H}_{\text{int}}$ the interaction between the atomic levels and the electromagnetic fields ($\hat{H}^s_{\text{int}}$ is for the signal field and $\hat{H}^c_{\text{int}}$ is for the control field). They can be expressed as:

$$\hat{H} = \hat{H}_{\text{at}} + \hat{H}^s_{\text{int}} + \hat{H}^c_{\text{int}} \tag{1.10}$$

$$\hat{H}_{\text{at}} = \hbar\omega_{eg}|e\rangle\langle e| + \hbar\omega_{sg}|s\rangle\langle s| \tag{1.11}$$

$$\hat{H}^s_{\text{int}} = -\hbar\Omega_s \cos(\omega_s t)(|e\rangle\langle g| + |g\rangle\langle e|) \tag{1.12}$$

$$\hat{H}^c_{\text{int}} = -\hbar\Omega_c \cos(\omega_c t)(|e\rangle\langle s| + |s\rangle\langle e|). \tag{1.13}$$

$\hat{\rho}$ is the density matrix of our system. Its evolution is given by the Lindblad master equation:

$$\frac{d\hat{\rho}}{dt} = \frac{i}{\hbar}[\hat{\rho}, \hat{H}] + \hat{\mathcal{L}}(\hat{\rho}) \tag{1.14}$$

with the Lindbladian

$$\hat{\mathcal{L}}(\hat{\rho}) = \sum_j \gamma_j (\hat{\sigma}_j \hat{\rho} \hat{\sigma}_j^\dagger - \frac{1}{2}\{\hat{\sigma}_j^\dagger \hat{\sigma}_j \hat{\rho}\}) \tag{1.15}$$

where γ_j are the decay rates of the transition considered and $\hat{\sigma}_j$ is the corresponding Linblad operators. The square brackets are the commutator $[a, b] = ab - ba$ and the curly ones are the anti-commutator $\{a, b\} = ab + ba$. The Lindbladian operator represents the relaxation term coming from the spontaneous emission. There are three decay paths in our lambda scheme: two from the excited state ($|e\rangle \rightarrow |g\rangle$ and $|e\rangle \rightarrow |s\rangle$) with a global decay rate γ_e and one from the long lived spin state ($|s\rangle \rightarrow |g\rangle$) at a rate γ_s. The Linblad operators corresponding to these decay channels are $\hat{\sigma}_{ge} = |g\rangle\langle e|$, $\hat{\sigma}_{se} = |s\rangle\langle e|$ and $\hat{\sigma}_{gs} = |g\rangle\langle s|$.

Expansion to first order perturbation series

In order to solve the master equation, we are going to expand it in perturbation series at the first order on the parameter $\epsilon = \Omega_s/\Omega_c$. Indeed, the amplitude of the signal field is very small compared to the control field in practice (the signal is typically at the photon level whereas the control power is on the order of milliwatts). The density matrix is noted $\hat{\rho} = \hat{\rho}^{(0)} + \hat{\rho}^{(1)}$ where $\hat{\rho}^{(0)}$ does not depend on ϵ (zero-th order term) and $\hat{\rho}^{(1)}$ scales linearly with ϵ (first order term). Initially, all the atoms are in the ground state $|g\rangle$ ($\rho^{(0)}_{gg} = 1$, $\rho^{(0)}_{ee} = \rho^{(0)}_{ss} = 0$) and all the coherence terms

(non-diagonal elements of the density matrix) are equal to zero. To the first order, equation (1.14) can be written:

$$\frac{d\hat{\rho}^{(1)}}{dt} = \frac{i}{\hbar}[\hat{\rho}^{(1)}, \hat{H}_{\text{at}} + \hat{H}^{c}_{\text{int}}] + \frac{i}{\hbar}[\hat{\rho}^{(0)}, \hat{H}^{s}_{\text{int}}] + \hat{\mathcal{L}}(\hat{\rho}^{(1)}) \tag{1.16}$$

The Hamiltonians $\hat{H}_{\text{at}}$ and $\hat{H}^{c}_{\text{int}}$ are zero-th order terms whereas $\hat{H}^{s}_{\text{int}}$ is a first order term. The aim would be to determine the density matrix elements required to calculate the susceptibility of the medium seen by the signal field. The only element we need is $\rho^{(1)}_{eg}$ as the susceptibility is proportional to this non-diagonal term according to the relation (1.24). After extracting $\rho^{(1)}_{eg}$ from equation (1.16), we obtain:

$$\frac{d\rho^{(1)}_{eg}}{dt} = -(i\omega_{eg} + \gamma_{ge})\rho^{(1)}_{eg} + i\Omega_c \cos(\omega_c t)\rho^{(1)}_{sg} + i\Omega_s \cos(\omega_s t)\rho^{(0)}_{gg} \tag{1.17}$$

with $\gamma_{ge} = \gamma_e/2$ the relaxation rate of the coherence between the states $|g\rangle$ and $|e\rangle$. In order to solve equation (1.17), $\rho^{(1)}_{sg}$ has to be calculated. After projecting equation (1.16), we obtain:

$$\frac{d\rho^{(1)}_{sg}}{dt} = -(i\omega_{sg} + \gamma_{gs})\rho^{(1)}_{sg} + i\Omega_c \cos(\omega_c t)\rho^{(1)}_{eg} \tag{1.18}$$

with $\gamma_{gs} = \gamma_s/2$ the relaxation rate of the coherence between the states $|g\rangle$ and $|s\rangle$. The next step consists in writing the density matrix elements in the rotating frame of the electromagnetic fields in order to simplify the calculations. The density matrix elements in the new rotating frame are:

$$\tilde{\rho}_{eg} = \rho_{eg} e^{i\omega_s t} \quad , \quad \tilde{\rho}_{sg} = \rho_{sg} e^{i(\omega_s - \omega_c)t}. \tag{1.19}$$

After writing the two differential equations (1.17) and (1.18) in the new frame, terms oscillating at the frequency $2\omega_c$ and $2\omega_s$ appear. The rotating wave approximation (RWA) consists in neglecting these high frequency terms as they will average to zero on the timescale considered. In other words, the variation of the density matrix elements is assumed be slow compared to the electromagnetic field oscillation. This approximation leads to:

$$\frac{d\tilde{\rho}^{(1)}_{eg}}{dt} = (i\Delta_s - \gamma_{ge})\tilde{\rho}^{(1)}_{eg} + \frac{i}{2}\Omega_c \tilde{\rho}^{(1)}_{sg} + \frac{i}{2}\Omega_s \rho^{(0)}_{gg} \tag{1.20}$$

$$\frac{d\tilde{\rho}^{(1)}_{sg}}{dt} = (i\delta - \gamma_{gs})\tilde{\rho}^{(1)}_{sg} + \frac{i}{2}\Omega_c \tilde{\rho}^{(1)}_{eg}. \tag{1.21}$$

In steady-state, equations (1.20) and (1.21) give access to the expressions of $\tilde{\rho}^{(1)}_{sg}$ and more importantly $\tilde{\rho}^{(1)}_{eg}$:

$$\tilde{\rho}^{(1)}_{sg} = \frac{\Omega_c \Omega_s}{4(i\gamma_{gs} + \delta)(i\gamma_{ge} + \Delta_s) - \Omega_c^2} \rho^{(0)}_{gg} \tag{1.22}$$

$$\tilde{\rho}^{(1)}_{eg} = -\frac{2\Omega_s(i\gamma_{gs} + \delta)}{4(i\gamma_{gs} + \delta)(i\gamma_{ge} + \Delta_s) - \Omega_c^2} \rho^{(0)}_{gg}. \tag{1.23}$$

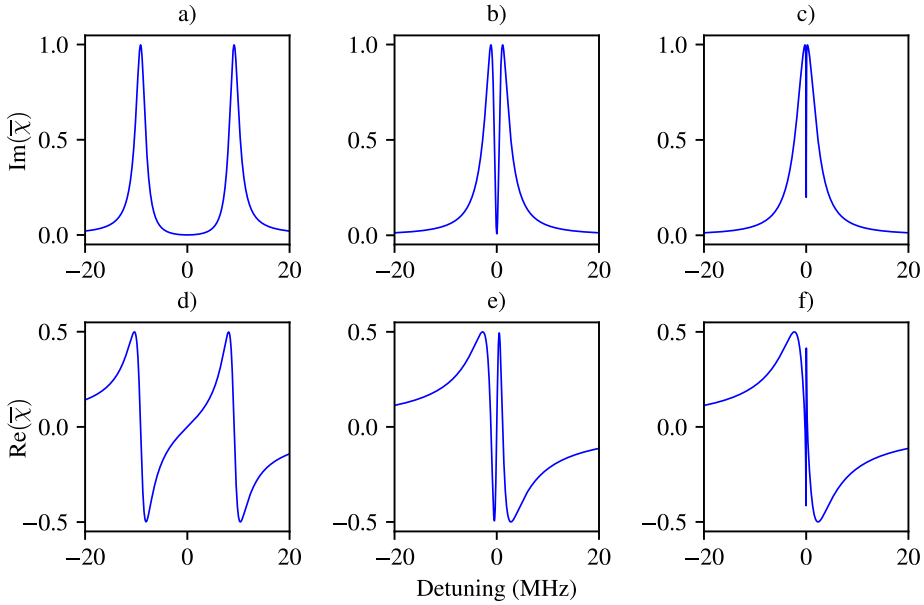

FIGURE 1.3: **Imaginary and real parts of the normalized susceptibility as a function of the signal detuning with a resonant control field for different Rabi frequencies.** The imaginary part of the susceptibility represents the absorption properties of the atomic medium whereas the real part is showing its dispersion. The relaxation rate of the coherence between the ground and spin states was chosen to be $\gamma_{gs} = 10^{-3}\Gamma$. The Rabi frequency of the resonant control field is different for each column: $\Omega_c = 4\Gamma$ for *a*) and *d*), $\Omega_c = \Gamma/2$ for *b*) and *e*) and $\Omega_c = \Gamma/10$ for *c*) and *f*). We note Γ the linewidth of the Cesium D1 line ($\Gamma = 4.575\,\mathrm{MHz}$).

Susceptibility in a three-level system

We can deduce from the result (1.23) the linear susceptibility at the signal wavelength:

$$\chi(\Delta_s, \Delta_c) = 2\mathcal{N}\frac{d_{eg}}{\epsilon_0 E_{0s}}\tilde{\rho}_{eg}^{(1)} \tag{1.24}$$

$$\chi(\Delta_s, \Delta_c) = -\frac{d_0\gamma_{ge}}{k_s L}\frac{(i\gamma_{gs}+\delta)}{(i\gamma_{gs}+\Delta_s-\Delta_c)(i\gamma_{ge}+\Delta_s)-\Omega_c^2/4} \tag{1.25}$$

with the optical depth on resonance $d_0 = \frac{k_s L\mathcal{N}d_{eg}^2}{\epsilon_0\hbar\gamma_{ge}}$, L the length of the atomic medium, $\mathcal{N}$ its constant density and k_s the wavevector of the signal field. The transmission of the signal through the atomic medium can be written as $T(\Delta_s, \Delta_c) = e^{-k_s L\,\mathrm{Im}(\chi(\Delta_s,\Delta_c))}$ but also with the normalized susceptibility $\overline{\chi}(\Delta_s, \Delta_c)$:

$$T(\Delta_s, \Delta_c) = e^{-d_0\,\mathrm{Im}(\overline{\chi}(\Delta_s,\Delta_c))} \quad , \quad \overline{\chi}(\Delta_s, \Delta_c) = \frac{\gamma_{ge}(i\gamma_{gs}+\delta)}{\Omega_c^2/4-(i\gamma_{gs}+\Delta_s-\Delta_c)(i\gamma_{ge}+\Delta_s)}. \tag{1.26}$$

Imaginary and real parts of the normalized susceptibility at the signal wavelength are presented in figure 1.3 as a function of the signal detuning Δ_s with a resonant control field for different Rabi frequencies. The imaginary part of the susceptibility represents the absorption properties of the atomic medium whereas the real part is

giving its dispersion (evolution of the refractive index with the signal frequency).

This figure shows two different regimes: the Autler-Townes and EIT regimes. The Autler-Townes regime is defined by the condition $\Omega_c > \Gamma$ and is illustrated by the first column ($\Omega_c = 4\Gamma$). The absorption profile in figure 1.3(a) is composed of two Lorentzian functions with a width equal to $\Gamma/2$ spaced by the Rabi frequency Ω_c. If the control field was not applied, we would see one peak with a linewidth equal to Γ. For $\Omega_c = \Gamma/2$, we expect the absorption at $\Delta_s = 0$ to increase as the two Lorentzian profiles are spaced by a gap equivalent to their width. However it is not the case as the result from figure 1.3(b) demonstrates. Indeed, the absorption at zero detuning remains zero. It can be explained by a destructive interference between two excitation paths ($|g\rangle \rightarrow |e\rangle$ and $|s\rangle \rightarrow |e\rangle$) preventing the atoms to populate $|e\rangle$. The atoms are in a "dark state" as they are not scattering incoming light. This phenomenon is called electromagnetically induced transparency (EIT). An extreme case is presented in figure 1.3(c) where $\Omega_c = \Gamma/10$. A narrow transparency window persists but absorption appears at $\Delta_s = 0$ due to the decoherence rate $\gamma_{gs} = 10^{-3}\Gamma$ between $|g\rangle$ and $|s\rangle$. The dispersion of the medium is also modified by the control field as figures 1.3(d),(e),(f) demonstrate, leading to slow light at the signal wavelength inside the atomic ensemble.

Slow light

The signal field has a group velocity defined as $v_g = d\omega_s/dk_s$. Its wave vector inside the medium is $k_s = n\omega_s/c$ with $n = 1 + \frac{1}{2}\,\mathrm{Re}(\chi)$. The group velocity can thus be expressed as:

$$v_g = \frac{c}{1 + \frac{\omega_s}{2}\frac{d\,\mathrm{Re}(\chi)}{d\omega_s}} \tag{1.27}$$

assuming that near resonance $\mathrm{Re}(\chi) \ll \omega_s \frac{d\,\mathrm{Re}(\chi)}{d\omega_s}$, which is valid for an atomic medium with high dispersion and low density. As a result the group velocity around $\Delta_s = 0$ depends on the derivative of the real susceptibility. As it is visible in figures 1.3(d),(e),(f), the slope at zero detuning decreases with the Rabi frequency of the control field Ω_c. More specifically, by expanding the real part of the susceptibility around zero detuning, the relation (1.27) can be approximated to:

$$v_g \approx \frac{\Omega_c^2 L}{d_0 \Gamma}. \tag{1.28}$$

The group velocity is thus proportional to Ω_c^2, i.e. the intensity of the control light. Small values of Ω_c enables to slow down the signal [Hau et al., 1999]. The signal propagating inside the EIT window is thus named "slow light". Therefore, light can be stopped when the limit $\Omega_c = 0$ is reached as we will describe more vigorously in the following section.

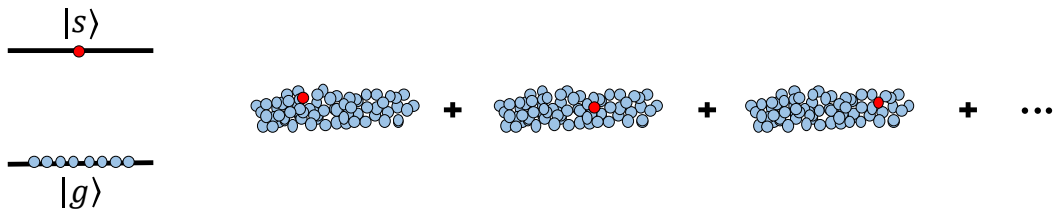

FIGURE 1.4: **Collective excitation.** One atom of the cloud is driven from the ground state $|g\rangle$ to the long-lived spin state $|s\rangle$. As the excitation is spread out across the entire ensemble, the position of the excited atom is in a superposition of all possibilities.

1.2.3 Efficient storage-and-retrieval process in atomic ensembles

This section presents the storage-and-retrieval process based on dynamical EIT. The optimization parameters to increase the memory efficiency are specified.

Collective excitation

Mapping the signal pulse in a collective excitation of the cloud is required to perform an efficient transfer into and out of the quantum memory. The principle of the collective excitation is illustrated in figure 1.4. If the pulse only contains one photon, one atom in the cloud is going to be driven from the ground state $|g\rangle$ to the long-lived spin state $|s\rangle$. As the excitation is spread out across the entire ensemble, the position of the excited atom is in a superposition of all possibilities. Each atom actively contributes to the absorption process, preserving the phase of the incoming field in the coherence between $|s\rangle$ and $|g\rangle$. The collective state called a "spin wave" can thus be noted as:

$$|\Psi\rangle = \frac{1}{\sqrt{N}} \sum_{j=1}^{N} e^{i\varphi_j} |g_1, ..., g_{i-1}, s_j, g_{i+1}, ..., g_N\rangle \tag{1.29}$$

with N the number of atoms and φ_j the phase acquired by the j-th atom. This phase is determined by the interference pattern between the signal and the control fields which is printed on the atomic ensemble. In practice, the amplitude in front of each term of the sum is not the same and depends on the signal pulse spatial profile and the density distribution of the cloud.

Storage-and-retrieval process

We consider a three-level system as the one in figure 1.2. The signal field is resonant with the transition $|g\rangle \rightarrow |e\rangle$ and the control field is resonant with the transition $|s\rangle \rightarrow |e\rangle$. In the previous sections, the signal field was defined as a classical field. From now on, this one is quantized and described by the operator:

$$\hat{E}_s(z,t) = \sum_k \hat{a}_k(t) e^{ikz} \tag{1.30}$$

with $\hat{a}_k$ the annihilation operator of the k wavevector. A collective excitation of the atomic medium from a state $|a\rangle$ to a state $|b\rangle$ is represented by the operator:

$$\hat{\sigma}_{ba}(z,t) = \frac{1}{N_z}\sum_{j=1}^{N_z} |b_j\rangle\langle a_j| e^{-i\omega_{ba}t} \tag{1.31}$$

with N_z the number of atoms contained in a small volume centered on the position z. The evolution of these atomic operators is given by the Heisenberg-Langevin equations. In the previous section, we took the Schrodinger picture with a time-dependent density matrix $\hat{\rho}(t)$. In this section, we are taking the Heisenberg picture with time-dependent operators $\hat{\sigma}(t)$. The Heisenberg-Langevin equations can be solved with the same method than the Lindblad master equation using perturbation series which leads to similar mathematical relations: (1.20) and (1.21) can be used by replacing the density matrix $\hat{\rho}$ by the operator $\hat{\sigma}$. The electromagnetic fields being quantized, Ω_s is also replaced by $\Omega_0\hat{E}_s$ introducing the vacuum Rabi frequency $\Omega_0 = 2d_{eg}\sqrt{\frac{\omega_{eg}}{2\hbar\epsilon_0 V}}$, with V the atom-light interaction volume defined by the overlap between the signal and the atomic ensemble. After implementing these modifications, we obtain the result[2] on resonance ($\Delta_s = \Delta_c = 0$):

$$\frac{\partial\hat{\sigma}_{ge}}{\partial t} = -\gamma_{ge}\hat{\sigma}_{ge} + \frac{i}{2}\Omega_c(t)\hat{\sigma}_{gs} + \frac{i}{2}\Omega_0\hat{E}_s \tag{1.32}$$

$$\frac{\partial\hat{\sigma}_{gs}}{\partial t} = -\gamma_{gs}\hat{\sigma}_{gs} + \frac{i}{2}\Omega_c(t)\hat{\sigma}_{ge}. \tag{1.33}$$

The Rabi frequency of the control $\Omega_c(t)$ is time-dependent. As $|s\rangle$ is considered as a long-lived state, γ_{gs} can be neglected in equation (1.33):

$$\hat{\sigma}_{ge} = \frac{-2i}{\Omega_c(t)}\frac{\partial\hat{\sigma}_{gs}}{\partial t}. \tag{1.34}$$

This new expression can be injected into (1.32):

$$-\frac{4}{\Omega_c(t)}\left(\frac{\partial}{\partial t} + \gamma_{ge}\right)\cdot\left(\frac{1}{\Omega_c(t)}\frac{\partial\hat{\sigma}_{gs}}{\partial t}\right) = \hat{\sigma}_{gs} + \frac{\Omega_0\hat{E}_s}{\Omega_c(t)}. \tag{1.35}$$

We assume a slow change of the control Rabi frequency $\Omega_c(t)$ in the adiabatic limit [Harris and Yamamoto, 1998; Lukin and Imamoglu, 2000]. The characteristic time of this change is noted T_c. One can define a dimensionless variable $t' = t/T_c$ and expand equation (1.35) on the parameter $1/T_c$. The lowest order of this perturbative expansion is:

$$\hat{\sigma}_{gs} = -\frac{\Omega_0\hat{E}_s}{\Omega_c}. \tag{1.36}$$

The paraxial approximation states that $|\frac{\partial^2\hat{E}_s}{\partial z^2}| \ll |k\frac{\partial\hat{E}_s}{\partial z}|$, and can be applied if we

[2] Equations (1.32) and (1.33) contain a factor 1/2 which is not the case of the paper [Fleischhauer and Lukin, 2000]. Indeed, this factor appears when the rotating wave approximation is applied. Theoreticians often discard it.

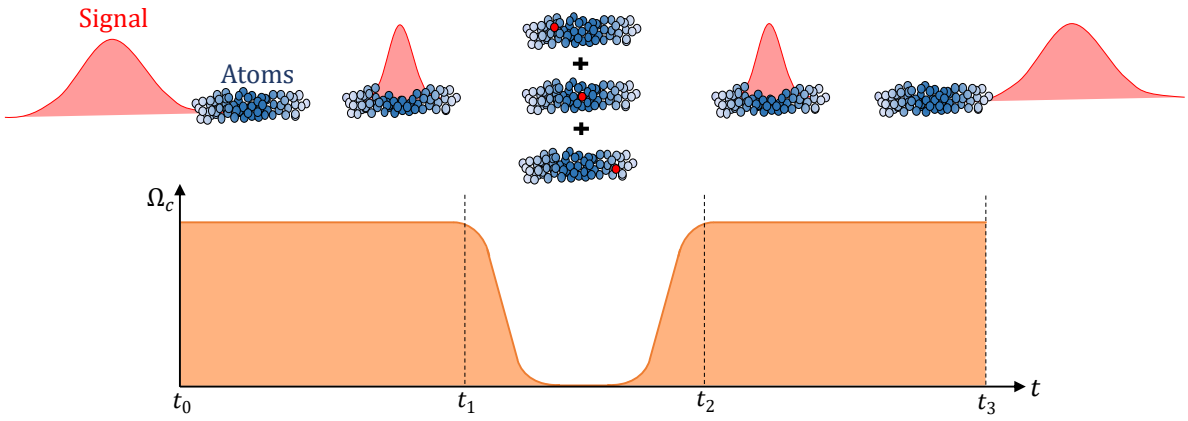

FIGURE 1.5: **Storage-and-retrieval process.** Before time t_0, the signal pulse has not interacted with the atomic medium. At time t_0, the control intensity is turned on to open an EIT window and let the signal enter into the cloud. The signal pulse is thus spatially compressed into the atomic medium by factor $1/n_g$. When the pulse is entirely contained into the cloud, Ω_c is adiabatically decreased to zero (time t_1). The signal is mapped in a collective excitation of the atomic ensemble. After a controllable storage time, Ω_c is adiabatically increased to its original value (time t_2) which triggers the retrieval process. The pulse reappears inside the cloud and leaves it at time t_3.

consider $\hat{E}_s(z,t)$ as a slowly varying function of z. The evolution of the signal field is given by the propagation equation [Fleischhauer and Lukin, 2000]:

$$\left(\frac{\partial}{\partial t} + c\frac{\partial}{\partial z}\right) \cdot \hat{E}_s(z,t) = i\frac{\Omega_0}{2} N \hat{\sigma}_{ge}(z,t), \tag{1.37}$$

N being the total number of atoms. By combining (1.34), (1.36) and (1.37), we obtain the formula which governs the quantized electromagnetic field evolution in the adiabatic limit:

$$\left(\frac{\partial}{\partial t} + c\frac{\partial}{\partial z}\right) \cdot \hat{E}_s(z,t) = -\frac{\Omega_0 N}{\Omega_c(t)} \frac{\partial}{\partial t} \frac{\hat{E}_s(z,t)}{\Omega_c(t)}. \tag{1.38}$$

A solution to this equation is known as the dark state polariton, described by the quantum operator $\hat{\Psi}$:

$$\hat{\Psi}(z,t) = \cos\theta(t)\hat{E}_s(z,t) - \sin\theta(t)\sqrt{N}\hat{\sigma}_{gs}(z,t) \tag{1.39}$$

with

$$\cos\theta(t) = \frac{\Omega_c(t)}{\sqrt{\Omega_c(t)^2 + \Omega_0^2 N}} \quad , \quad \sin\theta(t) = \frac{\Omega_0\sqrt{N}}{\sqrt{\Omega_c(t)^2 + \Omega_0^2 N}}. \tag{1.40}$$

This dark state polariton $\hat{\Psi}$ is a superposition between a photonic state represented by $\hat{E}_s$ and a collective spin-wave excitation represented by $\hat{\sigma}_{gs}$.

The evolution over time of $\Omega_c(t)$ can be chosen in order to efficiently store-and-retrieve the signal field as it is presented in figure 1.5. Before t_0, the signal pulse has not interacted with the atomic medium. At the time t_0, the control intensity is

turned on to open an EIT window and let the signal enter into the cloud. When the signal is inside the cloud, we can't consider it anymore just as a photonic state. The equation (1.39) demonstrates that it is a dark state polariton, i.e. a superposition between a photonic state and a collective spin-wave excitation. $\hat{\Psi}(z,t)$ is governed by the equation of motion:

$$\left(\frac{\partial}{\partial t} + c\cos^2\theta(t)\frac{\partial}{\partial z}\right)\cdot\hat{\Psi}(z,t) = 0 \tag{1.41}$$

As a result, this dark state polariton has a group velocity $v_g = c/n_g$ with $n_g = 1/\cos^2\theta(t)$. The signal pulse is thus spatially compressed in the atomic medium by factor $1/n_g$. Ω_c is adiabatically decreased to zero when the pulse is entirely contained into the cloud (time t_1). This requirement is crucial to achieve a high memory efficiency as the fraction of light located outside the cloud at t_1 is not going to be stored. The group velocity $v_g = 0$ indicates that the pulse in the medium is stopped. $\hat{\Psi}(z,t) = -\sqrt{N}\hat{\sigma}_{gs}(z,t)$ only exhibits the collective spin-wave excitation without any photonic component: the photonic state has been fully mapped on the atomic degrees of freedom. After a controllable storage time, Ω_c is adiabatically increased to its original value (time t_2) which triggers the retrieval process. The signal pulse reappears inside the atomic ensemble as the term $\hat{E}_s(z,t)$ in the state $\hat{\Psi}(z,t)$. At the time t_3, the pulse leaves the cloud and returns to its original shape.

Optimization of the memory efficiency

As discussed earlier, one of the main key element for quantum memories is the storage-and-retrieval efficiency. Therefore, this subsection is about the theoretical considerations to optimize the memory efficiency. The practical implementation of this optimization is described on the second chapter.

In the real experiment, we are not working with a three-level system but with a much more complex atomic structure. The states involved are called hyperfine levels and result from from the interaction between the magnetic moments associated to the nuclear and electronic spins. These hyperfine states are composed of many sublevels named Zeeman levels. A representation of this atomic structure is given in figure 1.6 for D1 Cesium line as used in this work. The ground state is $|g\rangle = |6S_{1/2}, F = 3\rangle$, the long-lived spin state is $|s\rangle = |6S_{1/2}, F = 4\rangle$ and the excited state is $|e\rangle = |6P_{1/2}, F' = 4\rangle$. As previously, the signal field is resonant with the transition $|g\rangle \rightarrow |e\rangle$ and the control field is resonant with the transition $|s\rangle \rightarrow |e\rangle$. An hyperfine level F is composed of $2F + 1$ Zeeman sublevels annotated by the number $m_F = \{-F, -F+1, .., F-1, F\}$. One important parameter to consider is the choice of polarizations for the signal and control beams. We define the z-axis as the quantization axis. The first configuration is presented in figure 1.6(a): the polarization of the signal is σ_z^+ and the control is σ_z^-. The selection rules require that the signal drives transitions $|F, m_F\rangle \rightarrow |F', m_{F'} = m_F + 1\rangle$ and the control drives

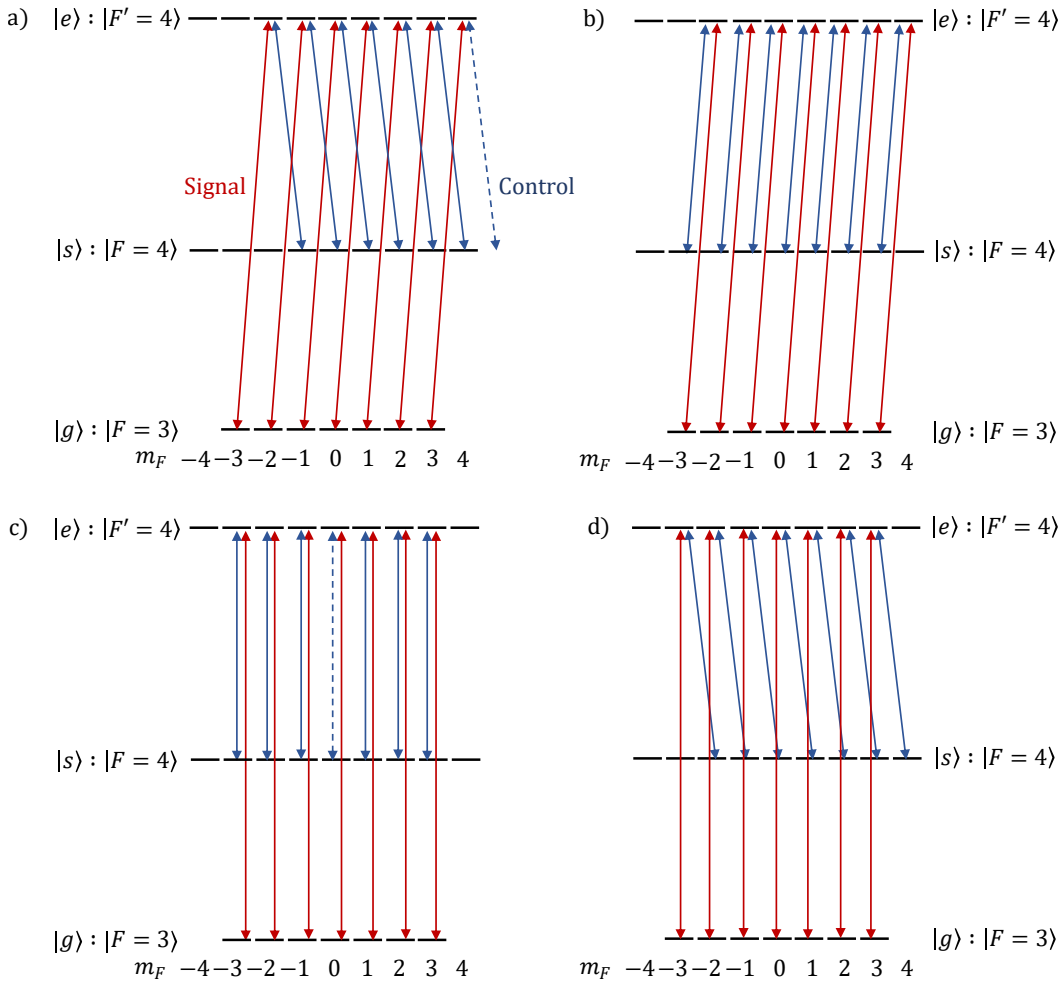

FIGURE 1.6: **Configurations for the polarizations of the signal and control beams.** The signal field is resonant with the transition $\left|F = 3\right\rangle \rightarrow \left|F' = 4\right\rangle$ and the control field is resonant with the transition $\left|F = 4\right\rangle \rightarrow \left|F' = 4\right\rangle$. *a)* The polarization of the signal is σ_z^+ and the control is σ_z^-. The sublevel $m_{F'} = 4$ is not driven by the control light leading to the absorption of the signal. *b)* The polarization of the signal is σ_z^+ and the control is also σ_z^+. In this specific configuration, each Zeeman level from the excited state is addressed by both signal and control fields leading to an optimal EIT transmission. *c)* Both fields are π_z polarized. In this case, we could not observe EIT as the transition $\left|F = 4, m_F = 0\right\rangle \rightarrow \left|F' = 4, m_{F'} = 0\right\rangle$ is forbidden. *d)* The last configuration is π_z polarization for the signal and σ_z^- for the control which leads to an optimal transparency window. However, this configuration is impossible to implement for two beams which are propagating in the same direction.

$|F, m_F\rangle \rightarrow |F', m_{F'} = m_F - 1\rangle$. In order to observe EIT, each Zeeman level from the excited state ($|6P_{1/2}, F' = 4\rangle$) should be addressed by both signal and control fields. However, the sublevel $m_{F'} = 4$ is not driven by the control light leading to the absorption of the signal. As the atomic medium has a high optical depth, this absorption drastically decreases the EIT transmission. The second configuration is in figure 1.6(b): the polarization of the signal is σ_z^+ and the control is also σ_z^+. In this specific case, each Zeeman level from the excited state is addressed by both signal and control fields leading to an optimal EIT transmission. In this example, we took σ_z^+ but it also works if the two fields are σ_z^- polarized. If both fields are π_z polarized (figure 1.6(c)), we could not observe EIT as the transition $|F = 4, m_F = 0\rangle \rightarrow |F' = 4, m_{F'} = 0\rangle$ is forbidden. The last configuration (figure 1.6(d)) is π_z polarization for the signal and circular polarization for the control which leads to an optimal transparency window. However, this configuration is impossible to implement for two beams which are propagating in the same direction. As a result, signal and control beams having the same circular polarization is the best option for our experiment.

The second consideration for memory optimization is about the value of Ω_c during the EIT phase (between t_0 and t_1 in figure 1.5). Two constraints have to be satisfied. The first one is $\Delta\nu_{\text{EIT}} > 1/\Delta t_{\text{pulse}}$: the width of the signal pulse in the frequency domain has to be smaller than the width of the EIT window. In order to deduce from this constraint a condition on Ω_c, we have to expand the normalized susceptibility (1.26) around the resonance ($\Delta_s/\Omega_c \ll 1$) with $\Delta_c = 0$ and $\gamma_{gs} = 0$. The result at first order is $\overline{\chi}(\Delta_s) \approx \frac{\gamma_{ge}\Delta_s}{(\Omega_c/2)^2}(1 + i\frac{\gamma_{ge}\Delta_s}{(\Omega_c/2)^2})$. The EIT transmission is equal to $T(\Delta_s) = e^{-d_0\,\text{Im}(\overline{\chi}(\Delta_s))}$ and can thus be approximated by $T(\Delta_s) \approx e^{-\Delta_s^2/\Delta\nu_{\text{EIT}}^2}$ with $\Delta\nu_{\text{EIT}} = \frac{(\Omega_c/2)^2}{\gamma_{ge}\sqrt{d_0}}$. As a result, the first constraint $\Delta\nu_{\text{EIT}} > 1/\Delta t_{\text{pulse}}$ results in:

$$\Omega_c^2 > \frac{2\Gamma\sqrt{d_0}}{\Delta t_{\text{pulse}}} \tag{1.42}$$

with $\Gamma = 2\gamma_{ge}$ the decay rate of the excited state. If this condition is not satisfied, a fraction of the pulse will be absorbed in the excited state which lowers the transfer efficiency from $|g\rangle$ to $|s\rangle$. The second constraint is that the wavepacket should fit in the cloud, i.e. $l_{\text{pulse}} < L$ with L the cloud length and $l_{\text{pulse}} = c/n_g \cdot \Delta t_{\text{pulse}}$ the pulse length inside the medium. Otherwise, the early part of the pulse will leak outside of the cloud and the late part is going to be absorbed. We can express this second requirement in terms of the Rabi frequency Ω_c[3]:

$$\Omega_c^2 < \frac{\Gamma d_0}{\Delta t_{\text{pulse}}}. \tag{1.43}$$

Therefore, there is a trade-off to make on the value of Ω_c to fulfill these two requirements. The size of the interval defined by the two inequalities (1.42) and (1.43) is proportional to $\sqrt{d_0}$ which demonstrates the importance of the optical depth in order

[3]This limit has been calculated with the assumption that the pulse length before compression is much higher than the length of the atomic medium.

to maximize the memory efficiency. One can note that Ω_c and Δt_{pulse} play a symmetric role in the optimization process. Indeed, one method would be to adjust Ω_c with a fixed Δt_{pulse} and the other is to optimize Δt_{pulse} with a fixed Ω_c. In practice, we can use these two methods to find the optimal values of both parameters.

In the previous sections, we didn't take into account sources of decoherence. Indeed, when the signal is stored, the collective excitation of the ensemble is sensitive to its magnetic environment and also to atoms motion. This topic is thoroughly discussed in the next part of this chapter.

1.2.4 Decoherence in the memory process

The memory efficiency decreases with storage time due to decoherence mechanisms. They modify the initial collective excitation leading to a decrease in the retrieval efficiency. A general way to describe the collective spin-wave in the presence of decoherence sources is:

$$|\Psi(t)\rangle = \frac{1}{\sqrt{N}} \sum_{j=1}^{N} e^{-i\Delta\omega_{sg}(\vec{r}_j,\vec{v}_j)t} |g_1, ..., g_{i-1}, s_j, g_{i+1}, ..., g_N\rangle \tag{1.44}$$

with $\Delta\omega_{sg}(\vec{r}_j, \vec{v}_j)$ the frequency shift of the spin wave seen by the j-th atom which can depend on its position or velocity according to the source of decoherence we are considering.

Residual magnetic field

During the storage process, the magnetic field of our magneto-optical trap is turned off but a residual B-field can be persistent due to long-lived Eddy currents. In this subsection, we are going to study the impact of this residual magnetic field on the evolution of the memory efficiency over time.

The energy levels of the atoms are shifted in the presence of a magnetic field. This phenomenon is called the Zeeman effect. The shift linearly depends on the sublevel m_F and can be written $\Delta E = m_F \mu_B g_F B_z$ with μ_B the Bohr magneton, g_F the Landé g-factor of the hyperfine level F and B_z the external magnetic field along the z-axis. If we consider the frequency of the transition $|g, m_g\rangle \rightarrow |s, m_s\rangle$ at the position $\vec{r}_j$ of the j-th atom, this one is going to shift as $\Delta\omega_{sg}(\vec{r}_j, m_g, m_s) = (m_s + m_g)\mu_B g B_z(\vec{r}_j)/\hbar$ assuming that the Landé g-factor of the ground state is $-g$ and the spin state is the opposite g. Then, each single excitation $|s_j(t)\rangle$ from equation (1.44) is going to be modified over time as:

$$|s_j(t)\rangle = \sum_{m_g, m_s} n(m_g) d(m_g, m_s) e^{-i\Delta\omega_{sg}(\vec{r}_j, m_g, m_s)t} |s, m_s\rangle \tag{1.45}$$

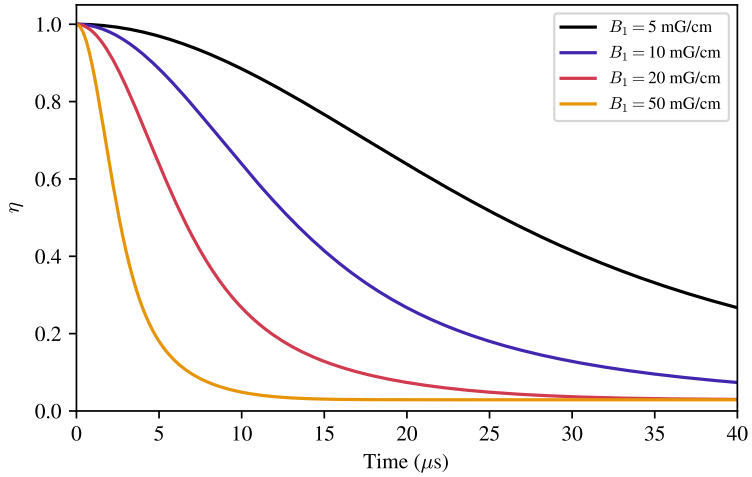

FIGURE 1.7: **Retrieval efficiency as a function of the storage time for different values of residual magnetic field gradient.** These results were calculated for a population equally distributed among the Zeeman levels and a length of the atomic medium equal to $L = 2.5\,\text{cm}$.

with $n(m_g)$ the probability to have an atom in the Zeeman level m_g at $t = 0$ and $d(m_g, m_s)$ the strengths of the transitions used for the storage-and-retrieval process. The polarization of the signal and control beams are chosen to be the same circular polarization which leads to $m_g = m_s$. The external magnetic field can be noted as $B(z) = B_0 + B_1 z$. The constant contribution is easy to cancel experimentally but the inhomogeneous one remains. For this reason, we take $B_0 = 0$ to study the effect of the gradient on the memory lifetime. The j-th atom $\vec{r}_j$ can be identified by its position z, and the sum $\frac{1}{N}\sum_{j=1}^{N}$ of (1.44) can be replaced by an integral $\int_{z=0}^{L} \mathcal{N}(z)$ with $\mathcal{N}(z)$ the density of atoms. The retrieval efficiency $\eta(t) = |\langle\Psi(t=0)|\Psi(t)\rangle|^2$ can thus be expressed as:

$$\eta(t) = \left| \sum_{m_g=-F}^{F} n(m_g) d(m_g) \int_z \mathcal{N}(z) e^{-i\alpha_{m_g} z t} dz \right|^2 . \tag{1.46}$$

with $\alpha_{m_g} = 2m_g \mu_B g B_1/\hbar$. We choose a Gaussian profile for density of atoms along the z-axis: $\mathcal{N}(z) = \frac{2}{L\sqrt{\pi}} e^{-\frac{z^2}{(L/2)^2}}$. The integral is therefore the Fourier transform of a Gaussian function in space which leads to a Gaussian function in time:

$$\eta(t) = \left| \sum_{m_g=-F}^{F} n(m_g) d(m_g) e^{-t^2/\tau_{m_g}^2} \right|^2 \tag{1.47}$$

with $\tau_{m_g} = 2\hbar/(m_g \mu_B g B_1 L)$. We assume that the Zeeman levels are equally populated ,i.e. $n(m_g) = 1/(2F+1)$. As before, we consider that the ground state is $|g\rangle = |6S_{1/2}, F = 3\rangle$, the long-lived spin state is $|s\rangle = |6S_{1/2}, F = 4\rangle$ and the excited state is $|e\rangle = |6P_{1/2}, F' = 4\rangle$. The transition strengths $d(m_g)$ are given by [Steck,

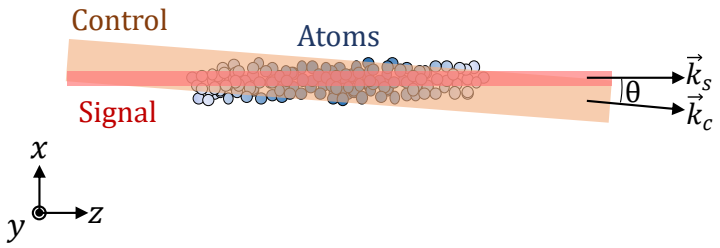

FIGURE 1.8: **Wavevectors of the signal and control beams in EIT configuration.** The signal wavevector $\vec{k}_s$ and the control wavevector $\vec{k}_c$ lie in the xz plane and are separated by an angle θ.

1998] in the configuration described in figure 1.6(b). The retrieval efficiency as a function of the storage time is represented in figure 1.7 for different values of residual magnetic field gradient. These results were calculated for a length of the atomic medium equal to $L = 2.5\,\text{cm}$. The lifetime τ of a quantum memory can be defined as the time for which the memory efficiency dropped at $1/e \approx 37\%$ of its initial value. The lifetimes corresponding to each residual magnetic field gradient are: $\tau = 3\,\mu\text{s}$ for $B_1 = 50\,\text{mG/cm}$, $\tau = 8\,\mu\text{s}$ for $B_1 = 20\,\text{mG/cm}$, $\tau = 16\,\mu\text{s}$ for $B_1 = 10\,\text{mG/cm}$, $\tau = 32\,\mu\text{s}$ for $B_1 = 5\,\text{mG/cm}$. τ scales as the inverse of the residual B-field gradient. One can note that the curves are not converging to $\eta = 0$ which can be explained by the atoms populating the Zeeman level $m_g = 0$. They are totally insensitive to the magnetic field as they are driven from $m_g = 0$ to $m_s = 0$.

Motional dephasing

During the storage time, atoms are moving due to their temperature. In this subsection, we will assess the impact of this motion on the memory lifetime. We consider the configuration presented in figure 1.8. The signal wavevector $\vec{k}_s$ and the control wavevector $\vec{k}_c$ lie in the xz plane and are separated by an angle θ. As a result, the wavector of the spin wave is $\Delta\vec{k} = \vec{k}_s - \vec{k}_c$. The j-th atom has an initial position $\vec{r}_j$ with a constant velocity $\vec{v}_j$. Indeed, at these short timescales (less than a millisecond) we can neglect the impact of gravity on the velocity of atoms. The collective state can thus be written as:

$$|\Psi(t)\rangle = \frac{1}{\sqrt{N}} \sum_{j=1}^{N} e^{-i\Delta\vec{k}\cdot(\vec{r}_j+\vec{v}_j t)} |g_1, ..., g_{i-1}, s_j, g_{i+1}, ..., g_N\rangle. \tag{1.48}$$

The retrieval efficiency $\eta(t) = |\langle\Psi(t=0)|\Psi(t)\rangle|^2$ can be expressed as:

$$\eta(t) = \left| \frac{1}{N} \sum_{j=1}^{N} e^{-i\Delta\vec{k}\cdot\vec{v}_j t} \right|^2. \tag{1.49}$$

The sum $\frac{1}{N}\sum_{j=1}^{N}$ can be replaced by an integral $\int_v f(v)$ with the Maxwell-Boltzmann distribution $f(v)$. The velocities which are participating to the spin-wave dephasing are the ones oriented in the xz plane as the wavevectors lie in this plane. The final

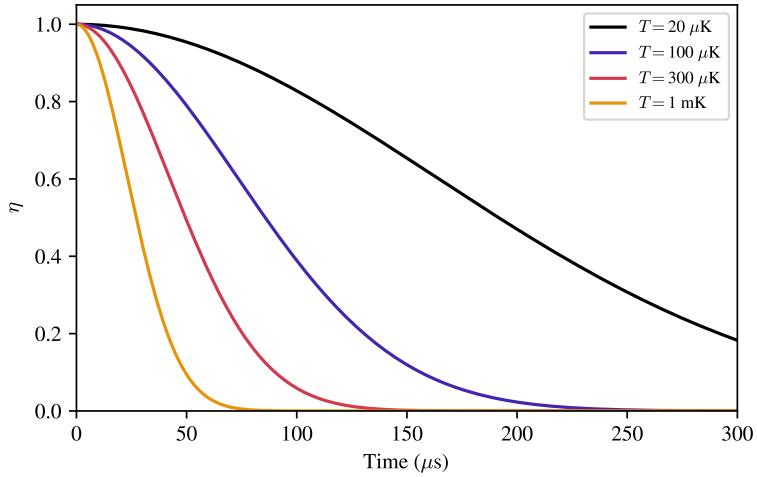

FIGURE 1.9: **Retrieval efficiency as a function of the storage time for different values of gas temperature.** The angle between the signal and control beams was set to $\theta = 1°$. $T = 20\,\mu$K corresponds to the temperature of an atomic cloud after sub-Doppler cooling, $T = 100\,\mu$K is approximately the Doppler temperature limit.

result is:

$$\eta(t) = \left| \int_v f(v) e^{-i\Delta\vec{k}\cdot\vec{v}t} dv \right|^2 \tag{1.50}$$

$$\approx e^{-t^2/\tau^2} \tag{1.51}$$

with the lifetime $\tau = 1/(|\Delta\vec{k}|\sigma_v)$ and the standard deviation of the Boltzmann distribution $\sigma_v = \sqrt{k_B T/m}$. The expression (1.51) is obtained by calculating the Fourier transform of the Maxwell-Boltzmann distribution $f(v)$. The frequencies of the signal and control fields are really close (9.2 GHz difference), so we can consider they have the same wavelength λ. For small θ, the wavevector of the spin wave has a norm equal to $|\Delta\vec{k}| = 2\pi \sin\theta/\lambda$. The lifetime associated to the motional dephasing can thus be noted:

$$\tau = \frac{\lambda}{2\pi \sin\theta} \sqrt{\frac{m}{k_B T}}. \tag{1.52}$$

The retrieval efficiency is represented in figure 1.9 as a function of the storage time for different values of temperature. The angle between the two beams was set to $\theta = 1°$. $T = 20\,\mu$K corresponds to the temperature of an atomic cloud after sub-Doppler cooling (such as polarization gradient cooling) and leads to a lifetime $\tau = 230\,\mu$s. The Doppler temperature limit, being approximately $T = 100\,\mu$K, gives a lifetime $\tau = 100\,\mu$s. Finally, atomic memories at $T = 300\,\mu$K reach a lifetime $\tau = 60\,\mu$s and the ones at $T = 1\,$mK correspond to $\tau = 33\,\mu$s. This is the reason why groups working with hot vapors [Dideriksen et al., 2021; Namazi et al., 2017a; Reim et al., 2011] need to set the signal and control fields colinear ($\theta = 0$) as the motional

dephasing increases drastically with the temperature of atoms. In this case, multiple Fabry-Perot cavities (FPC) in cascade are required to filter out the control, which significantly reduces the transmission of the detection setup.

Differential light shift

One solution to reduce motional dephasing is the implementation of a tightly confining optical lattice [Zhao et al., 2009]. However, it also creates another source of decoherence induced by the inhomogeneous intensity profile of the lattice: the differential light shift. Indeed, the principle of a dipole trap is to use off-resonant light and high intensity lasers to create a potential well thanks to light shift. The light shift of an atomic state $|F, m_F\rangle$ which is coupled to many excited states $|F', m_{F'}\rangle$ can be written:

$$\Delta\mathcal{E}_{F,m_F}(r) = |E(r)|^2 \sum_{F',m_{F'}} \frac{\left|\langle F, m_F| \vec{d} |F', m_{F'}\rangle\right|^2}{4\hbar\Delta_{F',m_{F'}}} \tag{1.53}$$

with E the amplitude of the light electric field and $\Delta_{F',m_{F'}} = \omega - (\omega_{F',m_{F'}} - \omega_{F,m_F})$ the detuning of the light frequency ω from the transition $|F, m_F\rangle \rightarrow |F', m_{F'}\rangle$. As the light intensity is not constant over space, it creates a position-dependent light shift. The frequency of the spin wave will then experience a light shift $\Delta\omega_{sg}(r, m_g, m_s) = (\Delta\mathcal{E}_{s,m_s}(r) - \Delta\mathcal{E}_{g,m_g}(r))/\hbar$. Therefore the calculation of the retrieval efficiency can be derived with the same method than the one used for the residual magnetic field as the shift of the spin wave depends on the same parameters for both problems (r, m_g, m_s). One can note the requirement to optically pump all the atoms in a particular Zeeman level m_g to limit the impact of this differential light shift on the memory lifetime. A complete study of this decoherence source is presented in [Jenkins et al., 2012] for more details.

1.3 Cooling and trapping mechanisms

The previous sections were about the explanation of the memory process. Our quantum memory is based on cold atoms. This section presents a theoretical description of the cooling and trapping mechanisms used in our experiment, going from the Doppler cooling to the principle of a magneto-optical trap and finishing by the study of polarization gradient cooling.

1.3.1 Doppler cooling

Doppler cooling was first proposed by [Hänsch and Schawlow, 1975] and experimentally implemented in [Chu et al., 1985] with sodium atoms. Laser beams are red-detuned from an atomic transition in order to be resonant with atoms moving toward the beams due to Doppler effect. These atoms are going to absorb and spontaneously re-emit photons in all directions. They are cooled down as light reduces their

kinetic energy by momentum transfer (radiation pressure). In this section we will calculate the limit temperature of this cooling method, called Doppler temperature.

The study of the cooling process is done in one dimension. We consider a two-level atom moving along the z direction with a velocity $\vec{v}$ and the light electric field $\vec{E}$. After applying the rotating wave approximation, the hamiltonian in the interaction picture is:

$$\hat{H} = -\frac{\hbar\Delta_v}{2}(|e\rangle\langle e| - |g\rangle\langle g|) - \frac{\hbar\Omega}{2}(|e\rangle\langle g| + |g\rangle\langle e|) \tag{1.54}$$

with the Rabi frequency $\Omega = \vec{d}_{ge} \cdot \vec{E}/\hbar$. The detuning $\Delta_v = \Delta_0 - \vec{k} \cdot \vec{v}$ is composed of two terms: the first is the detuning of the light frequency from the resonance of an atom at rest $\Delta_0 = \omega - \omega_{eg}$ and the second term is due to the Doppler shift. After injecting this hamiltonian into the Lindblad master equation (1.14) and projecting on the right states, we obtain:

$$\frac{d\rho_{ee}}{dt} = \Omega\,\mathrm{Im}(\rho_{eg}) - \Gamma\rho_{ee} \tag{1.55}$$

$$\frac{d\rho_{eg}}{dt} = (i\Delta_v - \gamma_{ge})\rho_{eg} + \frac{i}{2}\Omega(\rho_{gg} - \rho_{ee}) \tag{1.56}$$

We know ρ_{ee} and ρ_{gg} are linked with the relation $\rho_{ee} + \rho_{gg} = 1$. In the steady state regime (derivative equal to zero) the expression of ρ_{ee} is:

$$\rho_{ee} = \frac{1}{2}\frac{s}{s+1} \tag{1.57}$$

with the saturation parameter

$$s = \frac{s_0}{1 + 4\frac{\Delta_v^2}{\Gamma^2}} \tag{1.58}$$

and $s_0 = 2\frac{\Omega^2}{\Gamma^2}$. The radiation pressure applied by the light on the atoms is $\vec{F} = \hbar\vec{k}\Gamma\rho_{ee}$. $\hbar\vec{k}$ is the momentum transfer of one photon, Γ is the decay rate of the excited state and ρ_{ee} is the probability for an atom to be excited. Using (1.57), we can specify the expression of this force:

$$\vec{F} = \frac{\hbar\vec{k}\Gamma}{2}\frac{s}{s+1}. \tag{1.59}$$

If we consider two light beams with the same frequency ω propagating in opposite directions ($\vec{k} = \pm\frac{\omega}{c}\vec{e}_z$), the radiation pressure applied to the atom is:

$$\vec{F} = \frac{\hbar k\Gamma}{2}s_0\left[\frac{1}{1 + s_0 + 4\frac{(\Delta_0 - kv)^2}{\Gamma^2}} - \frac{1}{1 + s_0 + 4\frac{(\Delta_0 + kv)^2}{\Gamma^2}}\right]\vec{e}_z. \tag{1.60}$$

This force is represented in figure 1.10 as a function of the atom velocity in one dimension. The parameters chosen for this graph are: a saturation parameter on resonance $s_0 = 1$, a detuning $\Delta_0 = -\Gamma/2$ with $\Gamma = 2\pi \cdot 5.234\,\mathrm{MHz}$ which corresponds to the linewidth of the Cesium D2 line. The dotted lines are the forces of each beam individually, the upper one being the light with the wavevector $\vec{k} = \frac{\omega}{c}\vec{e}_z$ and the

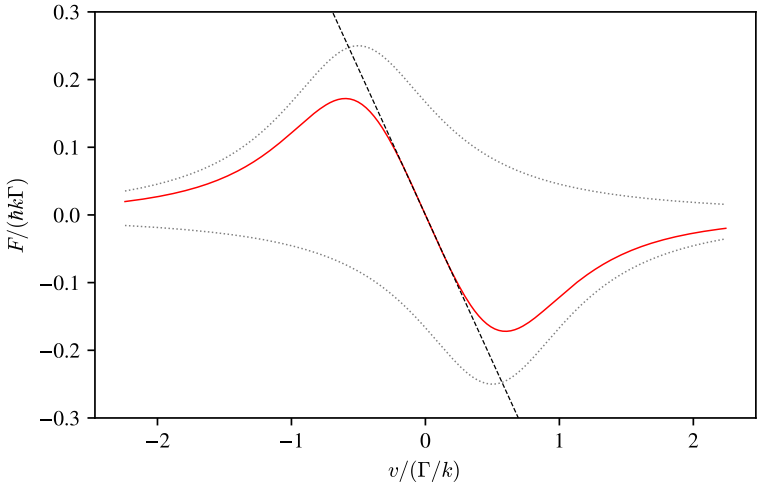

FIGURE 1.10: **Molasse force in function of the atom velocity in one dimension.** The parameters chosen for this graph are: a saturation parameter on resonance $s_0 = 1$, a detuning $\Delta_0 = -\Gamma/2$ with $\Gamma = 2\pi \cdot 5.234\,\text{MHz}$ which corresponds to the linewidth of the Cesium D2 line. The dotted lines are the forces applied by each beam individually, the upper one being the light with the wavevector $\vec{k} = \frac{\omega}{c}\vec{e}_z$ and the lower one is for $\vec{k} = -\frac{\omega}{c}\vec{e}_z$. The dashed line shows the linear behaviour of the force for small velocities ($|v| \ll \Gamma/k$).

lower one is for $\vec{k} = -\frac{\omega}{c}\vec{e}_z$. Atoms with a velocity $|v| < \frac{\Delta_0}{k}$ are participating to the cooling process. If their velocity is negative on the z-axis, the force applied is directed along $+\vec{e}_z$ and the atoms will be slow down. On the opposite side, if their velocity is positive on the z-axis, the force applied is oriented along $-\vec{e}_z$ and their velocity will also decrease. As a result, the radiation pressure created by the two beams acts as a damping force for the atoms. The dashed line shows the linear behaviour of the force for small velocities ($|v| \ll \Gamma/k$). This linear dependency can be specified by expanding equation (1.60):

$$\vec{F} \approx -\beta\vec{v} \quad \text{with} \quad \beta = -\frac{8\hbar k^2 \Delta_0 s_0}{\Gamma(1 + s_0 + 4\Delta_0^2/\Gamma^2)^2}. \tag{1.61}$$

The cooling rate is defined by the power of the force $P_c = \vec{F} \cdot \vec{v}$. The heating rate is associated to the minimum change in atom kinetic energy due to momentum transfer with light and is written $P_h = \frac{\hbar^2 k^2}{2m} R_{sc}$ with the scattering rate $R_{sc} = \Gamma\rho_{ee}$. In steady state, these two rates are equal to each others and lead to a kinetic energy $E_c = -\frac{\hbar}{4}(\Delta_0 + \frac{\Gamma^2}{4\Delta_0})$ with a minimum at $\Delta_0 = -\frac{\Gamma}{2}$. As $E_c = \frac{k_B T}{2}$ for one dimensional gaz, the minimal temperature achievable called the Doppler temperature is $T_D = \frac{\hbar\Gamma}{2k_B}$ which is equal to 125μK for Cesium atoms on the D2 line.

1.3.2 Magneto-optical traps

A magneto-optical trap (MOT) operates by combining laser cooling (presented on previous section) and magnetic-field gradients to slow down and confine atoms within

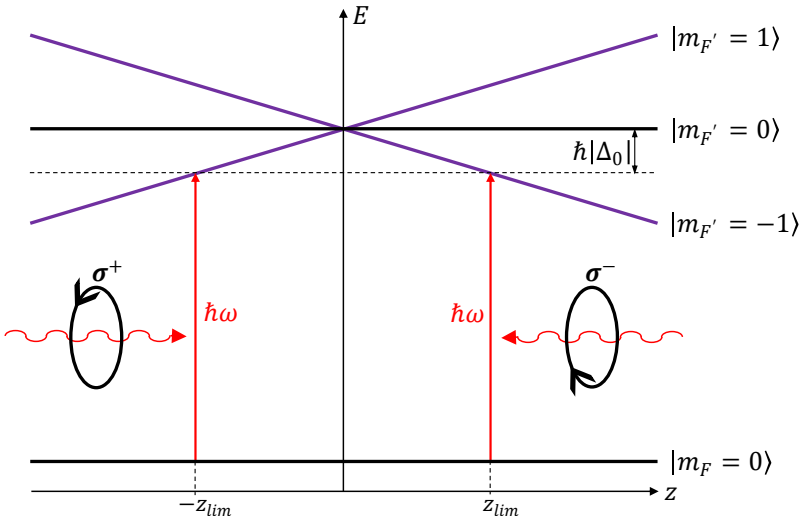

FIGURE 1.11: **Principle of a magneto-optical trap.** We consider a ground state $|m_F = 0\rangle$ and three excited states $|m_{F'} = -1\rangle$, $|m_{F'} = 0\rangle$ and $|m_{F'} = 1\rangle$. If the atom is in the center $z = 0$, both beams are not resonant with any atomic transitions as they are detuned by Δ_0 from the excited states. For $z = -z_{lim}$, the σ^+ polarized beam is resonant with the transition $|m_F = 0\rangle \rightarrow |m_{F'} = 1\rangle$. For $z = z_{lim}$, the σ^- polarized beam is resonant with the transition $|m_F = 0\rangle \rightarrow |m_{F'} = -1\rangle$.

a small region of space. The principle of the MOT is represented in figure 1.11. We consider a linear magnetic field $\vec{B}(z) = Bz\vec{e}_z$ oriented along the z axis with a gradient B. This magnetic field is shifting linearly the energy of Zeeman levels due to Zeeman effect according to the formula $\Delta E = m_F \mu_B g_F B z$ with μ_B the Bohr magneton and g_F the Landé g-factor of the hyperfine level F. Therefore, the sublevel $m_F = 1$ experiences a shift which is the opposite of $m_F = -1$. In order to simplify this qualitative description, we will take the example of an atom at rest, a ground state $|m_F = 0\rangle$ and three excited states $|m_{F'} = -1\rangle$, $|m_{F'} = 0\rangle$ and $|m_{F'} = 1\rangle$. If the atom is in the center $z = 0$, both beams are not resonant with any atomic transitions as they are detuned by Δ_0 from the excited states. For $z = -z_{lim}$, the σ^+ polarized beam is resonant with the transition $|m_F = 0\rangle \rightarrow |m_{F'} = 1\rangle$. As a result, the radiation pressure force is oriented from $z = -z_{lim}$ to the center $z = 0$. For $z = z_{lim}$, the σ^- polarized beam is resonant with the transition $|m_F = 0\rangle \rightarrow |m_{F'} = -1\rangle$ and applies a force on the atom oriented toward the center. The combination of the cooling beams and magnetic gradient confines the atoms in space and thus acts as a trap. This idea was first proposed by Jean Dalibard in 1985 and experimentally implemented in [Raab et al., 1987].

After this qualitative description, we will evaluate quantitatively this force for atoms with a non-zero velocity and the same energy levels than previous section. The expression of this force is similar than the one described in the equation (1.60)

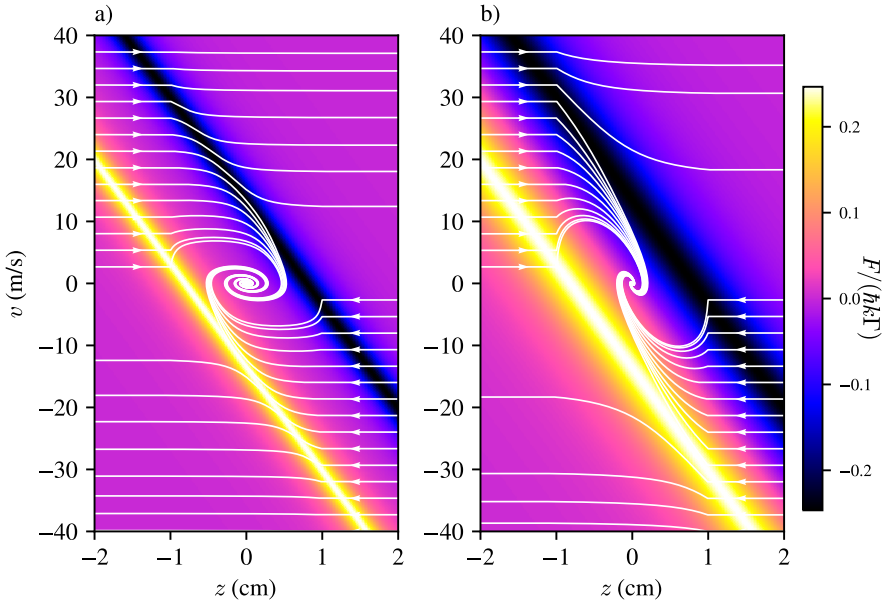

FIGURE 1.12: **Trajectories of atoms in a magneto-optical trap for different initial conditions.** The radius of the cooling beams is set at 1 cm, the detuning to $\Delta_0 = -3\Gamma$ and the magnetic field gradient to 35 G/cm. Atoms are initially placed at $z = -2$ cm with velocities in the range of $[0, 40]$ m/s and also at $z = 2$ cm with velocities in the range of $[0, -40]$ m/s. *a*) represents the trajectories for a saturation parameter $s_0 = 0.5$ and *b*) for $s_0 = 5$. A 2D map of the force applied by the cooling beams on the atomic gas is shown on the background.

with the Zeeman shift included in the detuning between light and atoms:

$$\vec{F} = \frac{\hbar k \Gamma}{2} s_0 \left[\frac{1}{1 + s_0 + 4\frac{(\Delta_0 - kv - \mu_B g B z/\hbar)^2}{\Gamma^2}} - \frac{1}{1 + s_0 + 4\frac{(\Delta_0 + kv + \mu_B g B z/\hbar)^2}{\Gamma^2}} \right] \vec{e}_z \quad (1.62)$$

g being the Landé g-factor of the excited states as the ground state $|m_F = 0\rangle$ is insensitive to magnetic field. In the regime of small displacement ($|z| \ll \hbar\Gamma/(\mu_B g B)$) and small velocities ($|v| \ll \Gamma/k$), the force can be approximated to a linear function of both parameters:

$$\vec{F} \approx -\beta \vec{v} - \kappa \vec{z} \quad \text{with} \quad \kappa = \frac{\mu_B g B}{\hbar k} \beta. \quad (1.63)$$

One can note that the product gB needs to be positive in order to have an attractive force and not a repulsive one. However, one can achieve an attractive force with a negative product gB if the configuration of the cooling beams is changed: the σ^+ polarized beam has to be oriented along $-\vec{e}_z$ and the σ^- polarized beam along $+\vec{e}_z$.

The trajectories of atoms in phase space are presented in figure 1.12 for different initial conditions. The radius of the cooling beams is set at 1 cm, the detuning to $\Delta_0 = -3\Gamma$ and the magnetic field gradient to 35 G/cm which corresponds to our

experimental case at the end of our compression phase (see section 2.1.3). Atoms are initially placed at $z = -2$ cm with velocities in the range of $[0, 40]$ m/s and also at $z = 2$ cm with velocities in the range of $[0, -40]$ m/s. Figure 1.12(a) represents the trajectories for a saturation parameter $s_0 = 0.5$ and figure 1.12(b) for $s_0 = 5$. A 2D map of the force applied by the cooling beams on the atomic gas is shown on the background. An atom is trapped if its trajectory is converging to the center of phase space ($z = 0$, $v = 0$). The velocity capture is defined as the maximum initial velocity for which atoms are trapped. The velocity capture achieved for $s_0 = 0.5$ is $v_c = 20$ m/s and the one for $s_0 = 5$ is $v_c = 31$ m/s. Moreover the number of damped oscillations around the center is higher for $s_0 = 0.5$ than for $s_0 = 5$ meaning that the converging time to the center decreases with s_0. These two observations underlines the importance of having a high saturation parameter ($s_0 \gg 1$) in order to trap atoms with a wide velocity range and cool them down efficiently.

1.3.3 Polarization gradient cooling

The temperature achieved in a magneto-optical trap is limited by the Doppler temperature. However, sub-Doppler cooling has been achieved experimentally [Lett et al., 1988] in 1988. One year later, [Dalibard and Cohen-Tannoudji, 1989] explained the mechanism of this cooling process called polarization gradient cooling (PGC). It involves two beams going in opposite directions without the presence of a magnetic field. Two configurations are possible for the polarizations of these beams: the linear configuration H/V or the circular one σ^+/σ^-. In our experiment, polarization gradient cooling is implemented in the circular configuration as we are using the same beams than the ones set in the magneto-optical trap.

The superposition of two counter-propagating waves, one σ^+ polarized and the other σ^- polarized, is a standing wave with a linear polarization which is rotating in space. As a result, the energy levels of atoms are not modulated in space: the polarization of the standing wave remains linear over all its extent which results in a constant light shift in space. This is the reason why Sisyphus cooling is not possible for the configuration σ^+/σ^- whereas it is effective in the configuration H/V. The mechanism that enables to cool down the gas at a sub-Doppler temperature in the circular configuration is the unbalanced radiation pressure from the two counter-propagating waves. Indeed, if we consider an atom with a velocity $v = zt$, this one will see the linear polarization of the standing wave rotating with an angle $\varphi = kv = kzt$. [Dalibard and Cohen-Tannoudji, 1989] demonstrated that the difference of population between the extreme Zeeman levels of the ground state $\Delta N = N_{m_g=F} - N_{m_g=-F}$ is proportional to $\frac{kv\Delta_0}{\Omega^2}$ with a positive proportionality constant. Assuming that the detuning $\Delta_0 < 0$, an atom moving in the direction $+\vec{e}_z$ ($v > 0$) has more probability to populate $m_g = -F$ than $m_g = F$. The probability for an atom in $m_g = -F$ to absorb a photon from the σ^- beam is higher than the one to absorb a photon from the σ^+ beam due to the imbalance in the Clebsh-Gordan coefficients. This imbalance

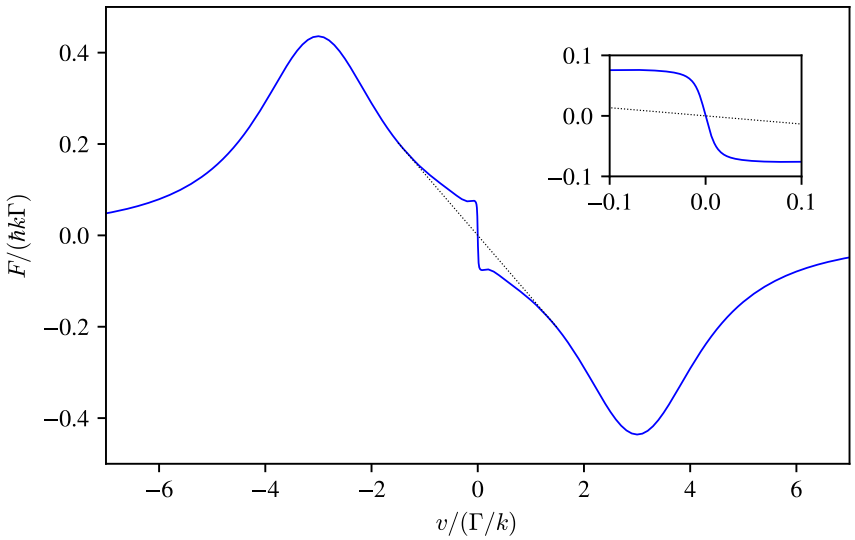

FIGURE 1.13: **Polarization gradient cooling in the σ^+/σ^- configuration.** The force is represented in function of the atom velocity for a ground state $F = 4$ and an excited state $F' = 5$. The saturation parameter chosen is $s_0 = 7$ and the detuning is $\Delta_0 = -3\Gamma$. The signature of the polarization gradient cooling is in the interval $[-0.1, 0.1]\Gamma/k$ shown on the inset of the figure. The dotted line is the slope of Doppler cooling without polarization gradient cooling.

is the cause of the unbalanced radiation pressure from the two counter-propagating waves which results in a damping force oriented toward the opposite direction of the atom velocity. The principle is the same for an atom moving in the direction $-\vec{e}_z$ ($v < 0$): it will populate $m_g = F$ and has more chance to absorb σ^+ polarized photons which results in a force oriented in the direction $+\vec{e}_z$.

The calculation of this force is complex, especially when we are dealing with high F number for the ground state. Nevertheless it can be simulated numerically thanks to the package *PyLCP* presented in [Eckel et al., 2022]. The force is computed for a ground state $F = 4$ and an excited state $F' = 5$ with cooling beams in the σ^+/σ^- configuration. The saturation parameter chosen is $s_0 = 7$ and the detuning is $\Delta_0 = -3\Gamma$ corresponding to our experimental values. The result is represented in figure 1.13. The signature of the polarization gradient cooling is in the interval $[-0.1, 0.1]\Gamma/k$ shown on the inset of the figure. The dotted line is the slope of Doppler cooling without the sub-Doppler mechanism. The value of the slope with polarization gradient cooling is higher by multiple orders of magnitude than the one only due to Doppler cooling. The damping factor β is thus enhanced in the presence of this sub-Doppler cooling. The final temperature calculated by [Dalibard and Cohen-Tannoudji, 1989] is proportional to $\frac{\hbar\Omega^2}{k_B|\Delta_0|}$ which explains why we decrease the intensity of our cooling beams and increase the absolute value of their detuning during the PGC phase of our cooling cycle (see section 2.1.3). Experimentally, we measured a temperature

$T_{PGC} = 20\,\mu$K [Hoffet, 2022] below the Doppler limit $T_D = 125\,\mu$K for cesium atoms.

1.4 Conclusion

This chapter first provided an overview of the different physical platforms currently investigated for quantum memories and a focus on EIT-cold-atom-based memories. Then, the analysis of the EIT protocol underlined the slowdown effect on light illustrated with the dark polariton picture and how this process can be employed to efficiently transfer a photonic state to a collective excitation of the cloud. The decoherence of this excitation was evaluated in presence of residual magnetic fields and dephasing induced by the motion of atoms. Finally, the trapping and cooling methods employed in our experiment were explained, first with the radiation pressure of light beams on the atomic gas and how counter-propagating waves can cool it down up to the Doppler temperature. This damping force can also depend on the atom position by adding magnetic field gradients, leading to a trap. Sub-Doppler temperatures can be reached when the magnetic field is switched off, due to the unbalanced radiation pressure of the counter-propagating beams induced by atomic motion. The implementation of these trapping and cooling methods is presented in Chapter 2.

CHAPTER 2

EXPERIMENTAL IMPLEMENTATION OF A COLD-ATOM BASED QUANTUM MEMORY

Contents

This chapter presents the experimental setup of our cold-atom based quantum memory. The magneto-optical trap implementation is described with the different cooling beams and the main coils generating magnetic-field gradients. The lasers involved in the memory process are also described with their locking setup. Moreover, we examine the critical parameters to enhance the memory efficiency of our storage platform such as the optical depth and the EIT transmission. Finally, a new

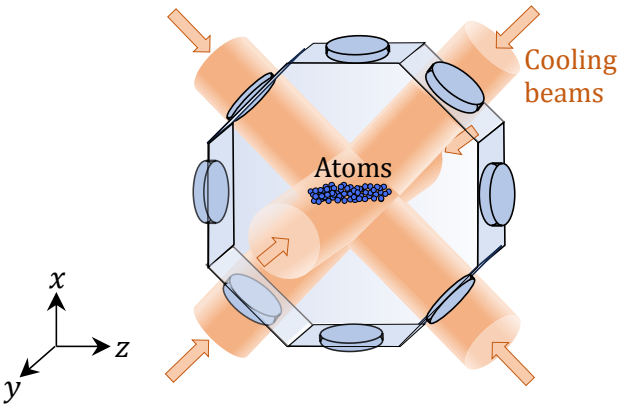

FIGURE 2.1: **Cooling beam configuration around the glass vacuum chamber.** Two inch beams are pointing at the center of the vacuum chamber along the three dimensions of space and retro-reflected to cool down atoms.

compensation system to cancel the residual magnetic field is presented leading to an improvement of the memory lifetime.

This experiment started almost ten years ago and several former members of the group contributed to its improvement years after years. Interesting details are available in their respective PhD thesis [Veissier, 2013], [Giner, 2013], [Nicolas, 2014], [Vernaz-Gris, 2018], [Hoffet, 2022].

2.1 Magneto-optical trap

A magneto-optical trap (MOT) operates by combining laser cooling and magnetic-field gradients to slow down and confine atoms within a small region of space (see section 1.3.2). First, we describe the atomic transitions used for laser cooling. Secondly, we characterize magnetic-field gradients created by the two pairs of rectangular coils that are employed to generate a quasi 2D-MOT. Finally, the sequence of the experiment is presented.

2.1.1 Cooling beams

The light used for the cooling process is produced by a Ti:sapphire laser (MSquared, SolsTiS). Two inch beams coming from this laser are pointing at the center of the vacuum chamber along the three dimensions of space (see figure 2.1). One mirror is positioned in front of each beam to produce a counterpropagating wave required to cool down atoms moving in the opposite direction. The light is circularly polarized thanks to quarter waveplates. The total optical power of the trapping beams is around 350 mW. Their frequency is given by the atomic transitions of the Cesium D2 line (see figure 2.2). The trapping light is red detuned from the cycling transition $|6S_{1/2}, F = 4\rangle \rightarrow |6P_{3/2}, F' = 5\rangle$ by 17 MHz corresponding to about three times the linewidth of the transition. Due to off-resonant scattering from $|6P_{3/2}, F' = 4\rangle$, a part of the atoms decays in the level $|6S_{1/2}, F = 3\rangle$ and are not anymore in the

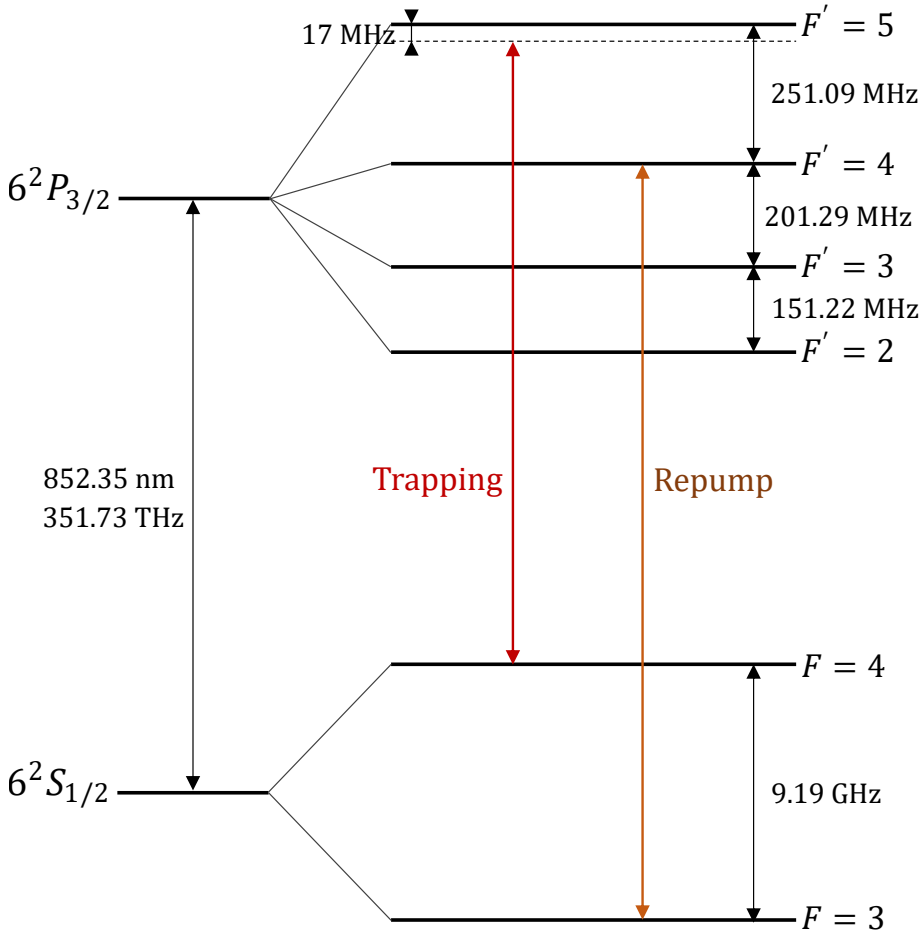

FIGURE 2.2: **Cooling beams addressing different transitions of the Cesium D2 line.** The trapping laser is red detuned from the cycling transition $|6S_{1/2}, F = 4\rangle \rightarrow |6P_{3/2}, F' = 5\rangle$ by 17 MHz to compensate for the Doppler shift of atoms moving toward the incoming light. The repump beam is resonant with the transition $|6S_{1/2}, F = 3\rangle \rightarrow |6P_{3/2}, F' = 4\rangle$ and enables the atoms which are in the level $|6S_{1/2}, F = 3\rangle$ to get back into the cooling process.

cooling cycle. In order to overcome this issue, we use a repump beam resonant with the transition $|6S_{1/2}, F = 3\rangle \rightarrow |6P_{3/2}, F' = 4\rangle$ to transfer the atoms back to the level $|6S_{1/2}, F = 4\rangle$. The repump laser is sent in the same directions than the trapping laser and has a total optical power of 4 mW.

2.1.2 MOT coils: characterization and implementation

Coils in an anti-Helmholtz configuration are the second ingredient to implement a magneto-optical trap. A pair of coils in this specific configuration generates a magnetic field gradient along each dimension of space. The value of this gradient defines the boundaries of the trap in each direction (see section 1.3.2). In our experiment, we are using two pairs of rectangular coils as it allows to achieve high gradients along two dimensions (called the transverse axes of the atomic cloud) and a low one on the last dimension (longitudinal axis of the cloud). As a result, we obtain a quasi 2D-MOT, leading to a very elongated cold-atomic ensemble. The purpose of having an elongated ensemble is to reach a higher optical depth [Lin et al., 2008] along the longitudinal axis (z-axis in figure 2.1), i.e. along the direction of the signal propagation.

During the course of my doctoral research, we observed short-circuits in the main coils used for the MOT. Therefore, we had to replace the coils for safety reasons. We took advantage of this change to enhance their performances. The first improvement was to increase the number of wire turns from 90 to 110 turns. Higher number of turns enables us to reach larger magnetic field gradients keeping the same value of current injected into the coils. The second was on optimizing the wire radius. A large wire radius is required for high current, especially in our experiment as the current reaches 18 A during the cooling phase (see section 2.1.3). However, the volume available for the wires on the coil holder is limited. Taking into account these two constraints, we chose a wire radius of 0.8 mm (compared to 0.7 mm for the previous coils). Each coil was made by stacking 10 layers of 11 turns (10×11). Thermal paste (RSpro) was spread between the layers for enhanced thermal dissipation, and also epoxy (Loctite 3430) to stick the layers tightly together (see figure 2.3(a)).

After winding the coils, we characterized them by measuring their resistance and their inductance. We used a multimeter to determine the value of the resistance R for each coil. In order to measure the inductance, we built a RL circuit, using a resistance r with a well known value, and a function generator which produced a sinusoidal waveform. By looking to the dephasing φ between the voltage around the resistance V_r and the voltage given by the function generator V_{in}, we can calculate the inductance with the following expression: $L = \frac{(r+R)\cdot|\tan(\varphi)|}{2\pi f}$, f being the frequency of the input sinusoidal signal. After scanning this frequency, we found the one corresponding to the dephasing $\varphi = \pi/4$ and determined the value of the inductance for the four coils.

a) b)

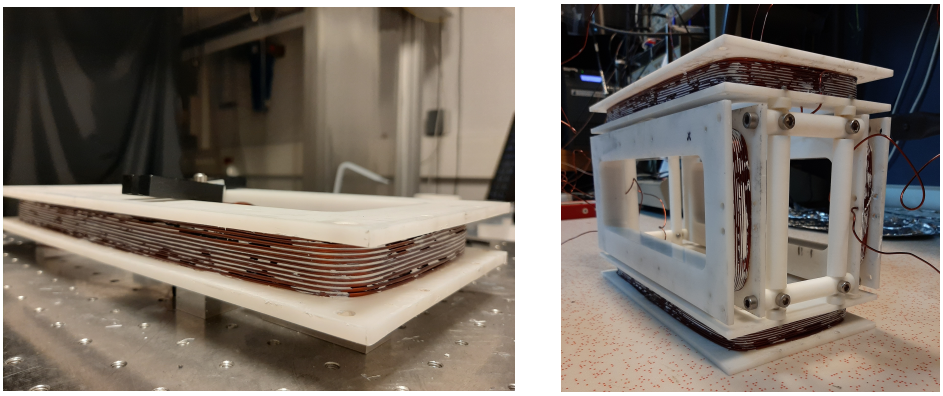

FIGURE 2.3: **Rectangular coils used for the magneto-optical trap.** *a*) One rectangular coil composed of a hundred and ten turns of wire. The wires are glued between each other with epoxy and thermal paste is applied on each layer of wire to enable a good heat exchange inside the coil. The rectangular coil has a width of 12 cm and a length of 28 cm. *b*) Two pairs of rectangular coils in an anti-Helmholtz configuration used for the magneto-optical trap. The horizontal pair of coils is spaced by 12 cm and the vertical one is spaced by 16 cm.

Position	Bottom	Top	Left	Right
L	3.9 mH	4.2 mH	4.1 mH	4.1 mH
R	0.8 Ω	0.8 Ω	0.8 Ω	0.8 Ω

TABLE 2.1: Measurements of the resistance R and the inductance L for each coil.

The table 2.1 shows the values of the resistance R and the inductance L for each coil. The position given in this table is the one corresponding to the configuration given by figure 2.3(b).

After characterizing them separately, the coils were assembled together as shown in figure 2.3(b). The horizontal pair is spaced by 12 cm while the vertical one is spaced by 16 cm. Then, we measured the magnetic field gradient created by the two pairs of coils in an anti-Helmholtz configuration (i.e. the configuration of the magneto-optical trap) along two different axis (see figure 2.4). Only one of the transverse axes has been measured (x axis) because the other (y axis) has the same value of gradient due to our configuration [Giner, 2013]. For this purpose, a magnetic field sensor was placed at the center of the magnetic cage and was attached to a translation stage to scan the two axis. Figure 2.4 shows a magnetic field gradient of 5.8 G/cm along the transverse direction of the magneto-optical trap and a gradient of 0.4 G/cm along the longitudinal direction, for a current $I = 3$A circulating inside each pair of coils. If the two pairs of coils have the same spacing, the gradient along the z axis should be equal to zero, and no trapping could be possible in this direction. In our case, the spacing between the two pairs is not the same, and for this particular reason, a small gradient appears along the z axis.

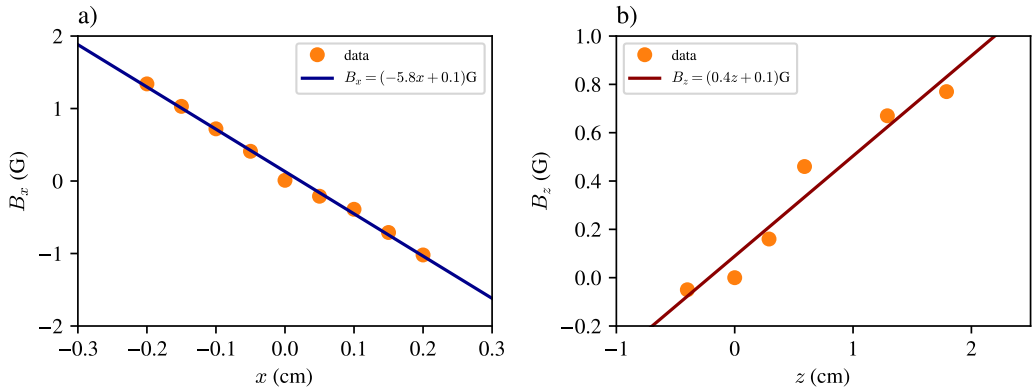

FIGURE 2.4: **Magnetic field gradient created by the two pairs of rectangular coils in an anti-Helmholtz configuration.** *a*) Magnetic field measured in the transverse direction of the magneto-optical trap. A linear fit shows a magnetic field gradient of 5.8 G/cm for a current $I = 3$ A circulating inside each pair of coils. *b*) Magnetic field measured in the longitudinal direction of the magneto-optical trap. A linear fit shows a magnetic field gradient of 0.4 G/cm for a current $I = 3$ A circulating inside each pair of coils.

2.1.3 Sequence of the experiment

The experiment is working on an optimized cycle of 120 ms described in figure 2.5. First, a loading phase of 108 ms begins, in which all the parameters are set in a continuous mode. The magnetic field gradient in the transverse axis is at 6 G/cm and the longitudinal one is around 0.4 G/cm. The total trapping power is around 350 mW with an intensity of 17 mW/cm^2. The trapping beam is red detuned from the cycling transition by 17 MHz. The total repump power is around 4 mW with an intensity of 0.2 mW/cm^2. Then, a compression phase is initiated and lasts 8 ms. During this phase, the magnetic field gradient is increased gradually from 6 to 35 G/cm. The purpose of this step is to enhance the density of atoms along the longitudinal direction [Petrich et al., 1994]. It leads to better optical depth[1] and then enables us to increase the memory efficiency. When the compression stage is finished, the magnetic field is turned off and we perform polarization gradient cooling (PGC) on our atomic cloud during 2 ms (see section 1.3.3). To do so, we ramp down the trapping and repump power to zero with an exponential decay. The trapping detuning is also decreasing exponentially from -17 to -107 MHz. The aim of this PGC phase is to cool down atoms to about $T = 20\,\mu$K. At the end of this phase, the cold-atom memory has optimal properties for the storage process. The "Memory" stage lasts 2 ms (in practice, we are only using 1 ms of this time interval for our experiment to keep a high optical depth). In this sequence, we don't use a depump laser to transfer our atoms from $|6S_{1/2}, F = 4\rangle$ to $|6S_{1/2}, F = 3\rangle$. Indeed, as the extinction time for

[1] In our case, the size of the cloud in the longitudinal direction is limited by the waist of our trapping beams. As a result, the length of the ensemble remains the same after compression and its density increases leading to a better optical depth.

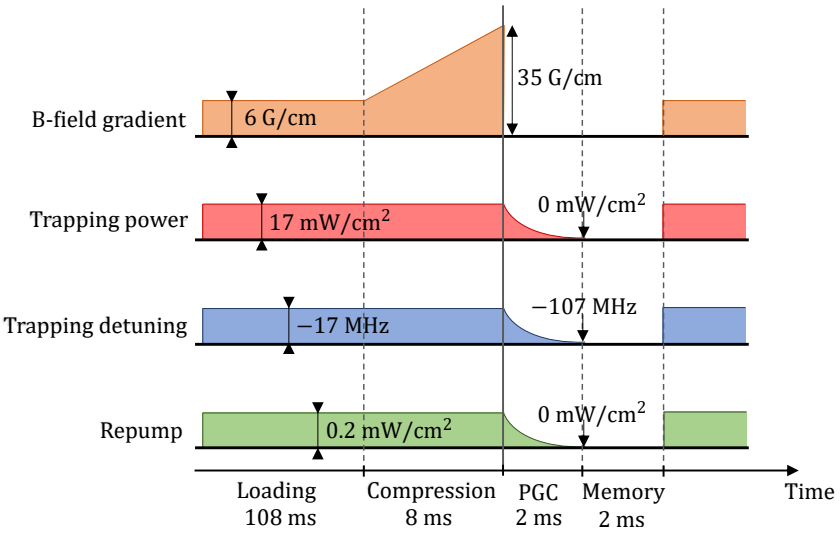

FIGURE 2.5: **Temporal sequence of the experiment.** First, a loading phase of 108 ms begins, in which all the parameters are set in a continuous mode to prepare the MOT. Then, a compression phase is initiated and lasts 8 ms. During this phase, the magnetic field gradient is increased gradually from 6 to 35 G/cm. When the compression stage is finished, the magnetic field is turned off and we perform polarization gradient cooling (PGC) on our atomic cloud during 2 ms by ramping down the trapping power, the trapping detuning and the repump power, following an exponential decay. Then, the cold-atom memory has optimal properties for the storage process. The "Memory" stage lasts 2 ms.

the trapping power is 1 ms longer than the one for the repump power, all the atoms already transferred to $|6S_{1/2}, F = 3\rangle$ at the end of the PGC stage.

The figure 2.6 shows the fluorescence of cesium atoms inside the elongated magneto-optical trap. This fluorescence is the spontaneous emission of atoms scattering photons during the cooling cycle. The atomic cloud is around 2.5 centimeters long with a transverse size which is on the order of a millimeter.

2.2 Lasers for the memory process

The storage-and-retrieval process requires the use of two different lasers. The first one is called the signal and represents the light which is going to be stored in the memory. The second one is called the control and is responsible of the EIT window opening. The control acts as a light switch when the signal pulse is inside the cloud: by turning it off, the signal photons are converted into a collective excitation of the cold atoms, and by turning it on, this excitation is converted back into the original signal photons (see section 1.2.3). The signal and the control beams are generated by semiconductor laser diodes (Toptica Photonics, DL100).

FIGURE 2.6: **Fluorescence of cesium atoms inside the elongated magneto-optical trap.** The fluorescence of cesium atoms is represented by the bright area at the center of the vacuum chamber.

2.2.1 Cesium D1 line compared to cesium D2 line

The choice of transitions for the lasers used in the memory process is significant if we want to achieve an optimal storage-and-retrieval efficiency. Previously in the group, EIT was implemented on the D2 line of Cesium (the excited state used was $|e\rangle = |6P_{3/2}, F' = 4\rangle$). Nevertheless, the hyperfine structure of this D2 line was a limitation in order to access efficiencies above 70% [Vernaz-Gris et al., 2018].

A quantitative analysis has been done in our group to compare the efficiency of D1 and D2 lines [Vernaz-Gris et al., 2018]. The results are presented in figure 2.7(b). The D2 line shows a limitation of the maximum memory efficiency (65% corresponding for an OD equal to 200) compared to the D1 line. Indeed, the memory efficiency scales as $e^{-2\gamma_{gs}T_d}$ [Hsiao et al., 2018], with T_d the group delay and γ_{gs} the ground state decoherence rate. This decoherence rate is increased by off-resonant coupling to the adjacent excited states. The adjacent excited states are $|6P_{3/2}, F' = 3\rangle$ and $|6P_{3/2}, F' = 5\rangle$ for D2 line (see figure 2.2) and $|6P_{1/2}, F' = 3\rangle$ for D1 line (see figure 2.7(a)). The off-resonant coupling is larger for the D2 line than the D1 line as the hyperfine splittings in the excited states are four times smaller leading to $\gamma_{gs}^{D2} > \gamma_{gs}^{D1}$. Therefore, the memory process becomes less efficient for the D2 line than for D1. Moreover, the efficiency decreases for high values of OD as the off-resonant coupling is enhanced. This effect is negligible in the case of the D1 line. To conclude, the D1 line enables a better memory efficiency than the D2 line with no limitations in the regime of high optical depth. Experimental demonstrations of quantum memories on the D1 transitions showed storage-and-retrieval efficiency up to 90% [Cao et al., 2020; Wang et al., 2019].

2.2.2 Implementation of the signal lock

The signal frequency must be locked on the transition $|6S_{1/2}, F = 3\rangle \rightarrow |6P_{1/2}, F' = 4\rangle$ as presented in figure 2.7(a). Previously on the experiment, the signal frequency

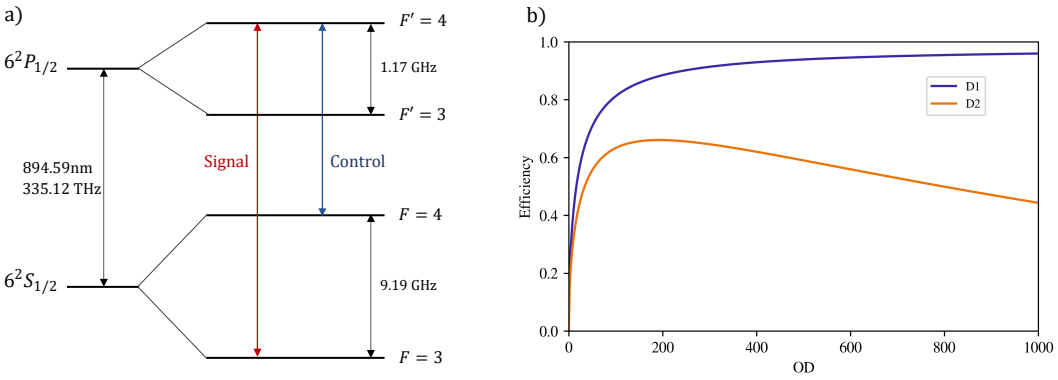

FIGURE 2.7: **Advantage of the D1 line compared to the D2 line for the memory process.** *a)* Lasers used for the memory process addressing different transitions of the Cesium D1 line. The signal beam is resonant with the transition $\left|6S_{1/2}, F = 3\right\rangle \rightarrow \left|6P_{1/2}, F' = 4\right\rangle$ and the control beam is resonant with the transition $\left|6S_{1/2}, F = 4\right\rangle \rightarrow \left|6P_{1/2}, F' = 4\right\rangle$. *b)* Memory efficiency as a function of the optical depth (OD) for the Cesium D1 and D2 lines. This simulation was done for an intrinsic ground state decoherence $\gamma_0 = 10^{-3}\Gamma$ and a residual magnetic field gradient $B_0 = 8\,mG/cm^{-1}$, a cloud length $L = 2.5\,\text{cm}$. The temporal duration of the signal pulse is $\tau = 500\,\text{ns}$ and the pulse delay is fixed to $T_d = 2\tau$.

was locked thanks to an error signal obtained by modulating the current of the laser diode. However this method was not optimal for the storage process as the signal sent to the memory is frequency modulated, even after being locked. As a result, we implemented a locking setup with an external modulation done by an AOM (acouto-optic modulator) to achieve a fixed frequency for the light sent to the memory [Zhang et al., 2009].

Before explaining the locking setup, an introduction to saturated absorption spectroscopy is required. We consider a probe beam with a weak intensity propagating in a vapor cell. If we monitor the transmission of the probe after the vapor cell, absorption will occur at the atomic resonances. However, the linewidth of the absorption profile is larger than the natural linewidth of the atomic levels due to Doppler broadening. If the frequency difference between two resonances is smaller than the Doppler broadening profile, they can not be distinguished. To fix this issue, we are using a high intensity pump beam going in the opposite direction of the probe. The two beams are overlapping in the vapor cell. Three cases need to be examined to understand the principle of the saturated absorption spectroscopy: atoms moving in the direction of the pump beam, atoms moving in the direction of the probe beam and atoms with no velocity along the propagation axis of light. For the first case and the second case, the probe is absorbed as the pump is not resonant with the same atoms than the probe due to their opposite Doppler shift. Only atoms with no velocity will be resonant with the two beams. As these atoms are saturated by the pump, they are transparent to the probe leading to narrow transmission peaks centered at atomic

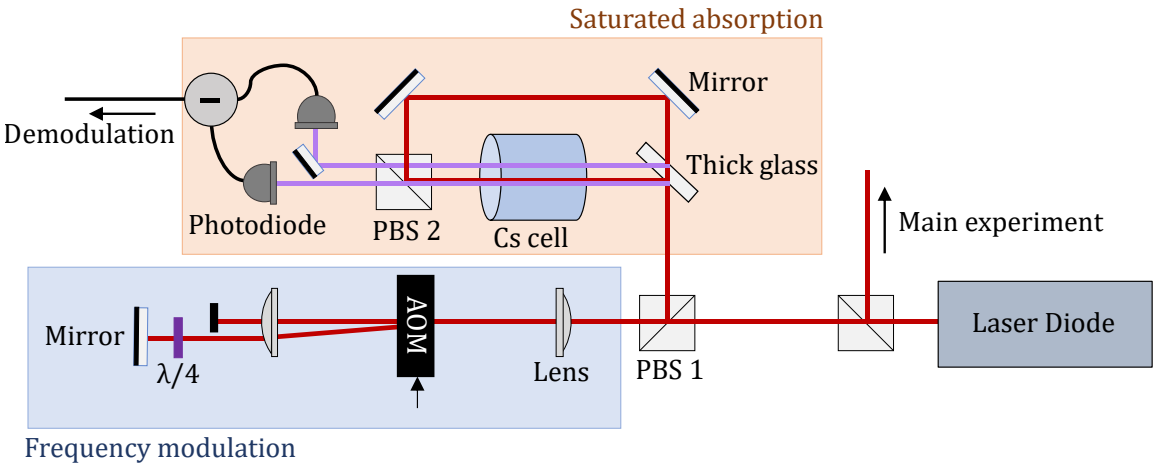

FIGURE 2.8: **Locking setup of the signal.** The laser is modulated in frequency thanks to an acousto-optic modulator (AOM). Then, the light enters in the saturated absorption setup: ten percent of it is reflected by the thick glass (one reflection at each interface) and ninety percent is transmitted. The transmitted beam is overlapping one of the reflection inside the vapor cell to perform saturated absorption spectroscopy. The other reflection is used to subtract the Doppler profile from the saturated absorption profile. The signal detected on the photodiodes is demodulated to create the error signal used to lock the laser.

resonances. Therefore, this spectroscopy overcomes the issue of Doppler broadening by only addressing atoms with a very low speed range.

The locking setup is presented in figure 2.8. First, we separate the light going to the memory from the one going to the locking part. Then the light is transmitted through the PBS1 (polarization beam-splitter) to go through an AOM. The AOM is frequency modulated with a signal $S = S_0 \cos(\Omega_m t + \varphi_m)$. We select the -1 diffraction order of the AOM two times (the second time being after reflecting on the mirror). The light frequency thus changes from ω to $\omega - 2\omega_m \cos(\Omega_m t + \varphi_m)$, with ω_m the amplitude of the modulation which is proportional to S_0. After being frequency modulated, the laser is reflected by the PBS1 and enters into the saturated absorption setup. Ten percent of the light is reflected by the thick glass (one reflection at each interface) and ninety percent is transmitted. In order to make the link with the description of the saturated absorption given above, the reflected beams are the probes (purple beams) and the transmitted beam is the pump. Only one probe will overlap with the pump in the vapor cell. The other is used to subtract the Doppler profile from the saturated absorption profile after detection on the photodiodes (blue waveform on figure 2.9).

Nevertheless, we need an error signal to lock the laser. The error signal is the derivative of the saturated absorption signal along the frequency axis. This derivative could be calculated by demodulating the signal received by the photodiodes after subtraction S_{sub}. Indeed, supposing that the amplitude of the modulation is small compared to the optical frequency ω, we can use a Taylor expansion at the first order

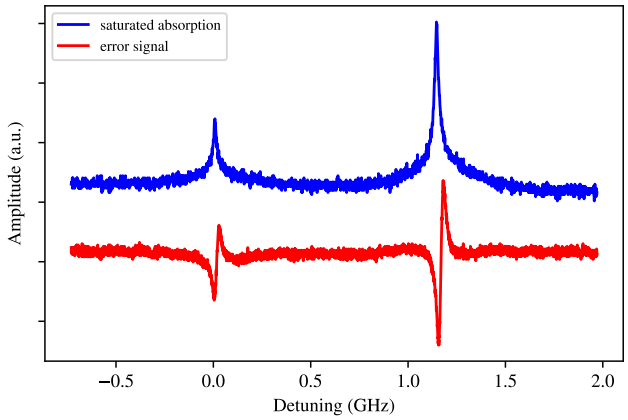

FIGURE 2.9: **Error signal for the locking of the signal laser.** The blue waveform represents the saturated absorption spectroscopy with Doppler subtraction. The left peak is the transition $|6S_{1/2}, F = 3\rangle \rightarrow |6P_{1/2}, F' = 3\rangle$ and the right one is the transition $|6S_{1/2}, F = 3\rangle \rightarrow |6P_{1/2}, F' = 4\rangle$. The error signal corresponding to these two peaks is represented by the red waveform.

to express S_{sub}:

$$S_{\text{sub}}(\omega - 2\omega_{\text{m}} \cos(\Omega_{\text{m}} t + \varphi_{\text{m}})) \approx S_{\text{sub}}(\omega) - \frac{dS_{\text{sub}}}{d\omega} \cdot 2\omega_{\text{m}} \cos(\Omega_{\text{m}} t + \varphi_{\text{m}}) \tag{2.1}$$

The first term at the frequency ω is independent of time because of the average done by the photodiodes, as their bandwidths (on the order of MHz) are smaller than the optical frequency (335 THz). This continuous component is suppressed by a high-pass filter. In order to demodulate S_{sub}, we need to multiply it to a demodulation signal $S_{\text{dem}} = S^0_{\text{dem}} \cos(\Omega_{\text{dem}} t + \varphi_{\text{dem}})$. The calculations lead to the following expression:

$$\begin{aligned} S_{\text{dem}} \cdot S_{\text{sub}} = -\omega_{\text{m}} S^0_{\text{dem}} \frac{dS_{\text{sub}}}{d\omega} [&\cos(\Omega_{\text{m}} + \Omega_{\text{dem}})t + (\varphi_{\text{m}} + \varphi_{\text{dem}}) \\ &+ \cos(\Omega_{\text{m}} - \Omega_{\text{dem}})t + (\varphi_{\text{m}} - \varphi_{\text{dem}})] \end{aligned} \tag{2.2}$$

The demodulation frequency and phase are set to be the same than the modulation ($\Omega_{\text{m}} = \Omega_{\text{dem}}$ and $\varphi_{\text{m}} = \varphi_{\text{dem}}$). The product of the two signals go through a low-pass filter to get rid of the oscillating term at $2\Omega_{\text{m}}$. The final expression of the resulting signal after demodulation is:

$$S_{\text{dem}} \cdot S_{\text{sub}} = -\omega_{\text{m}} S^0_{\text{dem}} \frac{dS_{\text{sub}}}{d\omega} \tag{2.3}$$

The most important factor in this expression is $dS_{\text{sub}}/d\omega$, i.e. the derivative of the saturated absorption signal along the frequency axis. Therefore, after demodulation we obtain an error signal that could be used to lock our laser. The device employed for the demodulation and filters is a Lock-In Amplifier (SR830). The experimental error

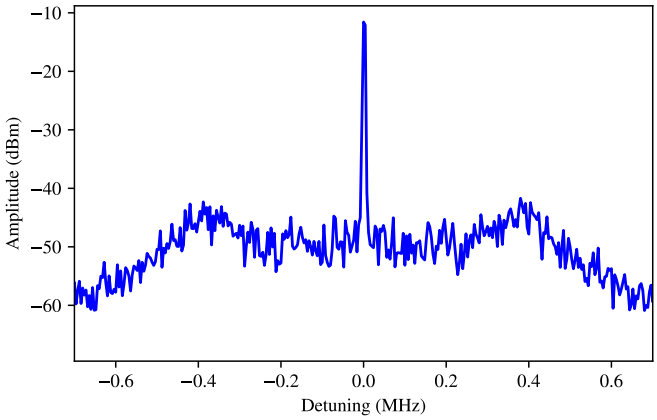

FIGURE 2.10: **Beatnote between signal and control lasers for phase locking.** The figure shows a central peak at zero detuning and servo bumps at ±400 kHz. The width of the central peak is limited by the resolution bandwidth of the spectrum analyser (3 kHz) and its amplitude is 30 dBm above the servo-bump amplitude.

signal achieved is shown on figure 2.9. The blue waveform represents the saturated absorption spectroscopy with Doppler subtraction. The left peak is the transition $|6S_{1/2}, F = 3\rangle \rightarrow |6P_{1/2}, F' = 3\rangle$ and the right one is the transition $|6S_{1/2}, F = 3\rangle \rightarrow |6P_{1/2}, F' = 4\rangle$. The error signal of these two peaks is represented by the red waveform. The right peak corresponds to the transition on which we are going to lock the signal laser ($|6S_{1/2}, F = 3\rangle \rightarrow |6P_{1/2}, F' = 4\rangle$) .

2.2.3 Phase lock between the control and the signal

The control laser is phase-locked with the signal laser in order to maintain a good coherence between the two beams during the storage process. To perform this phase locking, the two lasers are combined in a single-mode fiber which is linked to an ultra-fast photodiode (Thorlabs, DX20AF) with a bandwidth equal to 20 GHz. The two beams interfere in the fiber leading to a continuous component (the sum of the intensities of both lasers) and an oscillating component (called the beatnote) at the frequency $\omega_{\text{signal}} - \omega_{\text{control}}$. The photodiode was chosen to have a bandwidth higher than 9.19 GHz which corresponds to the frequency difference between the signal and control transitions (see figure 2.7(a)). The output of the photodiode goes through an amplification stage of 30 dB and is sent to a device (Vescent, D2-135) locking the frequency and phase of the beatnote to a reference microwave signal set at 9.19 GHz. After being phase locked, the beatnote between the signal and the control lasers is shown on figure 2.10. This beatnote was measured with a spectrum analyser (R&S, FSL18) which is able to detect frequencies up to 18 GHz. The resolution bandwidth used to visualize the beatnote is equals to 3 kHz. The figure shows a central peak at zero detuning and servo bumps[2] at ±400 kHz. The width of the central peak is

[2]These servo bumps occur when the phase delay of the feedback signal exceeds π, resulting in a transition from negative to positive feedback.

limited by the resolution bandwidth of the spectrum analyser and its amplitude is 30 dBm above the servo-bump amplitude.

After locking the signal and control lasers, we can begin the experimental procedure to optimize the memory efficiency (section 2.3) and the memory lifetime (section 2.4).

2.3 Optimizing the memory efficiency

In the context of quantum networks, the entanglement rate between the two ends of a communication line highly depends on the memory efficiency η as it affects the rate of entanglement swapping operations [Sangouard et al., 2011]. Moreover, achieving a high memory efficiency enables a range of cryptographic protocols to operate in the secure regime as losses introduced by the memory can be exploited by malicious parties (see Chapter 3). The focus of this section is on the experimental parameters that can be optimized to increase the storage-and-retrieval efficiency.

2.3.1 OD measurement

The optical depth is the first crucial parameter to optimize in order to increase the memory efficiency. A previous section about the comparison of the D1 and D2 lines shows the relation between the optical depth and the memory efficiency (see figure 2.7(b)). On the D1 line, the efficiency increases with the OD whereas on the D2 line, the efficiency decreases for an OD higher than 200 due to off-resonant coupling to the other excited states. Furthermore, the product between the bandwidth of the quantum memory and the temporal delay induced by EIT only depends on the optical depth. Therefore, an OD optimization is required to enhance the performance of our cold-atom memory.

Figure 2.11 shows the setup used to measure the optical depth of our atomic cloud. The light beam is separated in two paths thanks to the BS (beam-splitter). One of the paths leads to the reference photodiode (PD_{ref}) to monitor the optical power before absorption by the cesium atoms. The beam probing the cloud is focused inside the chamber thanks to a convex lens (L_1). The aim of using L_1 is to reduce the signal waist at the center of the MOT in order to achieve a better optical depth. Before L_1, the signal waist is about $w_0 = 1\,\text{mm}$. The atomic density in the transverse plane can be simplified to a Gaussian profile given by $n \propto e^{-2r^2/(\sigma_t^2)}$ with $\sigma_t \approx 500\,\mu\text{m}$ (we can call σ_t the atomic waist). As a result, the signal waist before L_1 is twice the atomic waist. If w_0 is reduced, the beam could entirely fit in the center of the cloud transverse plane where the atomic density is higher. The focal length of L_1 is $f' = 50\,\text{cm}$ and leads to $w_0 = 126\,\mu\text{m}$ which is four times less than σ_t. An additional photodiode PD_{out} is placed after the chamber to measure transmission through the atomic ensemble.

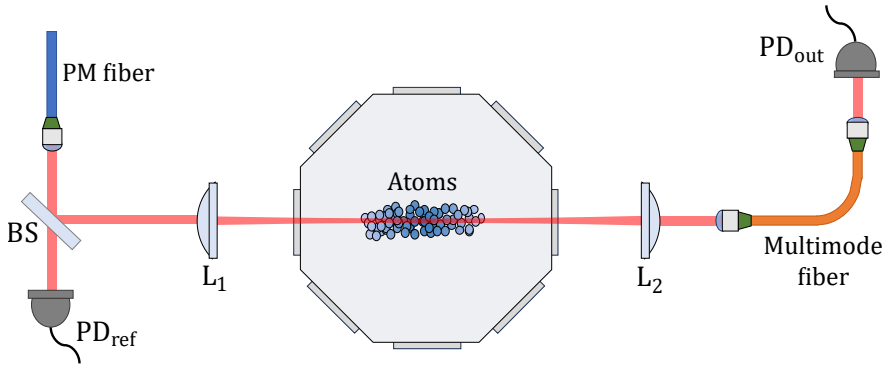

FIGURE 2.11: **OD measurement setup.** The light beam is separated in two paths thanks to the BS (beam-splitter). One of the paths leads to the reference photodiode (PD_{ref}) to monitor the optical power before absorption by the cesium atoms. The other beam is focused inside the cloud thanks to a convex lens L_1 with a focal lenth $f' = 50\,\text{cm}$. An additional photodiode PD_{out} is placed after the chamber to measure the fraction of light absorbed by the atoms.

Another constraint to be satisfied to measure properly the OD is to be below the saturation intensity of the signal transition I_{sat}. For the D1 line, I_{sat} is on the order of $1\ \text{mW/cm}^2$ [Steck, 1998]. The typical power used for our OD measurements is about $P = 10\,\text{nW}$. The corresponding intensity for a Gaussian beam is $I = 2P/\pi w_0^2 = 0.04\,\text{mW/cm}^2$ which confirms that we are in the non-saturated regime ($I \ll I_{sat}$).

The OD measurement is done by measuring the transmission of the signal going through the cloud for different signal detunings around the atomic resonance. The detunings are applied by an AOM on the signal. Measurements for detunings below than the linewidth of the transition are not accurate because the medium is so absorptive that the transmitted light has a power on the order of the photodiode dark counts. This is the reason why we are measuring the transmission for a wide range of frequencies around the atomic resonance (range of 100 MHz). The result is presented on figure 2.12. The red points represent the experimental data and the blue curve represents the theoretical model. This measurement has been done in the pulsed regime: the length of the signal pulse is $30\,\mu\text{s}$ with a square waveform. The formula explained in the first chapter (see section 1.2.1) and used for the model is the following:

$$T(d, \Delta) = \exp\left(\frac{-d}{1 + 4(\frac{\Delta}{\Gamma})^2}\right) \tag{2.4}$$

with d the OD, Δ the signal detuning from the resonance and Γ the linewidth of the transition. A fit between the experimental data and the model gives the value for the OD of 520 ± 10. One can see a gap between the data and the model for detunings below $-30\,\text{MHz}$ and above $30\,\text{MHz}$. Indeed, the atomic cloud produces a lensing effect that depends on light frequency due to the dispersion of the medium and thus modifies the coupling of the signal inside the multimode fiber leading to PD_{out}. The

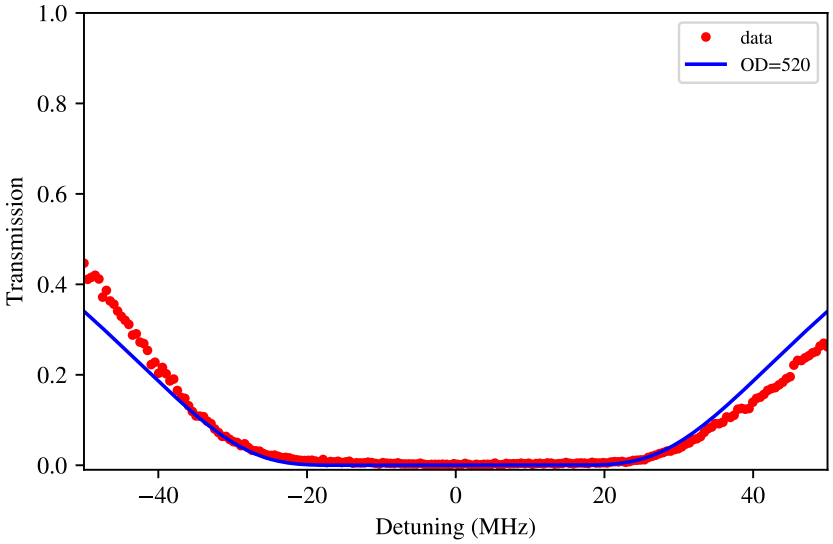

FIGURE 2.12: **OD measurement.** The OD measurement is done by measuring the transmission of the signal going through the cloud for a wide range of signal detunings around the atomic resonance. The red points represent the experimental data and the blue curve represents the theoretical model with a fitting OD of 520 ± 10. This measurement was done 2 ms after the magnetic field extinction.

fiber was chosen to be multimode in order to minimize this effect as its core is larger than a single-mode fiber.

High optical depth was achieved by optimizing the orientation of the trapping beams to increase the overlap between the cloud and the signal beam. Other parameters of the experiment enter into account in the optimization such as the trapping beam detuning, the power of the repump beam, the exponential decays of the cooling beams during the PGC phase (see figure 2.5). This measurement was done 2 ms after the magnetic field extinction. In our experiment, the memory is used between 2 ms and 3 ms after the extinction. The OD decreases by 10% typically during this interval of 1 ms due to the initial velocity of the atoms and also gravity as the trap is turned off. The OD decay time is a good witness to calculate the temperature of the cold atoms [Hoffet, 2022]. After a PGC phase, the typical temperature of our cloud is around $20\,\mu$K.

2.3.2 EIT measurement

After optimizing the optical depth seen by the probe, the next step is to measure EIT. The EIT configuration is presented on figure 2.13. The control beam is the additional laser responsible for the opening of the EIT window. The control and the signal are not set to be colinear as it would directly couple the control to the detectors. The angle between the two beams is equal to 1°. We kept a small angle to limit the motional dephasing (see section 1.2.4). However, some groups working

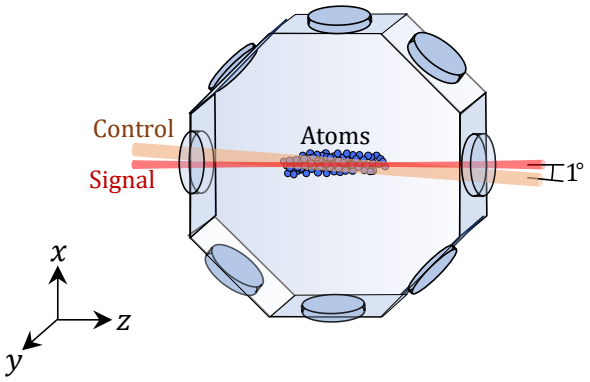

FIGURE 2.13: **EIT configuration.** The control is the additional laser responsible for the opening of the EIT window. The angle between the two beams is equal to 1°. The peak transmission of the EIT window is determined by the overlap between the two beams and the atomic cloud.

with hot vapors [Dideriksen et al., 2021; Namazi et al., 2017a; Reim et al., 2011] have to set them colinear as the motional dephasing increases drastically with the temperature of atoms. In this case, multiple Fabry-Perot cavities (FPC) in cascade are required to filter out the control, which significantly reduces the transmission of the detection setup. In our experiment, only one FPC is sufficient due to the angle between the beams.

The EIT window is shown on figure 2.14. The transmission of the signal beam through the cloud is measured as a function of the signal detuning. The red points represent the experimental data and the blue curve represents the theoretical model. The signal pulse duration chosen for this measurement is $30\,\mu$s. The control beam was turned on before the arrival of the signal pulse on the atoms and turned off after the exit of this pulse from the atomic medium. The peak transmission at zero detuning T_0 of the EIT window can be optimized by playing on the overlap between the two beams and the atomic cloud. Indeed, any atom on the signal path which is not interacting with the control beam is going to absorb the signal photons and decrease the transmission. The width of the EIT window $\Delta\nu_{\mathrm{EIT}}$ depends on the Rabi frequency Ω_c of the control field and the optical depth d. The formula explained in the first chapter (see section 1.2.2) and used for the model is the following:

$$T(\Omega_c,\Delta) = T_0 e^{-dIm(\chi)} \ , \ \chi(\Omega_c,\Delta) = \frac{\gamma_{ge}(\Delta + i\gamma_{gs})}{\Omega_c^2/4 + \gamma_{ge}\gamma_{gs} - i\Delta(\gamma_{ge}+\gamma_{gs}) - \Delta^2} \tag{2.5}$$

with χ the susceptibility of the atomic medium, Δ the signal detuning from the resonance, γ_{ge} and γ_{gs} the relaxation rate of the coherence between the levels $\{g,e\}$ and $\{g,s\}$ ($\gamma_{ge} = \Gamma/2$). A fit between the experimental data and the model gives the value for Rabi frequency of the control field equal to $\Omega_c = 2\pi\cdot(19.1\pm0.1)\,$MHz. This value is obtained for an optical depth of 450, a control power of 3 mW and a control

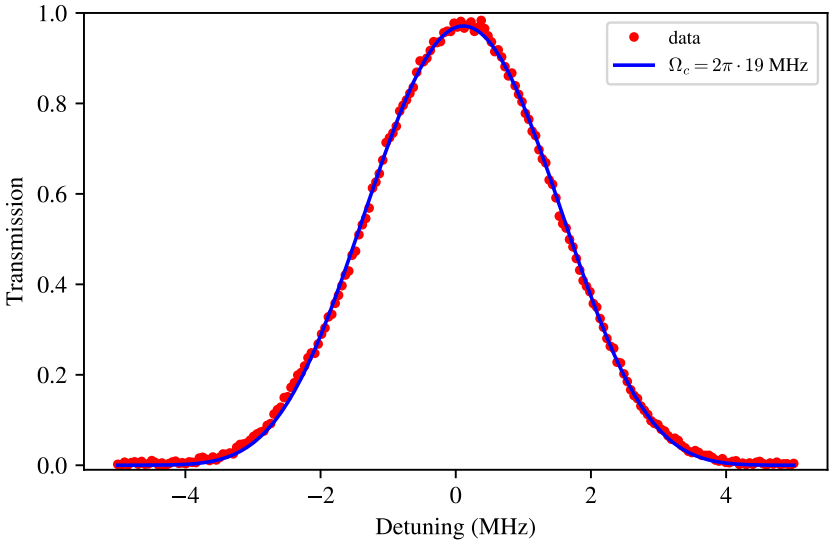

FIGURE 2.14: **EIT measurement.** The transmission of the signal through the cloud is measured as a function of the signal detuning while the control is turned on. The red points represent the experimental data and the blue curve represents the theoretical model with a fitting Rabi frequency for the control field equal to $\Omega_c = 2\pi \cdot (19.1 \pm 0.1)$MHz. This value is obtained for an optical depth of 450 ± 10.

waist of 1 mm. The polarisation of the signal and the control are optimized to be the same circular polarisation to maximize the transmission of the EIT windows (see section 1.2.3).

2.3.3 Memory optimization

The previous optimizations were required before going to this final stage. They enabled to find the optimal orientation and power for the cooling beams to maximize the optical depth, the optimal alignment and polarization for the control beam to maximize the signal transmission through the cloud. All these parameters are not going to be modified during this last optimization which consists in choosing the signal temporal width, the control intensity, and the cut-off time of the control pulse triggering the storage process.

The signal power is not the same than the one used for the OD and EIT measurements: the average photon number per pulse is set to a few photons (less than ten). The setup employed for this measurement is a bit different than the one described on figure 2.11 due to a few changes: the photodiode PD_{ref} is removed, the multimode fiber is replaced by a single-mode fiber and the output photodiode PD_{out} is replaced by an APD (AQRH 14-FC, Excelitas) and a Fabry-Perot cavity (FPE001A, Quantaser) to filter out the control noise.

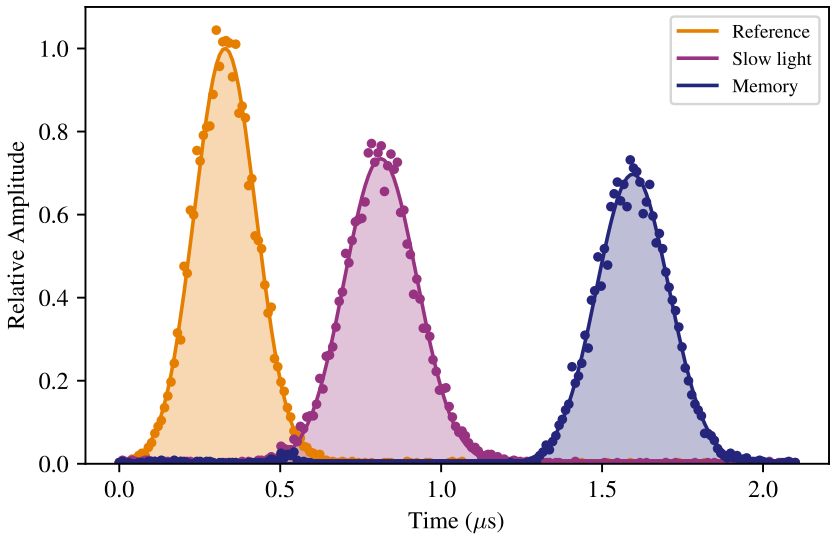

FIGURE 2.15: **Memory measurement.** The reference pulse is the signal before interacting with atoms. The slow-light pulse corresponds to the signal after being propagated through the cloud with an EIT window opened along all its propagation. The memory pulse represents the signal after the storage-and-retrieval process. The efficiency obtained for the slow light is $\eta_{\text{sl}} = (87 \pm 2)\%$ and the one for the memory is $\eta_{\text{mem}} = (81 \pm 2)\%$. The slow-light delay is equal to $\tau_{\text{delay}} = 480\,\text{ns}$ and the FWHM of the reference pulse is $\Delta t_{\text{pulse}} = 230\,\text{ns}$ ($\tau_{\text{delay}} \approx 2\Delta t_{\text{pulse}}$).

The EIT window has a Gaussian waveform in the frequency domain and also in the time domain (the Fourier transform of a Gaussian function is also a gausian function). Therefore, the temporal waveform chosen for the signal pulse is Gaussian in order to perfectly fit inside the transparency window. The FWHM (full width half maximum) of the signal pulse before interacting with atoms is about $\Delta t_{\text{pulse}} = 230\,\text{ns}$ (see the reference pulse on figure 2.15). The slow-light pulse corresponds to the signal after being propagated through the cloud with an EIT window opened along all its propagation. The control beam was turned on before the arrival of the signal pulse on the atoms and turned off after the exit of this pulse from the atomic medium. The slow-light has a delay $\tau_{\text{delay}} = 480\,\text{ns}$ compared to the reference light because of the high group refractive index n_g of the medium in the EIT configuration. The memory pulse represents the signal after the storage-and-retrieval process. The control beam was turned on before the arrival of the signal pulse on the atoms and turned off when the pulse is entirely compressed into the cloud (the compression factor is equal to n_g). After a defined storage time, the control beam is turned on again to retrieve the initial signal pulse. For this example the storage time is about 1.3μs.

Two constraints have to be satisfied in order to optimize the memory efficiency. The first one is $\Delta\nu_{\text{EIT}} > 1/\Delta t_{\text{pulse}}$: the width of the signal in the frequency domain has to be smaller than the width of the EIT window. If this condition is not satisfied,

a fraction of the pulse will be absorbed in the excited state which lowers the transfer efficiency from $|g\rangle$ to $|s\rangle$. The second one is: the spatial length of the signal pulse inside the cloud ($l_{\text{pulse}} = c/n_g \cdot \Delta t_{\text{pulse}}$) must be smaller than the spatial length of the cloud L_{cloud}. If this condition is not satisfied, a fraction of the pulse will leave the atomic medium and the storage efficiency is going to drop due to this leakage. This condition can be reformulated as $\tau_{\text{delay}} > \Delta t_{\text{pulse}}$: the slow-light delay has to be larger than the temporal width of the signal pulse. As a result, the control intensity should be high enough to complete the first constraint ($\Delta\nu_{\text{EIT}}$ increases with the control intensity). However the delay τ_{delay} is decreasing with the control intensity. Therefore, there is a trade-off on the control intensity to satisfy both conditions. Experimentally, the control power is fixed to have $\tau_{\text{delay}} \approx 2\Delta t_{\text{pulse}}$ as it is represented on figure 2.15 ($\tau_{\text{delay}} = 480\,\text{ns}$ and $\Delta t_{\text{pulse}} = 230\,\text{ns}$). The last optimization parameter is the cut-off time t_{cut} defined as the time when the control pulse is turned off to map the signal pulse into a collective excitation of the cloud. If t_{cut} is too small, the end of the signal pulse is absorbed in the excited state (and lost due to spontaneous emission) and if t_{cut} is too long, the first part of the pulse is going to leak outside of the cloud. Then, a compromise on t_{cut} has to be made to optimize the memory efficiency.

One can note on figure 2.15 the efficiency obtained for the slow light $\eta_{\text{sl}} = (87 \pm 2)\%$ and for the memory $\eta_{\text{mem}} = (81 \pm 2)\%$. In general, $\eta_{\text{sl}} \geq \eta_{\text{mem}}$ as the slow-light efficiency is included in the storage-and-retrieval efficiency.

2.4 Optimizing the memory lifetime

The memory efficiency is not the only important parameter to optimize. The lifetime τ of a quantum memory can be defined as the storage time for which the memory efficiency dropped at $1/e \approx 37\%$ of its initial value. In a quantum network, the lifetime of the quantum memories should at least be equal to the propagation time of light along the entire communication line. Therefore, τ should be on the order of ten milliseconds to perform quantum communication between nodes separated by a thousand kilometers. The long-term goal would be to build a memory with such a lifetime and near unity efficiency.

This section shows the experimental setup and methods used to optimize our memory lifetime. During the memory phase, the B-field is turned off but a residual B-field is persistent due to long-lived Eddy currents, in addition to the earth's magnetic field. This residual magnetic field is a decoherence mechanism which is limiting τ in our experiment (see section 1.2.4). The solution is to generate an additional magnetic field opposite to the first one in order to cancel it. The additional field is created by three pairs of compensation coils[3] located around the vacuum chamber.

[3]These compensation coils are different from the ones dedicated to the generation of the magneto-optical trap.

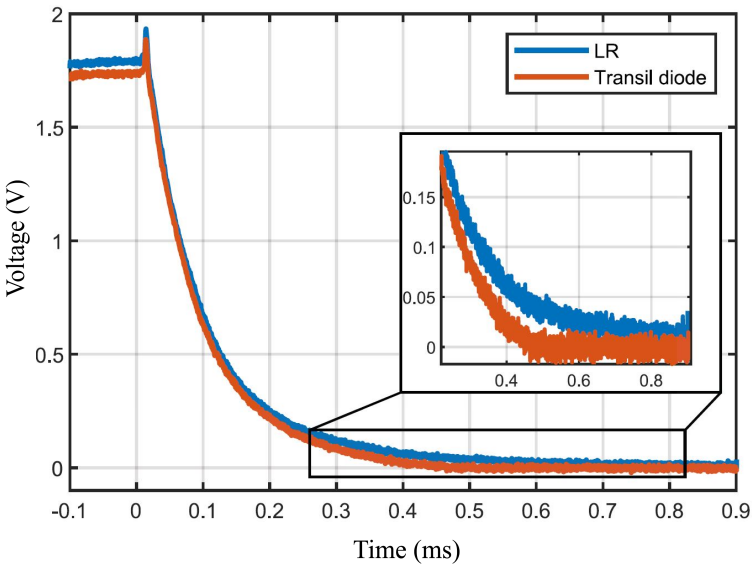

FIGURE 2.16: **Magnetic-field extinction using an electronic switch.** The current circulating in the MOT coils is measured over time via the output voltage of a current clamp. A custom electronic switch stops this current by dissipating the electrical power thanks to a resistor connected in parallel to the coils (blue curve). The performance of the switch is enhanced by implementing a TVS diode (orange curve). This diode cuts off the current to zero within 450 μs (see the inset).

2.4.1 Fast electronic switch for the extinction of the MOT coils

The first step in order to avoid any residual magnetic field during the storage is to completely stop the current in the MOT coils. For this purpose, a custom electronic switch dissipates the electrical power thanks to a resistor connected in parallel to the coils. We measured the current evolution over time in figure 2.16 with a current clamp. The voltage at the output of the clamp is proportional to the current circulating inside the coils. The fall time[4] is proportional the ratio between the inductance of the coils and resistance value, and is equal to 260 μs in our experiment. We enhanced the performance of the switch by implementing a TVS diode[5] (BZW-50). This diode cuts off the current to zero within 450 μs (see the inset in figure 2.16).

2.4.2 Current drivers for the compensation coils

A fast extinction of the MOT coils is necessary but not sufficient to cancel the residual magnetic field during the memory process because of long-lived Eddy currents. As a result, we need to actively compensate this residual B-field by injecting current in the compensation coils. During my PhD, we implemented new current drivers for the compensation coils in order to improve the accuracy and the control of the

[4]The fall time is the time taken by a pulse to decrease its amplitude from usually 90 % to 10 % of its peak value.

[5]TVS diode: transient-voltage-suppression diode

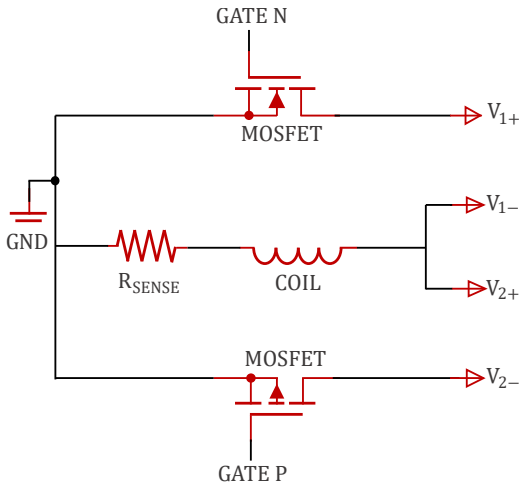

FIGURE 2.17: **Current drivers for the compensation coils in a bipolar configuration.** A PID controller changes the voltage applied to the MOSFET's gate to match the voltage around R_{sense} with the targeted voltage. The electronic circuit of the PID controller is shown in the Appendix A. Two MOSFETs are employed to enable positive and negative values and the power supply is floated instead of grounded.

magnetic field cancellation. The electronic circuit of the current drivers is presented on figure 2.17 and was inspired by the following PhD thesis [Vendeiro, 2021].

The operation principle of this electronic circuit is the following: a PID controller senses the current by measuring the voltage around R_{sense} and calculates the difference between this value and the target value. The PID controller thus changes the voltage applied to the MOSFET's gate to match the voltage around R_{sense} with the targeted voltage. Two MOSFETs are employed to enable a bipolar drive of the current (for positive and negative values). The power supply is floating instead of grounded. Indeed in the grounded configuration ($V_{1-} = V_{2+} = \text{GND}$), the maximum voltage applied by the PID controller on the MOSFET's gate is smaller than the one provided by the power supply which leads to a limitation on the current going through the coils. This issue can be overcome with a floating power supply as shown on figure 2.17. The electronic circuit of the PID controller is shown on the Appendix A and was designed in collaboration with the electrical workshop of our laboratory.

Three current drivers are used for the three pairs of compensation coils located along the axes X, Y, Z (the axes are the ones represented on figure 2.13). The pairs of coils are in a Helmholtz configuration. In our implementation $R_{\text{sense}} = 1\,\Omega$, the inductance and the resistance of the six compensation coils (two per axis) are shown on the table 2.2:

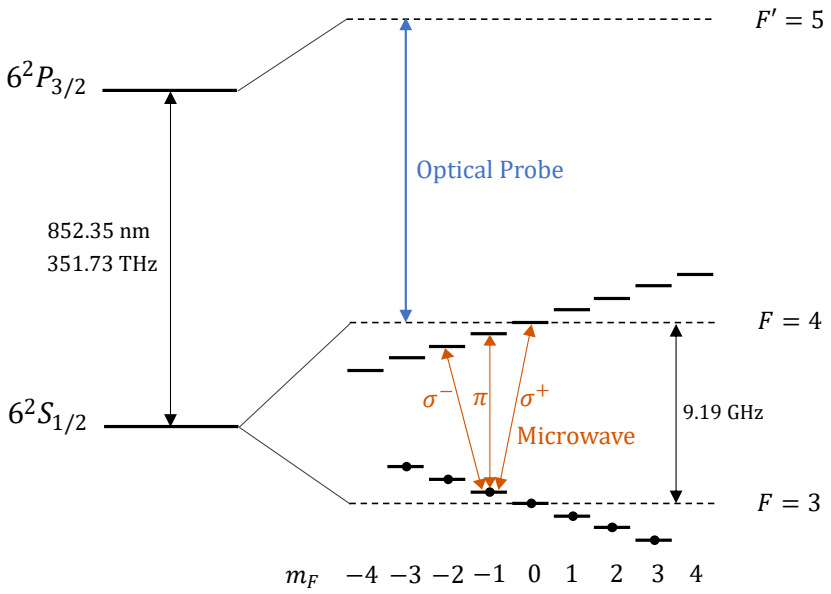

FIGURE 2.18: **Microwave spectroscopy mechanism.** The microwave frequency is scanned around the resonance to excite the atoms in the level $|6S_{1/2}, F = 4\rangle$ with three different transitions: $m_F \rightarrow m_{F'} = \{m_F - 1, m_F, m_F + 1\}$ corresponding to the three polarizations σ^-, π, σ^+. After reaching $F = 4$, the atoms are going to absorb the optical probe locked on the transition $|6S_{1/2}, F = 3\rangle \rightarrow |6P_{3/2}, F' = 5\rangle$. This absorption is monitored to perform spectroscopy.

Position	X_1	X_2	Y_1	Y_2	Z_1	Z_2
L	1.6 mH	1.6 mH	2.0 mH	2.4 mH	2.1 mH	2.2 mH
R	1.5 Ω	1.5 Ω	2.1 Ω	2.2 Ω	2.2 Ω	2.2 Ω

TABLE 2.2: Measurements of the resistance R and the inductance L for the six compensation coils.

The measurements of the coil inductance were done with the same method than the ones for the MOT coils described on the section 2.1.2.

2.4.3 Microwave spectroscopy

The first task to complete in order to compensate the residual magnetic field is to measure it. The sensing method employed is called microwave spectroscopy. The principle is described in figure 2.18. The atoms are initially in the level $|6S_{1/2}, F = 3\rangle$. A microwave signal is generated (SMB100A, R&S) with a 30 dBm amplitude and is sent on the atomic cloud thanks to an antenna. This microwave is addressing the transition $|6S_{1/2}, F = 3\rangle \rightarrow |6S_{1/2}, F = 4\rangle$. Its frequency is scanned with a MHz range around the resonance. The Zeeman levels m_F are split due to the residual magnetic field (Zeeman effect). During the scan, the microwave is going to excite the atoms to the state $|6S_{1/2}, F = 4\rangle$ with three different types of transitions (selections rules): $m_F \rightarrow m_{F'} = m_F$ for the polarization π, $m_F \rightarrow m_{F'} = m_F - 1$ for the polarization σ^- and $m_F \rightarrow m_{F'} = m_F + 1$ for the polarization σ^+. After reaching

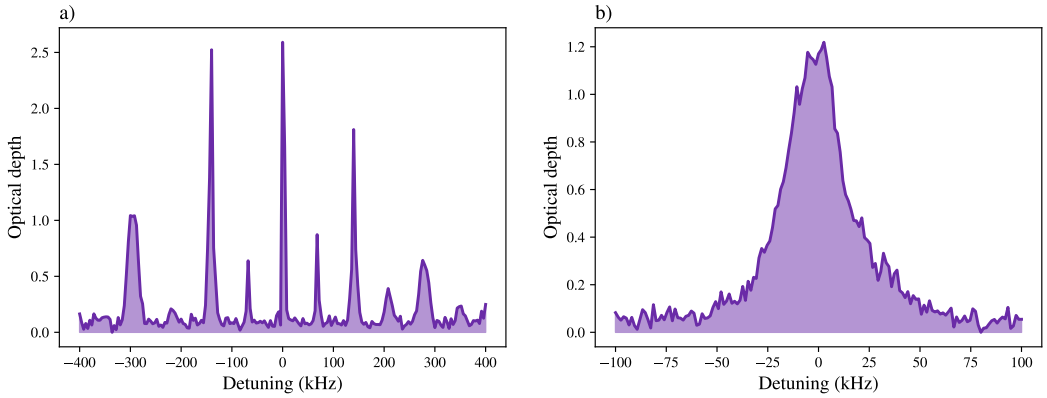

FIGURE 2.19: **Microwave spectroscopy measurements.** The graphs represent the optical depth on the probe transition as a function of the microwave detuning. *a)* Microwave spectroscopy without cancellation of the residual magnetic field. The peaks at the detunings $\delta = \{-280, -140, 0, 140, 280\}$ kHz correspond to the transitions $m_F \rightarrow m_{F'} = m_F$ for $m_F = \{-2, -1, 0, 1, 2\}$. The peaks at the detunings $\delta = \{-350, -210, -70, 70, 210, 350\}$ kHz correspond to the transitions $m_F \rightarrow m_{F'} = m_F + 1$ and also $m_F + 1 \rightarrow m_{F'} = m_F$ for $m_F = \{-3, -2, -1, 0, 1, 2\}$. *b)* Microwave spectroscopy with cancellation of the residual magnetic field. The width of this peak is the average inhomogeneous broadening of the transitions $m_F \rightarrow m_{F'} = \{m_F - 1, m_F, m_F + 1\}$ on all the m_F values. Its FWHM is equal to 35 kHz and corresponds to a residual magnetic field gradient on the order of 10 mG/cm.

$F = 4$, the atoms are going to absorb the photons from the optical probe locked on the transition $|6S_{1/2}, F = 3\rangle \rightarrow |6P_{3/2}, F' = 5\rangle$. The probe frequency is fixed unlike the microwave signal. We are monitoring the absorption of the probe beam in order to perform the spectroscopy presented on figure 2.19. The graphs represent the optical depth on the probe transition as a function of the microwave detuning. These measurements are done in the pulsed regime: the microwave pulse is first sent with a temporal length equal to 150 μs followed by a 30 μs probe pulse.

The multiple peaks on figure 2.19(a) represent the transitions $m_F \rightarrow m_{F'} = \{m_F - 1, m_F, m_F + 1\}$ for different values of m_F. The peaks at detunings $\delta = \{-280, -140, 0, 140, 280\}$ kHz correspond to the transitions $m_F \rightarrow m_{F'} = m_F$ for $m_F = \{-2, -1, 0, 1, 2\}$[6]. The peaks at detunings $\delta = \{-350, -210, -70, 70, 210, 350\}$ kHz correspond to the transitions $m_F \rightarrow m_{F'} = m_F + 1$ and also $m_F + 1 \rightarrow m_{F'} = m_F$ for $m_F = \{-3, -2, -1, 0, 1, 2\}$. In a general way, if we consider Δ_B the Zeeman splitting between adjacent Zeeman levels, $\delta = 2k\Delta_B$ counts for the π transitions (k is an integer), and $\delta = (2k + 1)\Delta_B$ counts for the $\{\sigma^+, \sigma^-\}$ transitions. Therefore we can deduce from this measurement the residual magnetic field without cancellation: $\Delta_B = \mu_B g_F B_{\text{res}} = 70$ kHz, with μ_B the Bohr magneton and g_F the Landé g-factor of the hyperfine level F. Its leads to $B_{\text{res}} = 200$ mG. This value represents the homogeneous part

[6]The peaks corresponding to the transitions $m_F \rightarrow m_{F'} = m_F$ for $m_F = \{-3, 3\}$ are beyond the scanning range at ± 420 kHz

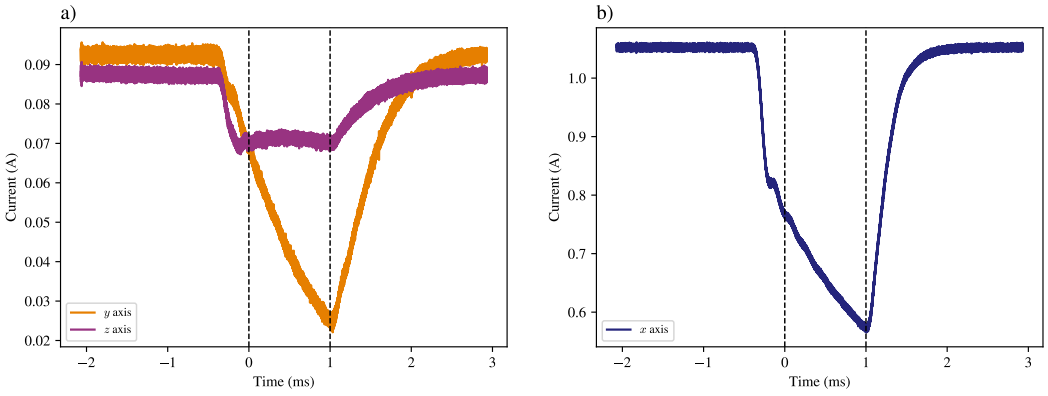

FIGURE 2.20: **Current applied for the dynamic cancellation of the residual B-field.** The cancellation is done between $t = 0\,\text{ms}$ and $t = 1\,\text{ms}$ when the storage-and-retrieval process occurs. The time $t = 0\,\text{ms}$ corresponds to 2 ms after the extinction of the MOT coils. *a*) Current applied for magnetic field cancellation by the pairs of coils oriented along the z-axis (longitudinal direction of the cloud) and y-axis. *b*) Current applied for magnetic field cancellation by the pair of coils oriented along the x-axis (gravity direction).

of the residual B-field (constant over space). The compensation coils in Helmholtz configuration can cancel this homogeneous contribution as it shown on figure 2.19(b). All the peaks unite into one after cancellation. However this peak has a width larger than the natural linewidth of the transition $|6S_{1/2}, F = 3\rangle \rightarrow |6S_{1/2}, F = 4\rangle$ due to the inhomogeneous part of the residual B-field[7]. The contribution from this part is quite important for our atomic cloud due to its elongated shape (2.5 cm long). The width of this peak is the average inhomogeneous broadening of the transitions $m_F \rightarrow m_{F'} = \{m_F - 1, m_F, m_F + 1\}$ on all the m_F values. Its FWHM (full width half maximum) after compensation is equal to 35 kHz[8]. Assuming that the population is equally distributed in all the m_F levels, it corresponds to a residual magnetic field gradient on the order of 10 mG/cm.

Six months before I joined the group, my co-workers noticed that the residual magnetic field was not constant over time (this issue was not present in our previous implementation before 2020). For example, if this one is cancelled at a fixed time t_0 in the sequence, it is not the case anymore at $t_0 + 100\,\mu\text{s}$: the width of the peak measured by the microwave spectroscopy increases from 35 to 100 kHz. To mitigate this issue, the current in the compensation coils has to vary over time to compensate for this time-dependent B-field. The current injected into the three pairs of coils is displayed on figure 2.20. The axis refers to the orientation of the pair of coils used: z corresponds to the pair along the longitudinal axis of the cloud and x is the one along

[7]The residual B-field can be written as $\vec{B}_{\text{res}} = \vec{B}_0 + \vec{B}_1 z$ with z the position of the particle considered along the elongated axis of the cloud. $\vec{B}_0$ is the homogeneous component and $\vec{B}_1$ is the inhomogeneous part of this residual field.

[8]One solution to decrease the width of the peak would be to generate magnetic-field gradients to cancel the inhomogeneous part of the residual field.

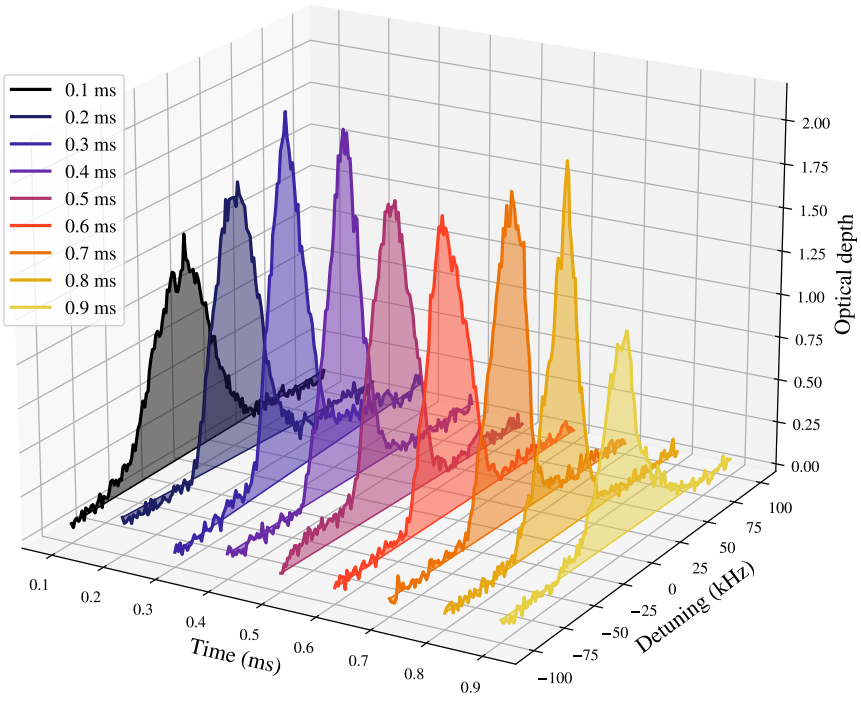

FIGURE 2.21: **Dynamical cancellation of the magnetic field.** The 3D plot represents the optical depth on the probe transition as a function of the microwave detuning and time (the origin of time corresponds to 2 ms after the extinction of the MOT coils).The average FWHM of the peaks over the 1 ms interval is equal to 36 kHz.

the gravity direction. As a reminder, the direction of the magnetic field created in the Helmoltz configuration at the center of the chamber is the same than the orientation of the pair (the pair along x-axis creates a B-field also oriented on the x-axis). The time $t = 0$ ms corresponds to 2 ms after the extinction of the MOT coils at the end of the compression phase (see figure 2.5). The cancellation is done between $t = 0$ ms and $t = 1$ ms when the storage-and-retrieval process occurs. As said earlier, the two contributions of this residual field are: the earth's magnetic field (DC component) which is mainly oriented in the gravity direction as the high values of current on the x-axis indicate, but also the magnetic field induced by the extinction of the main coils (AC component). The latter is the reason why we need to implement dynamical cancellation. The figure 2.20 shows that this AC component is mainly oriented on the transverse direction of the cloud (x and y axis) as the compensation current is almost constant $t = 0$ ms and $t = 1$ ms on the longitudinal direction (z-axis).

The microwave spectroscopy has been used in order to obtain the values for these current ramps. The results of the dynamical cancellation is presented on figure 2.21. This 3D plot represents the microwave spectroscopy at different times within the

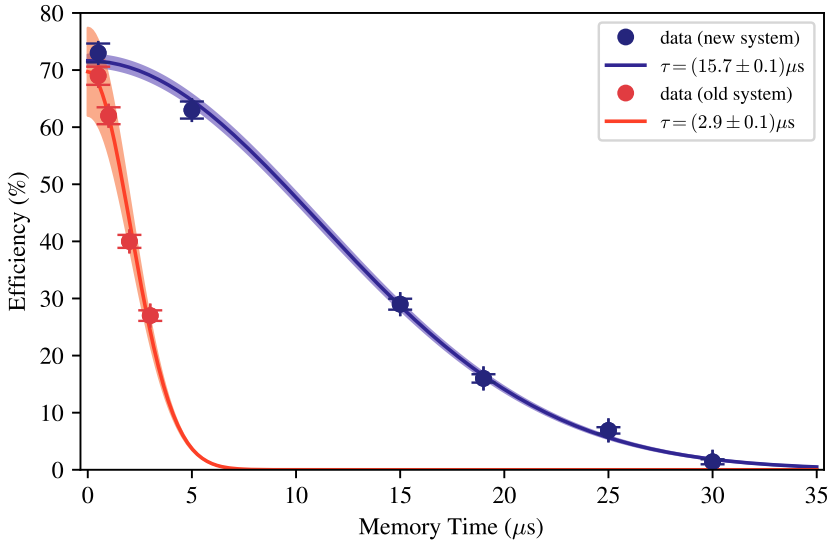

FIGURE 2.22: **Improvement of the memory lifetime.** The dots represent the experimental data and the solid lines are the fit curves corresponding to the function Ae^{-t^2/τ^2}. The lifetime achieved by the new compensation system $\tau = (15.7 \pm 0.1)\,\mu$s is five times better than the old one $\tau = (2.9 \pm 0.1)\,\mu$s.

sequence by steps of 0.1 ms (the origin of time corresponds to 2 ms after the extinction of the MOT coils). The average FWHM of the peaks over the 1 ms interval is equal to 36 kHz. The hardest point for the compensation is the beginning of the sequence as the black curves indicates (FWHM=50 kHz). Indeed, it is the closest time from the extinction which could explain why the inhomogeneous broadening is the highest compared to the other times.

2.4.4 Memory lifetime improvement

We now turn to evaluate the impact of this cancellation on the lifetime of the memory. The first chapter underlines other decoherence mechanisms such as the motional dephasing. However, the decoherence source which is currently limiting the memory lifetime in our experiment is the residual B-field. Therefore, any improvement on the compensation of the residual field enhances the lifetime.

Before 2020, the system was compensated with DC currents as the residual field was not evolving with time at 2 ms after the extinction of the MOT coils. A 15 μs lifetime was achieved with this system [Vernaz-Gris, 2018]. However, as said earlier, an AC component appeared since 2020, leading to the dynamical cancellation presented in the previous section. The first current drivers used to cancel this time-dependent residual magnetic field were made of old electronic circuits from the group. The lifetime obtained with these old current drivers is evaluated in figure 2.22 and compared to the one achieved with the new current drivers presented in section 2.4.2. The dots

represent the experimental data and the solid lines are the fit curves corresponding to the function Ae^{-t^2/τ^2}. The lifetime achieved by the new compensation system $\tau = (15.7 \pm 0.1)\,\mu$s is five times better than the old one $\tau = (2.9 \pm 0.1)\,\mu$s. The main difference between the old and the new system that could explain this improvement are the current drivers: they are more accurate compared to the previous ones thanks to their PID controllers. Moreover, the usability of the compensation system has been upgraded. In fact, the input signal of the old current drivers was produced by a function generator. Each point of the ramp had to be edited one after the other. Once the ramp was implemented in the device, modifications on some particular points were time consuming as the access was limited. Instead of this function generator, we implemented a DAQ (USB-6363, National Instruments) controlled by a Python script. The current ramps are represented by arrays inside the script, which can be easily modified as we have an instant access on each point of the ramps.

On the first chapter (see section 1.2.4), we derived an expression that links the evolution of the memory efficiency over time with the residual magnetic field gradient:

$$\eta(t) = A \left| \sum_{m_g=-F}^{F} n(m_g) d(m_g) e^{-t^2/\tau_{m_g}^2} \right|^2 \tag{2.6}$$

with A the initial efficiency, $n(m_g)$ the probability to have an atom in the Zeeman level m_g at $t = 0$ and $d(m_g)$ the strengths of the transitions used for the storage-and-retrieval process. τ_{m_g} is the lifetime for an atom populating the ground state m_g and is defined as $1/\tau_{m_g} = m_g \mu_B g_F \frac{dB}{dz} L/(2\hbar)$. We can deduce the residual magnetic field gradient $\frac{dB}{dz}$ by fitting this theoretical model with the experimental data. Assuming that all the m_g levels are initially equally distributed, it leads to $\frac{dB}{dz} = 11\,\mathrm{mG/cm}$. This value is in good agreement with the one calculated from the width of the microwave spectroscopy profile.

This lifetime value is not a strict limitation of our cold atoms platform as it can be increased by multiple means. One can overcome the decoherence mechanism due to the residual B-field by applying a Zeeman pumping into a specific m_F level combined with magnetically insensitive clock transition [Bao et al., 2012; Xu et al., 2013]. Moreover, implementing a tightly confining optical lattice reduces motional dephasing [Zhao et al., 2009] but also creates differential light shift which results in lifetime on the order of the millisecond. This differential light shift can be cancelled with a "magic" magnetic field increasing the lifetime to the 100 ms range [Jenkins et al., 2012].

2.5 Additional details on the experimental setup

This section presents the additional details on the setup playing a key role in our experiment.

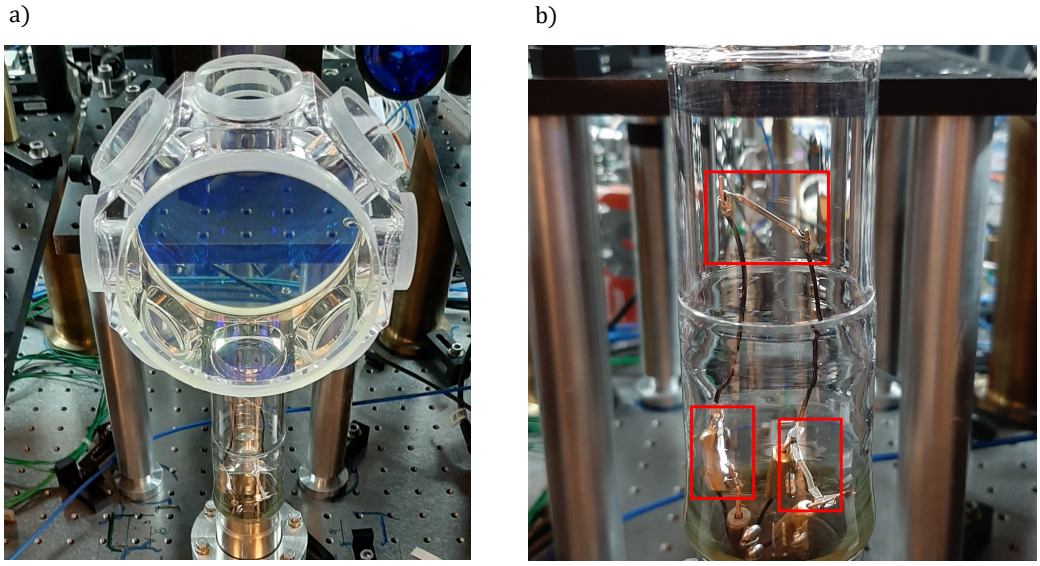

FIGURE 2.23: **Glass chamber and dispensers.** *a*) The vacuum chamber is made of glass to reduce Eddy currents. An anti-reflection coating is on the inside and outside surface of the chamber optimized for the two wavelengths: 852 nm and 1064 nm. *b*) The dispensers are located at the bottom of the glass chamber. We placed three alkali metal dispensers for Cesium (each one is highlighted with red borders and is connected to two electrodes).

2.5.1 Vacuum system

The first element we need to build a cold atom experiment is the vacuum system in order to remove all the molecules contained in the air (mostly N2 and O2) to only keep the cesium atoms inside the chamber. Reaching low-pressure is one requirement to implement a MOT: if the pressure is too high ($> 10^{-8}$ Torr), atoms are going to be ejected from the trap faster than they can be loaded. Furthermore, it prevents collisions between the cesium atoms which is one limiting factor of the coherence time for hot vapor [Horsley et al., 2013]. Most of the cold atom experiments are using metallic chambers which is a drawback in the case of our quantum memory. Indeed, when the MOT coils are turned off, Eddy currents could propagate on the chamber and reduce our memory lifetime. Therefore, our vacuum chamber is made of glass to avoid this effect (see figure 2.23(a)). An anti-reflection coating is on the inside and outside surface of the chamber optimized for the two wavelengths: 852 nm which is the wavelength of the cooling beams and 1064 nm in the prospect of a dipole trap in the future. The D1 line (894 nm) is not the optimal wavelength for the coating but its transmission remains fairly good (97%).

The source of cesium atoms is located at the bottom of the vacuum chamber (see figure 2.23(b)). This source called dispenser or getter is a metal wire which is connected to electrodes. These electrodes are coupled to a power supply injecting current through the metal wire. Then, the dispenser heats up due to the current flow and releases a cesium gas. The atom flux dispensed inside the chamber is increasing with

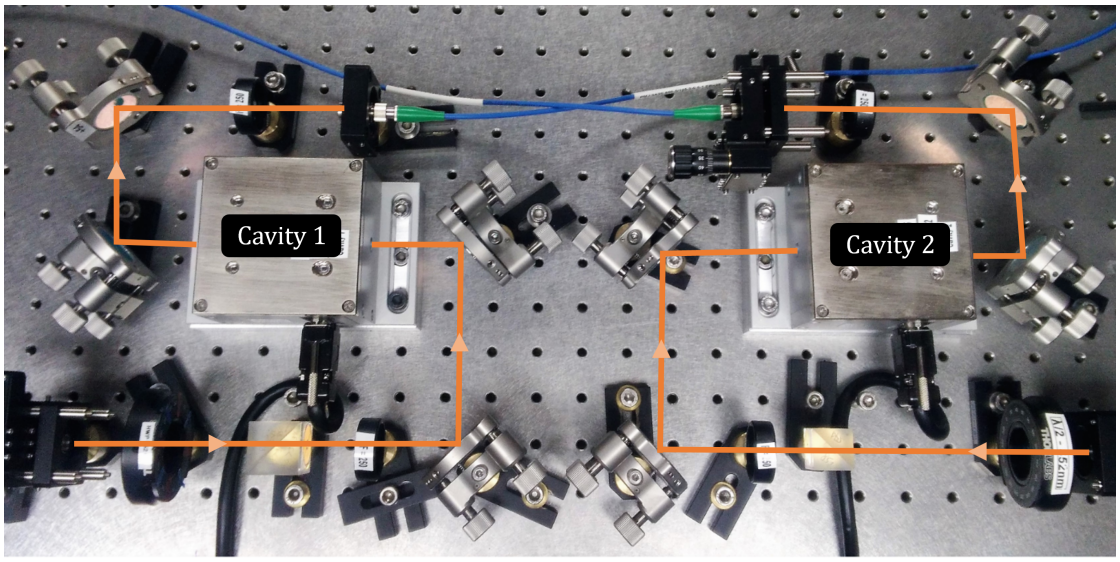

FIGURE 2.24: **Filtering setup.** The light coming from the memory is decomposed in two paths with orthogonal polarizations: one cavity is implemented for each polarizations to filter out the control light with a 45 dB rejection. Convex lenses are used to focus the light inside the cavity etalons with a focal length $f' = 25\,\text{cm}$.

the current injected in the electrodes. During my doctoral research, we had to change the dispensers as they were five years old and we had evidence that they were running empty. It was necessary to "break the vacuum" as the chamber needed to be opened to have access to the getters. Nitrogen was circulating inside the chamber during this phase to avoid water and dust from sticking on its inner walls. We placed three alkali metal dispensers for Cesium (SAES) at the positions given by figure 2.23(b). One getter is above the other to optimize the atom flux feeding the MOT (this is the one currently used in the experiment). After setting the dispensers, the system is closed and a turbo pump (Pfeiffer Vacuum HiCube 80 Eco) decreases the pressure to $5 \cdot 10^{-7}$ Torr. When the pressure reaches this point, the procedure to activate the getters begins:

- Note of the initial pressure ($\approx 5 \cdot 10^{-7}$ Torr on the turbo pump).
- Increment the dispenser current by 0.2 A and allow time for the pressure to return to its initial level.
- Perform the second step until the pressure ceases to decrease, indicating a consistent release of atoms from the dispensers.

The current value reached after this final step is around 5 A for the three dispensers. However, after activation, we turned off two out of three getters and decreased the current to 3.8 A for the one currently used in the experiment. Finally, the ion pump (Starcell Vacion Plus 40 L/s) is turned on to reduce the pressure to 10^{-10} Torr.

2.5.2 Detection setup

The last part of our experimental implementation is the detection setup which enables the measurement of the signal pulses with and without storage. The first elements of this setup are the filtering cavities (FPE001A, Quantaser) used to filter out the control beam. These Fabry-Perot cavities have a FSL (free spectral range) about 16 GHz and a 60 MHz bandwidth. The peak transmission is around 70 % with a 45 dB rejection at the control frequency, i.e. at 9.2 GHz around the central frequency. The central frequency can be modified via temperature controllers with an accuracy on the order of 1 mK (2 MHz resolution). The filtering setup is presented on figure 2.24. The light coming from the memory is decomposed in two paths with orthogonal polarizations: one cavity is implemented for each polarization. Convex lenses are used to focus the light inside the cavity etalons with a focal length $f' = 25$ cm. The stability over time of the cavities transmission has been improved with a plexiglas box which surrounds them by suppressing the disturbances caused by air flows. The light coming out of the filtering cavities is coupled into fibers linked to single photon counters (AQRH 14-FC, Excelitas). These avalanche photodiodes have typically a 50 % detection efficiency at 852 nm and a 50 Hz dark count rate.

2.6 Conclusion

This chapter showed the extent of our experimental implementation for the atom cooling and the memory process. On the cooling side, changing the main coils enabled to reach higher B-field gradient due to the increase of wire turns compared to the previous version. On the memory side, improvements have been done on the signal lock to avoid any frequency modulation on the light sent to the experiment. We analysed the key ingredients to optimize the memory efficiency of our storage platform. Indeed, choosing the D1 Cesium line, reaching a high optical depth and an EIT peak transmission around unity are crucial elements to build a highly efficient quantum memory. The accuracy and the control of our compensation system were improved, leading to a memory lifetime up to 15 μs (we returned to the value achieved in the group before the issue of the time-dependent residual magnetic field). Our cold-atomic ensemble has the required properties to be implemented as a memory layer in a quantum cryptographic protocol.

CHAPTER 3

CRYPTOGRAPHIC PROTOCOL USING A COLD-ATOM BASED QUANTUM MEMORY

Contents

Quantum memories play a key role in long-distance quantum communications as they are employed to synchronize elementary links between each others [Kimble, 2008]. This synchronization device can be used for other purposes such as in linear optical quantum computation in order to increase the success rate of non-deterministic operations [Heshami et al., 2016] but also in quantum cryptographic protocols. Indeed, few experimental implementations of cryptographic protocols combined with quantum memories were reported [Namazi et al., 2017b]. However, none of them include the possibility that malicious parties having access to the memory could exploit losses and noise added by the storage platform to hide their cheating attempts. Therefore, the protocol is considerably more challenging to perform in the secure regime

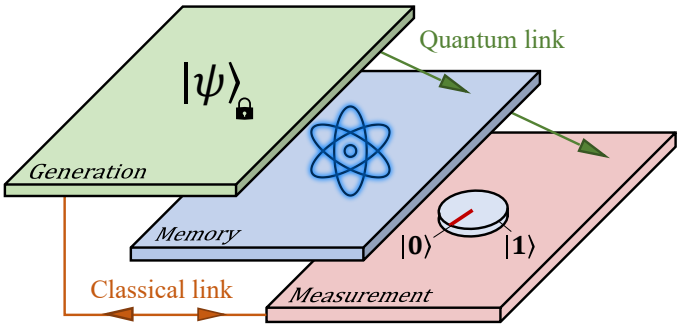

FIGURE 3.1: **Quantum memory implemented as an intermediate layer in a quantum cryptographic protocol.** In the context of quantum networks, optical memories are required to exchange quantum information on demand. However, their use also imposes further challenges for ensuring secure communications, in terms of losses and noise added by the storage platform.

when this possibility is taken into account as the constraints are very demanding in terms of memory efficiency and fidelity.

One fundamental property of quantum mechanics is the no-cloning theorem [Wootters and Zurek, 1982]: one cannot create a identical copy of an unknown quantum state. Building upon this idea, Wiesner designed the quantum money protocol in [Wiesner, 1983], demonstrating that by encoding a secret key into qubits defined in conjugate bases, we can safeguard it against forgery. These qubits are stored in a quantum memory used as an intermediate layer in the cryptographic protocol (see figure 3.1). Experimental implementations of the quantum money protocol without this memory layer were published [Bozzio et al., 2018; Guan et al., 2018]. However the complete version of the protocol has not yet been reported due to the lack of high-efficiency and low-noise storage devices [Bozzio et al., 2019]. A few quantum money use-cases are not relying on quantum storage [Schiansky et al., 2023], but their approach involves deploying a trusted network whose spacetime coordinates are strictly monitored [Kent and Pitalúa-García, 2020]. This option is challenging to implement, as it requires either stringent clock synchronization between remote agents or trusting a Global Positioning System (GPS), potentially vulnerable to spoofing-type attacks [Tippenhauer et al., 2011]. In this work, we take advantage of our efficient cold-atom-based quantum memory [Cao et al., 2020] to reach the secure regime of the quantum money protocol for its first demonstration involving a storage device.

3.1 Quantum money

The purpose of this section is to explain the quantum money protocol and provide the security analysis of the protocol in the presence of noise and storage losses. The security analysis was developed by Mathieu Bozzio [Bozzio, 2019] who is co-author of the paper we are writing about the implementation of the quantum money protocol with our cold-atom based quantum memory.

3.1.1 The protocol

We consider a three-party quantum money scheme involving a bank, a client and a vendor. The protocol consists of four steps described in figure 3.2(a). First, the bank encodes a random secret classical key onto a sequence of two-level quantum states (qubits). The secret key dictates each qubit's encoding basis, along with its chosen eigenstate. In our case, the qubits are mapped onto the polarization of weak coherent states and the encoding bases are either $\{H, V\}$ or $\{\sigma^+, \sigma^-\}$. Secondly, the states are stored in the quantum memory, materializing the quantum credit card held by the client. In a third step, the client retrieves the coherent states from the memory and forwards them to a vendor, who measures each qubit in a random polarization basis. In the final verification step, the vendor communicates the measurement basis and the results to the bank, who checks for consistency with the original secret key and determines the error rate ε (fraction of errors in the communication). The verification is only done on qubits measured in the right basis, i.e. when the measurement basis is the same than the encoding one. The other qubits are not taken into account in the analysis.

The untrusted party in this scheme is the client[1] who may attempt to duplicate the sequence of qubits in order to perform two transactions at the same time (double-spending attempt). This operation cannot be performed without introducing errors in the process due to the no-cloning theorem. Therefore, we need to set a security threshold to prevent attacks from malicious clients.

3.1.2 Security analysis

In an ideal experiment, measuring a non-zero error rate upon verification would immediately signal an unauthorized double-spending attempt to the honest parties. In the presence of photonic noise and storage losses however, even honest parties will introduce a non-zero error rate. This implies that some fraction of experimental imperfection should be tolerated for a practical protocol to succeed. On the other hand, a malicious party having access to perfect quantum channels may exploit this fault tolerance to hide their double-spending attempts. This calls for a rigorous security analysis, identifying a combination of noise, losses and mean photon number for which no malicious party is able to successfully cheat. We provide such an analysis by searching for the optimal quantum cloning strategy that minimizes the introduction of noise upon verification, given a fixed mean photon number and storage losses. This derivation is based on [Bozzio et al., 2019].

3.1.3 Modelling for weak coherent state implementation

In the protocol described above, the information is encoded on the polarizations of weak coherent states. Coherent states are expressed in the basis of Fock states as:

[1] We consider that the bank and the vendor are trusted.

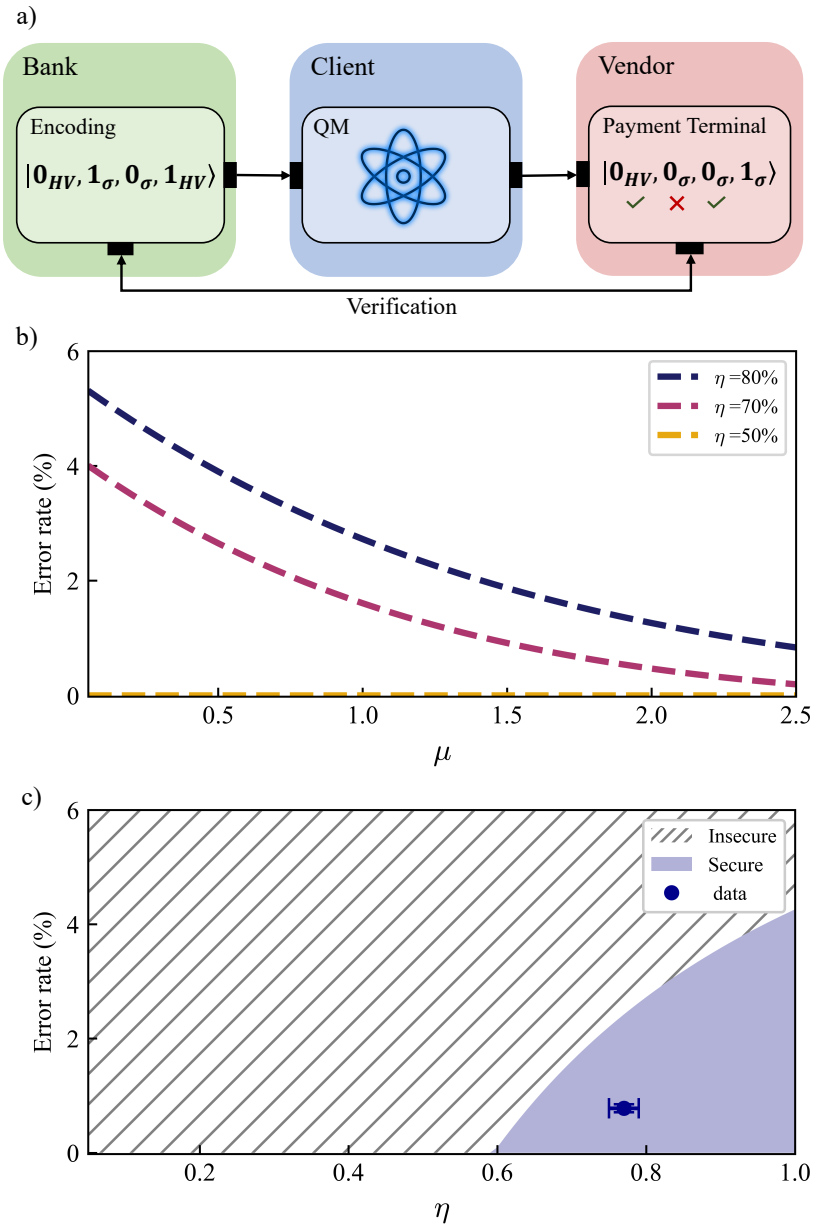

FIGURE 3.2: **The quantum money protocol.** a) The bank encodes a random secret key into a sequence of polarization qubits. The encoding base is either $\{H, V\}$ or $\{\sigma^+, \sigma^-\}$. These qubits are stored in a quantum memory that is accessible to the client. Then, the client retrieves the quantum states from the memory and forwards them to the vendor, who measures each qubit in a random polarization basis. In the final step, the vendor communicates the results to the bank with the measurement basis associated. The bank compares these results with the part of the secret key encoded in the vendor's measurement basis. Finally, the error rate of the communication could be established and compared to a security threshold. b) Security threshold as a function of the mean photon number μ for different memory efficiencies η. The communication is considered as secure if the error rate is below the threshold. c) Security threshold as a function of the memory efficiency for $\mu = 1$. The hatched area represents the insecure regime while the blue one is the secure area. The blue data point is the experimental data achieved after implementation of the protocol including the memory layer.

$$|\alpha\rangle = \sum_{n=0}^{\infty} e^{-\frac{|\alpha|^2}{2}} \frac{\alpha^n}{\sqrt{n!}} |n\rangle = \sum_{n=0}^{\infty} C_\alpha(n) |n\rangle \tag{3.1}$$

with $|n\rangle$ the Fock states. The mean photon number is $\mu = |\alpha|^2$. One can map the polarization qubits $\{|H\rangle, |\sigma^+\rangle, |V\rangle, |\sigma^-\rangle\}$ employed in our experiment onto coherent states:

$$\begin{aligned} |\alpha_H\rangle &= \left|e^{i\theta}\alpha\right\rangle \otimes |0\rangle, \quad |\alpha_{\sigma^+}\rangle = \left|e^{i\theta}\frac{\alpha}{\sqrt{2}}\right\rangle \otimes \left|e^{i(\theta+\pi/2)}\frac{\alpha}{\sqrt{2}}\right\rangle \\ |\alpha_V\rangle &= |0\rangle \otimes \left|e^{i\theta}\alpha\right\rangle, \quad |\alpha_{\sigma^-}\rangle = \left|e^{i\theta}\frac{\alpha}{\sqrt{2}}\right\rangle \otimes \left|e^{i(\theta+3\pi/2)}\frac{\alpha}{\sqrt{2}}\right\rangle \end{aligned} \tag{3.2}$$

with θ a global phase. In the following part, we note $|\alpha_0\rangle = |\alpha_H\rangle$, $|\alpha_1\rangle = |\alpha_{\sigma^+}\rangle$, $|\alpha_2\rangle = |\alpha_V\rangle$ and $|\alpha_3\rangle = |\alpha_{\sigma^-}\rangle$.

We assume that the phase θ from equation (3.2) is uniformly randomized over $[0, 2\pi]$[2]. Under this assumption, the integration of $|e^{i\theta}\alpha\rangle$ over θ reduces the coherent states to a mixture of photon number states [Lo and Preskill, 2005]:

$$\frac{1}{2\pi}\int_0^{2\pi} |\sqrt{\mu}e^{i\theta}\rangle\langle\sqrt{\mu}e^{i\theta}| \, d\theta = e^{-\mu}\sum_{n=0}^{\infty}\frac{\mu^n}{n!}|n\rangle\langle n|. \tag{3.3}$$

When the mixture contains 0 photon, no information can be accessed by the adversary. When it contains 1 photon, the security proof is employed. When it contains 2 or more photons, the adversary cheats without introducing errors as each photon represents one copy of the information encoded.

The phase-randomized states can be decomposed in the basis $\{|0\rangle, |H\rangle, |V\rangle, |m_0\rangle, |m_1\rangle, |m_2\rangle, |m_3\rangle\}$, with $|0\rangle$ the vacuum component, $|H\rangle$ and $|V\rangle$ the polarization states associated to the single photon component ($n = 1$), and $|m_i\rangle$ representing multi-photon states ($n \geqslant 2$) [Bozzio, 2019]. In our study, we consider the polarizations $|H\rangle, |\sigma^+\rangle, |V\rangle$ and $|\sigma^-\rangle$. $|\sigma^+\rangle$ and $|\sigma^-\rangle$ are not part of the basis as they are superpositions of $|H\rangle$ and $|V\rangle$. The density matrices of the phase-randomized states are thus expressed as:

$$\begin{aligned} \rho_0 &= P_\mu(0)\,|0\rangle\langle 0| + P_\mu(1)\,|H\rangle\langle H| + P_\mu(\geqslant 2)\,|m_0\rangle\langle m_0| \\ \rho_1 &= P_\mu(0)\,|0\rangle\langle 0| + P_\mu(1)\,|\sigma^+\rangle\langle\sigma^+| + P_\mu(\geqslant 2)\,|m_1\rangle\langle m_1| \\ \rho_2 &= P_\mu(0)\,|0\rangle\langle 0| + P_\mu(1)\,|V\rangle\langle V| + P_\mu(\geqslant 2)\,|m_2\rangle\langle m_2| \\ \rho_3 &= P_\mu(0)\,|0\rangle\langle 0| + P_\mu(1)\,|\sigma^-\rangle\langle\sigma^-| + P_\mu(\geqslant 2)\,|m_3\rangle\langle m_3| \end{aligned} \tag{3.4}$$

where $P_\mu(n)$ are equal to:

$$P_\mu(0) = e^{-\mu}, \quad P_\mu(1) = \mu e^{-\mu}, \quad P_\mu(\geqslant 2) = 1 - (1+\mu)e^{-\mu}. \tag{3.5}$$

[2]In the experiment, the global phase θ of the coherent states is not fixed and is changing quite importantly due to phase noise added by acousto-optic modulators. Therefore, we made the approximation that the states are phase randomized.

3.1.4 Threshold calculation

After modelling the states accessible to the adversary, the purpose of this section is to analyze the possible attacks performed by this malicious party to duplicate the information encoded. The attack from the dishonest client is represented by the map Λ generating two versions of the initial quantum state created by the bank. This initial state is described by the density matrice:

$$\rho_{\text{ini}} = \frac{1}{4}\sum_{k=0}^{3}\rho_k. \tag{3.6}$$

with ρ_k expressed in (3.4). Each density matrice has equal probability of occurrence as the polarizations encoded are random in the protocol.
The error rate measured by the vendor on the first version of the initial state is:

$$\varepsilon_1 = \text{Tr}\sum_{k=0}^{3}\left(\frac{1}{2}\left|\beta_k^{\perp}\right\rangle\left\langle\beta_k^{\perp}\right|\otimes\mathbb{1}\right)\Lambda\left(\frac{1}{4}\rho_k\right) \tag{3.7}$$

and for the second version:

$$\varepsilon_2 = \text{Tr}\sum_{k=0}^{3}\left(\mathbb{1}\otimes\frac{1}{2}\left|\beta_k^{\perp}\right\rangle\left\langle\beta_k^{\perp}\right|\right)\Lambda\left(\frac{1}{4}\rho_k\right) \tag{3.8}$$

with $|\beta_0\rangle = |H\rangle$, $|\beta_1\rangle = |\sigma^+\rangle$, $|\beta_2\rangle = |V\rangle$, $|\beta_3\rangle = |\sigma^-\rangle$, and $|\beta_k^{\perp}\rangle$ the orthogonal state (for instance $|\beta_0^{\perp}\rangle = |V\rangle$). Measurements on the first version are written on the left side of the Kronecker product $\otimes$ while the ones regarding the second version are on the right side of $\otimes$. The prefactor 1/2 denotes that the vendor is choosing randomly the measurement basis. In order to have more compact expressions of the error rates ε_1 and ε_2 , we introduce the Choi-Jamiolkowski operator $J(\Lambda)$[3] associated to the map Λ. The new expressions of (3.7) and (3.8) are $\varepsilon_1 = \text{Tr}\left(E_1(\mu)J(\Lambda)\right)$ and $\varepsilon_2 = \text{Tr}\left(E_2(\mu)J(\Lambda)\right)$, with $E_1(\mu)$ and $E_2(\mu)$ defined as:

$$\begin{aligned} E_1(\mu) =& \frac{1}{4}\sum_{k=0}^{3}\frac{1}{2}\left|\beta_k^{\perp}\right\rangle\left\langle\beta_k^{\perp}\right|\otimes\mathbb{1}\otimes\overline{\rho_k} \\ E_2(\mu) =& \frac{1}{4}\sum_{k=0}^{3}\mathbb{1}\otimes\frac{1}{2}\left|\beta_k^{\perp}\right\rangle\left\langle\beta_k^{\perp}\right|\otimes\overline{\rho_k} \end{aligned} \tag{3.9}$$

where $\overline{\rho_k}$ is the complex conjugate of ρ_k. Similarly, the losses measured by the vendor on both copies are equal to $\text{Tr}\left(L_1(\mu)J(\Lambda)\right)$ and $\text{Tr}\left(L_2(\mu)J(\Lambda)\right)$, with $L_1(\mu)$ and $L_2(\mu)$

[3] If we consider an entangled state $|\Phi^+\rangle\langle\Phi^+| = \frac{1}{d}\sum_{i,j=1}^{d}|i\rangle\langle j|\otimes|i\rangle\langle j|$, the Choi-Jamiolkowski operator $J(\Lambda)$ associated to the map Λ is defined as: $J(\Lambda) = \frac{1}{d}\sum_{i,j=1}^{d}\Lambda(|i\rangle\langle j|)\otimes|i\rangle\langle j|$.

defined as:

$$\begin{aligned} L_1(\mu) &= \frac{1}{4}\sum_{k=0}^{3} |0\rangle\langle 0| \otimes \mathbb{1} \otimes \overline{\rho_k} \\ L_2(\mu) &= \frac{1}{4}\sum_{k=0}^{3} \mathbb{1} \otimes |0\rangle\langle 0| \otimes \overline{\rho_k}. \end{aligned} \tag{3.10}$$

The next step is to find the optimal map Λ minimizing the error rates measured on both copies given fixed losses $l = e^{-\eta\mu}$, where η is the storage-and-retrieval efficiency of the quantum memory. The detection losses cannot be exploited by malicious agents as the vendor (trusted) is the only party who can access the measurement setup. The losses accessible by the untrusted client are coming from the storage platform which explains why storage losses are taken into account in the analysis. We formulate the client's attack in terms of semidefinite programming [Molina et al., 2013; Watrous, 2011]:

$$\begin{aligned} \min \quad & \mathrm{Tr}\left(E_1(\mu)J(\Lambda)\right) \\ \text{s.t.} \quad & \mathrm{Tr}\left(J(\Lambda)\right) = \mathbb{1} \\ & \mathrm{Tr}\left(E_1(\mu)J(\Lambda)\right) \geqslant \mathrm{Tr}\left(E_2(\mu)J(\Lambda)\right) \\ & \mathrm{Tr}\left(L_1(\mu)J(\Lambda)\right) \leqslant l \\ & \mathrm{Tr}\left(L_2(\mu)J(\Lambda)\right) \leqslant l \\ & J(\Lambda) \geqslant 0 \end{aligned} \tag{3.11}$$

Semidefinite programming solves this optimization problem by testing all possible attacks from the client, represented by the map Λ, to access the one minimizing the error rate $\varepsilon_1 = \mathrm{Tr}\left(E_1(\mu)J(\Lambda)\right)$ given several constraints:

- The trace of the map Λ is equal to the identity.
- The error rate ε_1 on the first version must be larger than or equal to ε_2 (error rate on the second version).
- The losses on both copies should be inferior or equal to the expected losses l.
- The map Λ has to be completely positive.

The minimal noise created by the dishonest client on both copies is the security threshold and is represented on figure 3.2(b) as a function of the average photon number μ, for different memory efficiencies η. As expected, if the quantum memory has an efficiency lower than 50 %, the adversary introduces no errors on the cloning process. In this case, the map Λ models a 50/50 beam splitter separating the two copies. The optimal attack is not as simple to understand for the other memory efficiencies. Figure 3.2(c) displays the security threshold as a function of the memory efficiency for $\mu = 1$. This figure underlines the need of having a high-efficiency and low-noise storage platform to reach the secure regime. The blue data point is the experimental data we achieved after implementation of the protocol including the memory layer.

3.2 Implementation of the quantum money protocol including a quantum memory

After providing the security analysis of the quantum money protocol, we present its implementation using our cold atomic ensemble as a quantum memory layer. An overview of the experimental setup is given, followed by more detailed descriptions about specific components that were crucial for the demonstration of the protocol. The timing of the experiment is shown at the end of the section.

3.2.1 Overview of the experimental setup

The experimental setup is illustrated on figure 3.3. The bank is sending weak coherent states at the single photon level and the information is encoded on the polarization of light using a Pockels cell. More specifically, a quantum random number generator is employed in order to create random bits. For this specific protocol, four different bits need to be generated : $\{00, 01, 10, 11\}$. These bits are then converted to voltages by a digital-to-analog converter (DAC), amplified and sent to the Pockels cell to encode a sequence of random polarization states onto the signal (the possible states being $\{H, \sigma^+, V, \sigma^-\}$). As each polarization corresponds to a different voltage, the voltage gap between two consecutive polarizations changes in the sequence and impacts the fidelity of the qubits encoded. We managed to overcome this issue (see section 3.2.3) and found an optimal temporal sequence for the Pockels cell that enabled to achieve a conditional fidelity of 99.5% for the qubits encoded (without storage).

One requirement to efficiently store a pulse of light into the cloud is that signal and control field should have the same circular polarization (see section 1.6). Nevertheless, the signal could not fulfill this requirement because its polarization is changing randomly in the protocol. In order to overcome that issue, we built a Mach-Zehnder interferometer around the chamber defined by the two beam-displacers on figure 3.3. When the signal enters into the first beam displacer, the original path is decomposed into two different paths, one with the projection on the H polarization and one on V. Then, the V component is converted into H thanks to a half waveplate which is only addressing one path, and finally, both paths are transformed into the same circular polarization thanks to a quarter waveplate. Therefore, the signal propagating in the atom chamber is circularly polarized regardless of the polarization encoded by the Pockels cell. After the atom chamber, the paths are recombined by another beam displacer (BD2) to recreate the original polarization. The visibility and stability of the Mach-Zehnder interferometer are discussed in section 3.2.4.

The photonic state encoded on the signal is stored in the cold atomic ensemble using dynamical EIT (see section 1.2.3). The optical depth is around 400 in order to have a large storage efficiency. The power of the control beam is set to 2 mW with a

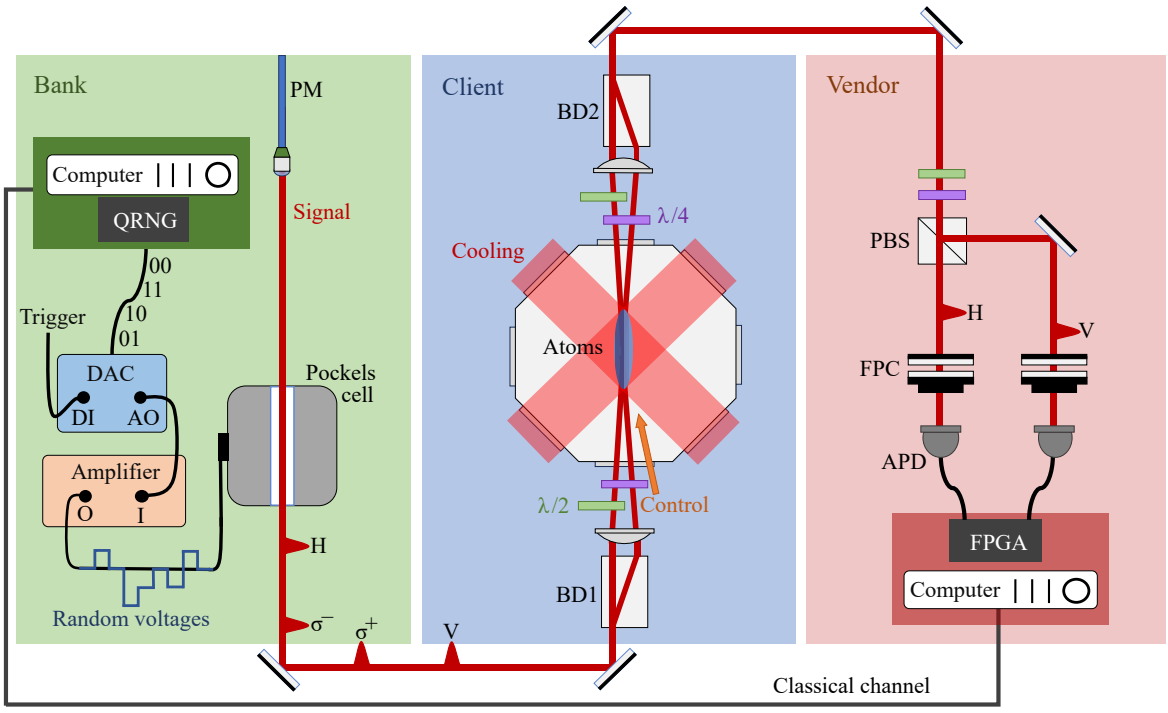

FIGURE 3.3: **Experimental setup.** A quantum random number generator (QRNG) creates a secret key composed of random bits. The bits are converted to voltages by a digital-to-analog converter (DAC), amplified and sent to the Pockels cell to encode random polarizations on weak coherent states. Afterwards, the random qubits are stored in the cold-atom based quantum memory. However, light should be circularly polarized to be efficiently stored into the atomic cloud. For this purpose, a beam displacer (BD1) maps the qubit polarizations into two paths (the first corresponds to the projection on the polarization H and the second to V). A combination of waveplates ($\lambda/2$, $\lambda/4$) transforms both projections into the same circular polarization. An additional beam controls the storage-and-retrieval process. After the atom chamber, the paths are recombined by another beam displacer (BD2) to recreate the original polarizations encoded by the Pockels cell. Then the qubits are measured in $\{H, V\}$ or $\{\sigma^+, \sigma^-\}$ basis thanks to waveplates and a polarizing beam splitter (PBS). Fabry-Perot cavities (FPC) are used to filter out the control beam. The signal is measured with avalanche photodiodes (APD) and data is collected by a field programmable gate array (FPGA). The measurement results are compared to the secret key thanks to a classical channel.

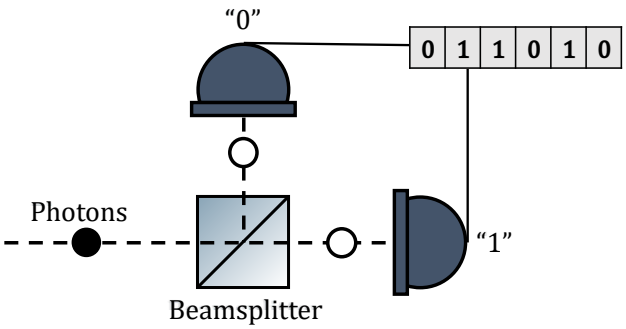

FIGURE 3.4: **Principle of the quantum random number generator from ID Quantique.** Photons are sent onto a 50/50 beamsplitter. If they are transmitted, they will be associated to the binary number "1" and if they are reflected, to the number "0". After some repetitions of this experience, a random sequence of "0" and "1" is generated.

waist of 1 mm. The signal pulse has a gaussian temporal profile with a FWHM (full width half maximum) of 230 ns to match the shape and the width of the transparency window during the storage process. After a controllable storage time, the client reads the memory and hands the qubits to the vendor who measures them in a specific polarization basis ($\{H, V\}$ or $\{\sigma^+, \sigma^-\}$). An half waveplate, a quarter waveplate and a polarizing beam splitter are required to perform the projection. The vendor has to adjust these waveplates to accurately match the detection basis with one encoding basis in order to maximize the overall fidelity with respect to the input state.

Details about specific parts of this experimental setup are given in the following subsections such as the generation of random polarization states, the optimization of their fidelity and also the stability of the Mach-Zehnder interferometer over time.

3.2.2 Generation of random polarization states

The generation of random numbers is required to create random polarization states of light. There are two kinds of random number generators: pseudo-random number generators (PRNGs) and true random number generators (TRNGs). A pseudo-random number generator is a computer program creating sequences of numbers that appear to be random but are actually generated using a deterministic process. Unlike true random number generators, which rely on unpredictable physical phenomena, PRNGs start with an initial value called a seed and use mathematical operations to produce a sequence of numbers. This sequence is thus predictable if one knows the seed and the algorithm used. For this particular reason, it is safer to use true random number generators to realise cryptographic protocols.

Quantum random number generators (QRNGs) are considered as TRNGs because of the intrinsic randomness of quantum mechanics. Our implementation of the quantum money protocol involves one QRNG made by the company ID Quantique which

functions with the following principle (see figure 3.4). Photons are sent onto a 50/50 beamsplitter. If they are transmitted, they will be associated to the binary number "1" and if they are reflected, to the number "0". After some repetitions of this experience, a random sequence of "0" and "1" is generated. The photons sent are weak coherent pulses with a very low average photon number, typically around 0.1 [Stefanov et al., 2000]. The card we used for the quantum money protocol is the Quantis–PCI–4 and is able to generate a random bit stream of 16 Mbits/s.

The next step is to convert the random numbers generated by the QRNG into random polarizations of light. A Pockels cell can perform this operation. Indeed, a Pockels cell is composed of a birefringent crystal: the refractive index is not the same on every axis of the crystal. We consider n_x the refractive index on one of the transverse axis and n_y on the other. An electric field is created in the material by electrodes located on the top and the bottom of the crystal. This electric field modifies n_x and n_y, but more importantly the difference $n_x - n_y$. The polarization of light going through this medium is thus modified. By varying the voltage applied on the crystal, the Pockels cell could act as a half or a quarter waveplate, changing the polarization from H to V, σ^+ or σ^-. As a result, the random numbers generated by the QRNG can be first converted into random voltages by a DAC (USB-6363, National Instruments). Afterwards, these voltages are amplified and sent to the Pockels Cell (LM0202, LINOS) to encode random polarizations of light (see figure 3.5). The amplifier (PZD350A, Trek) was specifically chosen for this experiment as it can produce high voltages up to 700 Volts in a short timescale: the settling time corresponding to 1 % error is on the order of 30 μs. The typical voltages required for our Pockels Cell to create the four polarizations we need are: 0 Volt for H, 150 Volts for σ^+, 300 Volts for V and 450 Volts for σ^-. This process is synchronised with our cold atom experiment thanks to an external trigger sent on the DAC. A python program controls all the operations regarding the QRNG and the DAC to deliver on time the random voltages to the Pockel Cell. After generating random polarization states of light, we must optimize their fidelity in order to minimize the error rate of the communication.

3.2.3 Encoding a sequence of high-fidelity qubits

In the experiment, the Pockels voltage has to change within a short timescale to encode the whole sequence of random qubits in 1 ms[4]. The encoding rate is limited by the settling time of the Pockels amplifier which is on the order of 30 μs. However, the time required for the amplifier to stabilize is longer for the transition $H \rightarrow \sigma^-$ corresponding to a voltage gap of 450 Volts than the transition $V \rightarrow \sigma^-$ corresponding to a voltage gap of 150 Volts.

[4] time window dedicated to the cryptographic protocol in the MOT cycle (see the section 3.9).

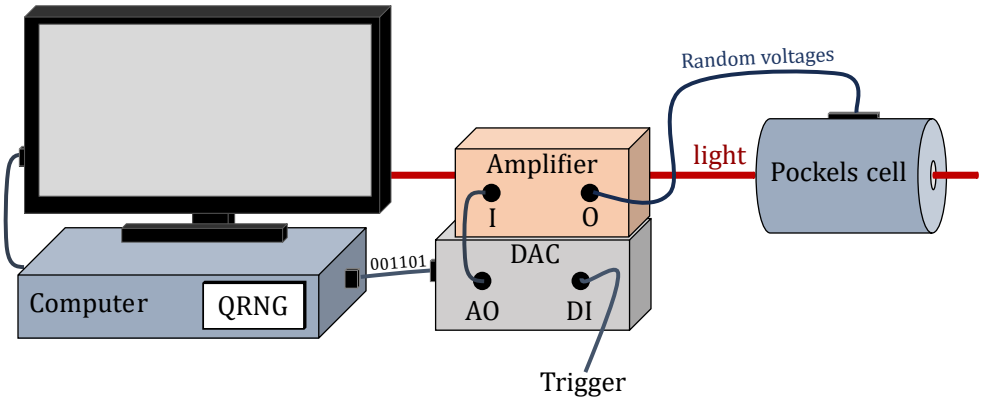

FIGURE 3.5: **Setup for the generation of random polarization states.** I: input, O: output, DI: digital input, AO: analog output. Four different bits are generated by the QRNG : 00, 01, 10 and 11. These random bits are then converted to voltages by a digital-to-analog converter (DAC). Afterwards, the voltages are amplified and sent to the Pockels Cell to encode random polarizations of light. The amplifier (PZD350A, Trek) was specifically chosen for this experiment as it can produce high voltages up to 700 Volts in a short timescale: the settling time corresponding to 1 % error is on the order of 30 μs. This process is synchronised with our cold atom experiment thanks to an external trigger sent on the DAC.

In order to characterize this phenomenon, we measured the error rate of σ^- polarization depending on the previous polarization encoded in the sequence. We considered all the possible transitions: $\sigma^- \rightarrow \sigma^-$, $V \rightarrow \sigma^-$, $\sigma^+ \rightarrow \sigma^-$ and $H \rightarrow \sigma^-$. The time duration between two consecutive voltages is set to 25 μs. The results are presented on the following table[5]:

Transitions	$\sigma^- \rightarrow \sigma^-$	$V \rightarrow \sigma^-$	$\sigma^+ \rightarrow \sigma^-$	$H \rightarrow \sigma^-$
Error rate	$(0.45 \pm 0.04)\%$	$(0.67 \pm 0.05)\%$	$(1.1 \pm 0.07)\%$	$(2.1 \pm 0.09)\%$
Voltage gap	$0\,V$	$150\,V$	$300\,V$	$450\,V$

TABLE 3.1: Error rate of σ^- polarization depending on the previous polarization encoded in the sequence (without intermediate level).

One can notice that the error rate increases with the voltage gap on table 3.1. The fidelity of the polarization encoded thus strongly depends on the type of transition considered. The secret key generated by the QRNG contains all types of transitions as the sequence is totally random. As a result, the mean error rate would be an average of the four data points shown on the table 3.1, corresponding to 1.08%. This value is too high to perform the cryptographic protocol in the secure regime as the encoding is not the only contribution to the final error rate of the communication: other noise sources will be added during the storage-and-retrieval process (see section 3.4). Therefore, an optimization method leading to smaller error rates is required.

[5]The value of σ^- voltage was adjusted by sending a continuous voltage to the Pockels cell. This explains why the lowest error rate is obtained for the transition $\sigma^- \rightarrow \sigma^-$ corresponding to a voltage gap of 0 volt.

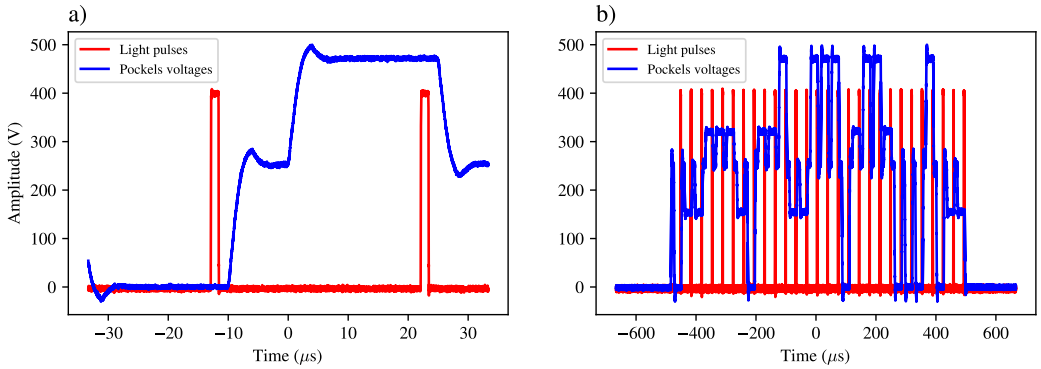

FIGURE 3.6: **Optimal sequence for the Pockels voltages.** The voltages are shown after amplification (blue curve) and the triggers for light pulses are sent 3 µs before the end of each voltage pulse (red curve). As the fidelity of the polarization encoded strongly depends on the type of transitions in the sequence, a 10 μs intermediate level is inserted between each 25 μs random voltage. *a*) represents the transition $H \rightarrow \sigma^-$ with an intermediate voltage of 250 Volts. *b*) is the entire sequence of 1 ms composed of 28 random polarizations.

As the fidelity of the polarization encoded strongly depends on the type of transitions in the sequence, we decided to insert an intermediate level (called I) between each random voltage (see figure 3.6(a)). This intermediate voltage has a length of 10 μs and a voltage equal to 250 Volts which is approximately the middle value between the highest voltage (polarization σ^-) and the the lowest voltage (polarization H). By inserting this intermediate level, the above table 3.1 is reduced to one possible transition being $I \rightarrow \sigma^-$ and the value of σ^- voltage can be adjusted to minimize the error rate for this specific transition. Thus, the error rate is not anymore an average of the results for all different transitions but only the one transition for which the system is optimized. The result obtained after implementation of this method is an error rate equal to (0.35 ± 0.06) %, i.e. a conditional fidelity of (99.5 ± 0.1) %.

3.2.4 Stability of the Mach-Zehnder interferometer over time

After encoding the sequence of qubits, they are sent to the atoms in order to be stored. One requirement to efficiently store a light pulse into the cloud is that signal and control fiels should have the same circular polarization (see section 1.6). Nevertheless, the signal could not fulfill this requirement because its polarization is changing randomly in the protocol. In order to overcome that issue, we built a Mach-Zehnder interferometer around the chamber (see figure 3.7) defined by the two beam-displacers (BD1 and BD2). This technique is called dual-rail encoding [Choi et al., 2008; Vernaz-Gris et al., 2018].

If the polarization encoded by the Pockels cell is linear (H or V), light is propagating along one arm of the interferometer. However, if the polarization is circular (σ^+ or σ^-), light is going through both paths and the visibility of the interference has to be

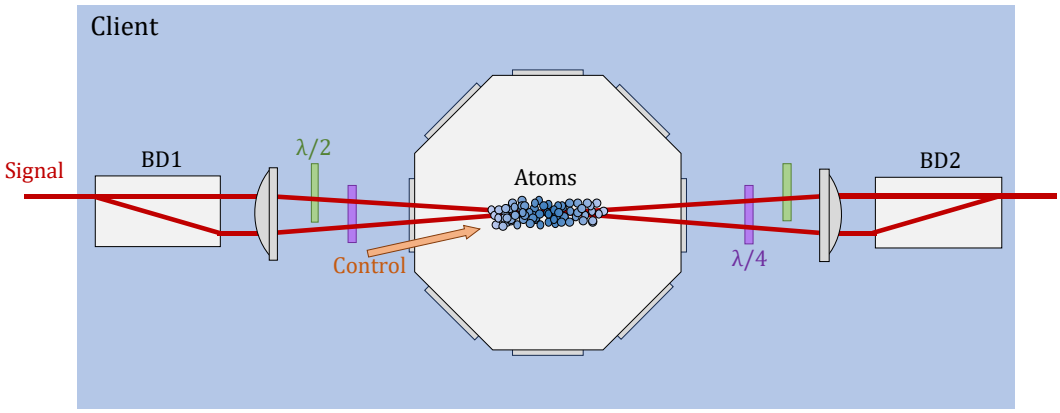

FIGURE 3.7: **Mach-Zehnder interferometer for dual-rail encoding.** The signal should be circularly polarized to be efficiently stored into the atomic cloud. For this purpose, a beam displacer (BD1) maps the qubit polarizations into two paths (the first corresponds to the projection on the polarization H and the second to V). A combination of waveplates ($\lambda/2$, $\lambda/4$) transforms both projections into the same circular polarization. After the atom chamber, the paths are recombined by another beam displacer (BD2) to recreate the original polarizations encoded by the Pockels cell.

maximized to achieve a low error rate[6]. The key element to optimize in this case is the recombination into the second beam displacer. The degrees of freedom we can play with are related to the optics located after the chamber: the position of the second lens (which has to be symmetrical to the first one), the rotation of the quarter and half waveplates, and the alignment of the second beam displacer. At the end of the optimization, the typical visibility obtained is above 99 % (error rate $\varepsilon < 0.5\,\%$).

The stability of the interferometer is also essential in this protocol if one wants to achieve a low error rate for long acquisitions. We placed curtains all around the setup in order to prevent any air flow from perturbing the experiment as it would induce a phase difference between the two paths which would lead to a decrease of the visibility (an increase of the error rate). Figure 3.8 represents the interferometer stability over time. The error rate of the σ^- polarization is measured in the CW regime without storage. The detectors employed to perform this characterization are two powermeters from Thorlabs (S120C) that are taking values every 100 milliseconds. Each data point on figure 3.8 is an average value of the error rate over 30 seconds. One can notice two intervals of time where evolution of the error rate is different. The first one is [0,20] minutes, the second is [20,50] minutes (50 minutes corresponds to the end of the acquisition). During the first interval, the error rate remains fairly static with an average value equal to 0.4% and fluctuations of 0.1%. During the second interval, the error rate evolves linearly as a function of time with a slope of 0.6% per 10 minutes (value extracted from a linear fit). The fluctuations are also four times larger compared to the previous interval with a mean of 0.4%.

[6]The visibility V and the error rate ε are linked with the following relation: $V = 1-2\varepsilon$. Moreover the fidelity $\mathcal{F}$ can be calculated from the visibility thanks to the relation: $\mathcal{F} = (1+3V)/4$.

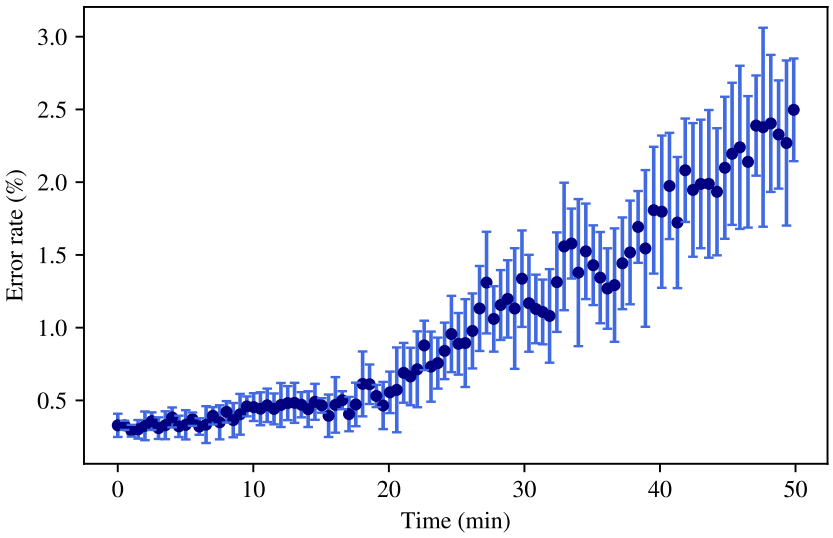

FIGURE 3.8: **Interferometer stability over time.** Evolution the error rate as a function of time when σ^- polarization is sent in the CW regime without storage. Each data point is an average value of the error rate over 30 seconds and its fluctuation is represented by error bars.

The evolution given by figure 3.8 is relevant to determine the duration of the acquisitions when we execute the quantum money protocol. This duration has to be under 20 minutes and a realignment of the interferometer is required every 20 minutes. If we did implement an active locking of the phase difference between the two paths we could achieve a longer stability but we did not due to time constraints. Moreover, the main coils were turned on during the dataset shown in figure 3.8 to be in the same conditions than the real experiment. These coils generate heat in the middle of the interferometer and thus create air flows between hot and cold air. These flows are responsible for the disalignment of the interferometer as they introduce fluctuations on the phase difference between the two paths.

3.2.5 Timing of the experiment

The temporal sequence of the experiment is presented in figure 3.9. The loading, compression and PGC phases are related to atom cooling and are optimized to achieve a cold atomic ensemble with a large optical depth (OD = 400) and temperature of $20\,\mu$K. After this cooling stage, the cold-atom memory has the required properties to perform the cryptographic protocol. The random polarizations are stored and retrieved in and out of the memory using dynamical EIT. The control beam is turned on before the arrival of the signal pulse on the atoms and turned off when the pulse is entirely compressed into the cloud. After a storage time of $1\,\mu$s, the control beam is turned on again to retrieve the initial signal pulse. The FWHM of the signal pulse

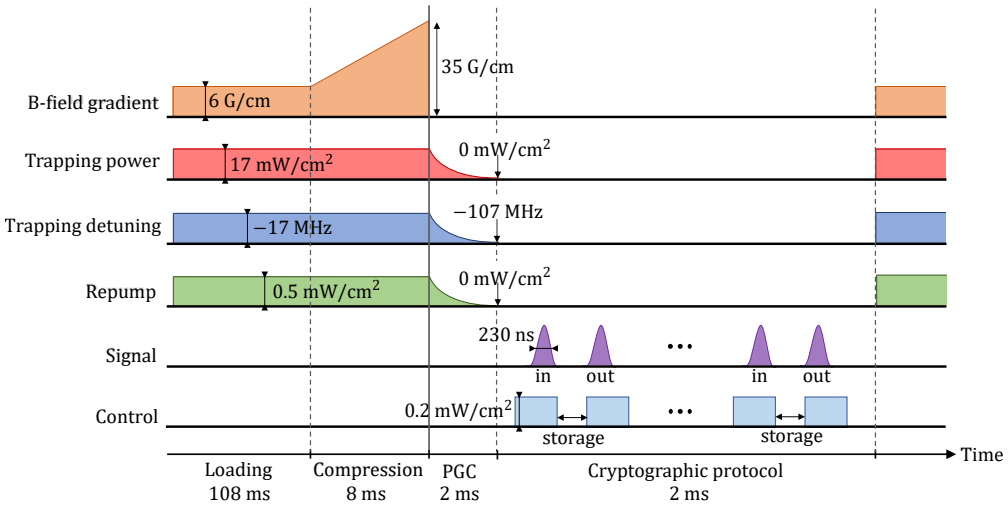

FIGURE 3.9: **Temporal sequence of the experiment.** First, a loading phase of 108 ms begins, in which all the parameters are set in a continuous mode to prepare the MOT. Then, a compression phase is initiated and lasts 8 ms. During this phase, the magnetic field gradient is increased gradually from 6 to 35 G/cm. When the compression stage is finished, the magnetic field is turned off and we perform polarization gradient cooling (PGC) on our atomic cloud during 2 ms by ramping down the trapping power, the trapping detuning and the repump power, following an exponential decay. Then, the cold-atom memory has the required properties to perform the cryptographic protocol. The random polarizations are stored-and-retrieved in and out of the memory using dynamical EIT thanks to a control beam. The storage time is about 1 μs, the FWHM of the signal pulse was set to 230 ns and the control intensity to 0.2 mW/cm^2. The storage-and-retrieval process is repeated 28 times during this last phase of the experiment cycle.

is set to 230 ns and the control intensity to 0.2 mW/cm^2. The storage-and-retrieval process is repeated 28 times during this last phase of the experiment cycle.

3.3 Data analysis and results

The data analysis consists in comparing the data collected by the vendor to a part of the secret key generated by the bank. Indeed, the verification is only done on qubits measured in the right basis, i.e. when the measurement basis is the same than the encoding one. The other qubits are not taken into account in the analysis. A success is reported when the output polarization is the same than the input one, and an error is reported in the other case. If the vendor detects double clicks (one click on both detectors at the same time), the bank counts it both as an error and success. Finally, the error rate is the ratio $N_{\text{error}}/(N_{\text{success}} + N_{\text{error}})$ with N_{success} the number of successes and N_{error} the number of errors. We performed the experiment for four values of average photon numbers: $\mu \in \{0.5, 1, 1.5, 2\}$ in the two measurement basis $\{H/V, \sigma^+/\sigma^-\}$. The secret key generated is different for each measurement and

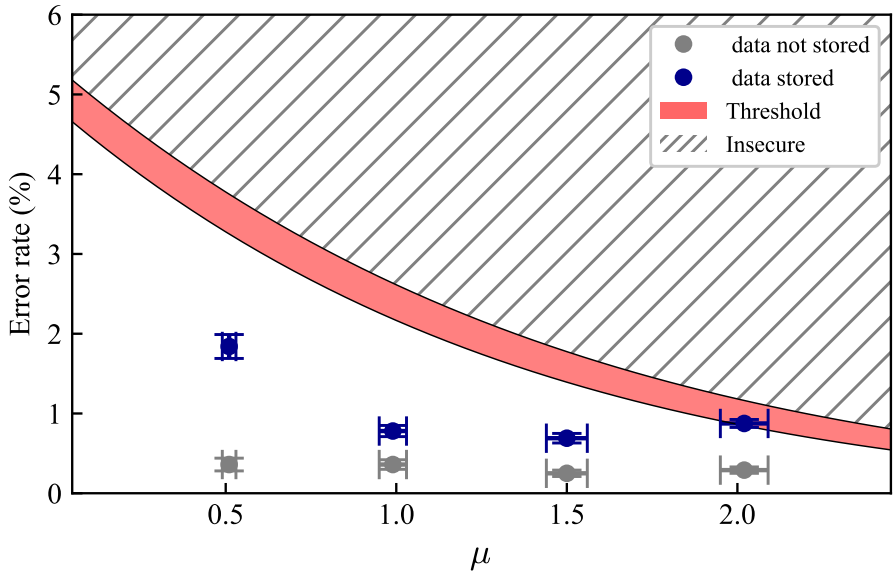

FIGURE 3.10: **Comparison between the security threshold and experimental data.** The error rates are measured for four different values of μ with storage (blue data points) and without storage (grey data points). They are obtained by calculating the mean value between the results of the two measurement basis $\{H/V, \sigma^+/\sigma^-\}$. The error bars on experimental data are estimated by taking into account the statistical uncertainty of photon counts. The light-red area is the security threshold which distinguishes the secure regime from the insecure regime (hatched area). The threshold is determined from the mean efficiency achieved over the four photon numbers $\eta = (77 \pm 2)\%$.

is composed of 28 random polarizations repeated 4000 times. The time duration between two consecutive polarizations in the sequence is set to 35 μs.

Figure 3.10 is a comparison between the security threshold and the experimental data. The data points represent the error rates of the communication for each μ which are obtained by calculating the mean value of the two measurement basis $\{H/V, \sigma^+/\sigma^-\}$. In fact, the probability to measure the data in each basis is the same in the quantum money protocol. The blue dots are the error rates for the complete protocol including the memory and the grey ones are the error rates without the memory (a photonic experiment). The error bars on experimental data are estimated by taking into account the statistical uncertainty of photon counts. The hatched area represents the "insecure" regime and the light-red area is the threshold which distinguishes the secure regime from the insecure regime. If the error rate is above the threshold, the communication is not secured. The threshold is determined from the mean efficiency achieved over the four photon numbers $\eta = (77 \pm 2)\%$. The following table provides details about the blue and grey data points represented on figure 3.10.

μ	0.51 ± 0.02	0.99 ± 0.04	1.50 ± 0.06	2.02 ± 0.07
ε^{ph}	$(0.36 \pm 0.08)\%$	$(0.36 \pm 0.06)\%$	$(0.25 \pm 0.04)\%$	$(0.29 \pm 0.04)\%$
ε^{mem}	$(1.84 \pm 0.15)\%$	$(0.78 \pm 0.07)\%$	$(0.69 \pm 0.06)\%$	$(0.87 \pm 0.05)\%$

TABLE 3.2: Error rates measured for four different values of μ with storage (ε^{mem}) and without storage (ε^{ph}).

The error rates ε^{ph} measured in the photonic experiment (without storage) correspond to conditional fidelities $\mathcal{F} \geq 99.5\,\%$. These are the best results among the implementations of the quantum money protocol in its photonic version [Bozzio et al., 2018; Guan et al., 2018]. It could be explained by the optimization of the sequence sent to the Pockels cell in the encoding stage (see section 3.2.3) and the accurate adjustment of the phase difference between the two arms of the Mach-Zehnder interferometer in order to enhance its visibility (see section 3.2.4).

The error rates ε^{mem} measured in the experiment including the memory are specified in table 3.2. Contrary to the purely photonic case, the error rate at $\mu = 0.5$ is higher than results obtained for other photon numbers due to the signal-to-noise ratio (SNR). Indeed, a new noise source is added when we store the qubits: the control beam. This laser is not coupled to the detectors as there is a 1° angle between the control and the signal paths. Nevertheless, the hot vapor which is surrounding the cold atoms is absorbing the control photons and emitting them spontaneously in all directions. As a result, a part of this emission is oriented on the probe path and creates false clicks on the single-photon counters. This additional noise explains the difference between the error rates ε^{mem} and ε^{ph}. This topic is thoroughly discussed in section 3.4.

The experimental data $\mu = 0.5$ is under the threshold by 8 standard deviations, $\mu = 1$ is under by 18 standard deviations and $\mu = 1.5$ is under by 11 standard deviations. Therefore we achieved the secure regime for the quantum money protocol involving a quantum memory and we can safely perform the protocol for these three different values of μ. The data point $\mu = 2$ is in the limit between the secure and insecure regimes. The protocol becomes more demanding for high photon numbers as a dishonest client can exploit the multi-photon components of the coherent state to minimize the error rate of the two copies.

The stored data shown in figure 3.10 corresponds to a storage time $\delta t = 1\,\mu$s. The memory efficiency decays with storage time due to the residual magnetic field (see section 1.2.4). This decay leads to two consequences : the secure area becomes smaller as the threshold decreases with storage losses and the error rate increases as the SNR drops (the retrieved signal is weaker and the noise added by the control field remains the same). Therefore, the experimental data located in the secure area for a storage time $\delta t = 1\,\mu$s will no longer be secure past a limit value δt_{lim}. Given our

15 μs memory lifetime, the storage time limit for which the data point $\mu = 1$ remains below the security threshold is $\delta t_{\text{lim}} = 6\,\mu$s.

The next step is the analysis of the noise sources in our experiment, more specifically the noise induced by the control beam.

3.4 Study of the control noise

In this section, we will try to give an explanation about the physical phenomena which are responsible for errors in our cryptographic protocol. First we can distinguish two sources of noise: the first one coming from the optical setup without the memory and the second one from the storage-and-retrieval process. Figure 3.10 contains quantitative information about the relative weight of these two contributions. Indeed the grey dots are the errors introduced by the optical setup. They are mainly explained by the intrinsic impurity of the polarization qubits created by the Pockels cell and also the visibility of the interferometer. These two elements have been studied in the sections 3.2.3 and 3.2.4. The blue dots are the errors of the qubits stored in the memory. The difference between these two error rates ($\varepsilon^{\text{mem}} - \varepsilon^{\text{ph}}$) represents the noise added by the storage-and-retrieval process. In the following part, we will focus on this last noise.

3.4.1 Analysis of the physical mechanisms causing the control noise

As mentioned in the previous chapters, an additional laser (called the control beam) is used to store-and-retrieve the polarization states from the quantum memory. As a 1° angle separates the control and the signal paths, this beam is not coupled to the two detectors. Indeed, when all cesium atoms are removed from the vacuum chamber, the control photons are not detected by the single-photon counters (see orange curve in figure 3.11). The dispenser is the source of cesium atoms inside the vacuum chamber. The control noise observed when the dispenser is turned on (purple curve in figure 3.11) corresponds to fluorescence emitted by the hot cesium vapor as the magneto-optical trap was switched off during this acquisition. Starting from this experimental observation, we will analyze the physical mechanisms at play explaining the control noise.

At the end of the cooling stage, the cold atoms are transferred in the ground state $|g\rangle$ that is not addressed by the control beam. Therefore, the cold atomic medium is transparent for this additional field. Nevertheless, there are not only cold atoms in the chamber, but also a hot vapor released by the dispensers. A fraction of cesium atoms composing this vapor is populating the long-lived spin state $|s\rangle$ addressed by the control laser. The hot medium thus absorbs photons from the control field and spontaneously emits them in all directions. A fraction of this light is emitted in the signal path and is responsible for false clicks on the detectors.

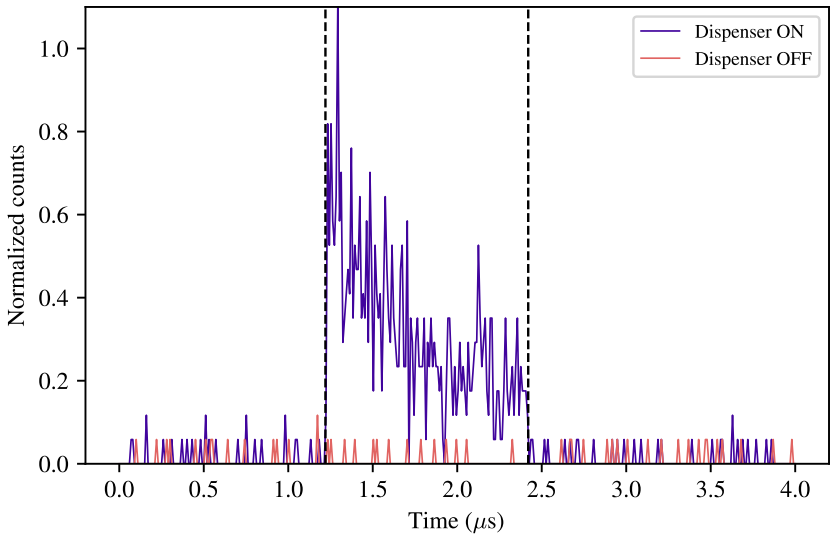

FIGURE 3.11: **Control noise with and without cesium atoms in the vacuum chamber.** The control pulse is delimited by the vertical dashed lines. The dispenser is the source of cesium atoms inside the vacuum chamber. Before taking this measurement, the dispenser was turned off during one complete day to remove all the atoms from the chamber. The control noise observed when the dispenser is turned on corresponds to fluorescence emitted by the hot cesium vapor as the magneto-optical trap was switched off during this acquisition.

The energy levels with their decay channels are presented on figure 3.12. We consider atoms in this hot vapor which are initially in the state $|s\rangle$ (atoms in the state $|g\rangle$ are not addressed by the control laser). After turning on the control beam, atoms are excited from $|s\rangle$ to $|e\rangle$. Then, they could spontaneously decay in $|g\rangle$ or $|s\rangle$ with a decay rate Γ_{eg} or Γ_{es}. Stimulated emission is also possible from $|e\rangle$ to $|s\rangle$. After a few cycles, all the atoms are optically pumped into $|g\rangle$ as the ground state is not addressed by the control beam, leaving empty $|s\rangle$ and $|e\rangle$. Nevertheless, another mechanism enters into account: some atoms are leaving the beam and are replaced by other ones that are in the same energy level or in a different one. Γ_{gs} and Γ_{sg} are the transit rates representing this population exchange. Therefore, the system will reach a steady state where the populations in $|s\rangle$ and $|e\rangle$ are not equal to zero. In other words, control photons are going to be absorbed and re-emitted by the cesium atoms as long as the beam is turned on.

After this qualitative description, equations are required to complete the understanding of the population dynamics. We assume that $\Gamma_{gs} = \Gamma_{sg} = \Gamma_t/2$ with Γ_t being the transit time. In practice, the coherence are relaxing faster than the population which means that the non-diagonal term of the density matrix can be considered in the steady-state regime. As a result, the Bloch equations can be written in terms

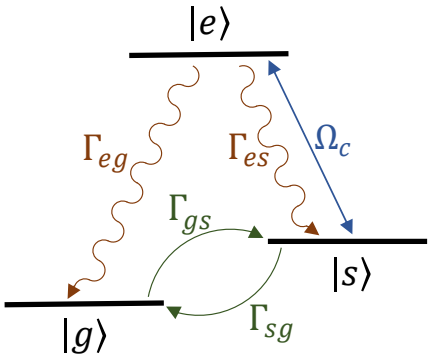

FIGURE 3.12: **Three-level system in the presence of a control field.** Ω_c is the Rabi frequency associated to the control field. Γ_{eg} and Γ_{es} are the spontaneous decay rate from $|e\rangle$ to $|g\rangle$ and $|s\rangle$. Γ_{gs} and Γ_{sg} are the transit relaxation rates which represents the population exchange between the levels $|g\rangle$ and $|s\rangle$ due to atoms entering or leaving the control beam.

of rate equations as:

$$\begin{cases} \dfrac{dN_g}{dt} = \Gamma_{eg} N_e - \dfrac{\Gamma_t}{2}(N_g - N_s) & (3.12) \\ \dfrac{dN_e}{dt} = -\Gamma N_e + B_{es} u_\nu (N_s - N_e) & (3.13) \\ \dfrac{dN_s}{dt} = \Gamma_{es} N_e - B_{es} u_\nu (N_s - N_e) + \dfrac{\Gamma_t}{2}\,(N_g - N_s) & (3.14) \end{cases}$$

where $\Gamma = \Gamma_{eg} + \Gamma_{es}$ is the total decay rate of the excited state and $B_{es}u_\nu$ represents the absorption and stimulated emission rates with B_{es} the Einstein coefficient and u_ν the spectral energy density. One can show that $B_{es}u_\nu = \Omega_c^2/2\frac{\Gamma/2}{(\Gamma/2)^2+(\delta-kv)^2}$ with δ the detuning of the control frequency from the atomic transition $s \to g$ and v the velocity of the atoms [Raimond and Perrin, 2020]. The expression of the transit time Γ_t can be derived by comparing the average velocity v of the atoms (determined by the temperature T of the gas) to the diameter of the control beam (evaluated by its waist w_0). It leads to $\Gamma_t = \frac{1}{w_0\sqrt{2\log(2)}}\sqrt{\frac{8k_bT}{\pi m}}$, with k_b the Boltzmann constant [Urvoy et al., 2013]. We solved this system of equations with Mathematica to get an analytical expression of N_g, N_e and N_s as a function of the time.

Figure 3.13 represents the dynamics of populations in a three-level system in the presence of a control field without transit effect. The Rabi frequency of the control beam is different for the two subplots: $\Omega_c = 2\pi \cdot 1$ MHz in a) and $\Omega_c = 2\pi \cdot 15$ MHz in b). The decay rate of the excited state is $\Gamma = 2\pi \cdot 4.575$ MHz. Atoms are considered at rest for this example. The first case illustrates the regime $\Omega_c \ll \Gamma$ where the population of the excited state remains low and the second one is the regime $\Omega_c \gg \Gamma$ where $N_e \approx N_s$. The evolution of N_e and N_s at very short timescale ($t < 20$ ns) on figure 3.13(b) is determined by the stimulated emission. Moreover, the pumping time is decreasing with the Rabi frequency: 90 % of the population is transferred to the ground state in 3.5 μs for figure 3.13(a) compared to 350 ns for figure 3.13(b).

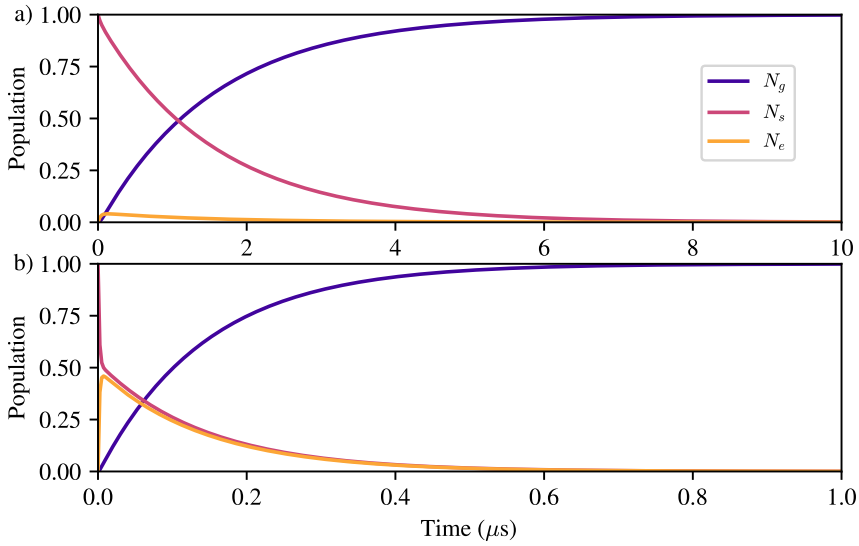

FIGURE 3.13: **Population dynamics in a three-level system in the presence of a control field without transit effect.** The Rabi frequency of the control beam is different for the two subplots: $\Omega_c = 2\pi \cdot 1$ MHz in a) and $\Omega_c = 2\pi \cdot 15$ MHz in b). The decay rate of the excited state is $\Gamma = 2\pi \cdot 4.575$ MHz. Atoms are considered at rest for this example. The first case represents the regime $\Omega_c \ll \Gamma$ where the population of the excited state remains low and the second one is the regime $\Omega_c \gg \Gamma$ where $N_e \approx N_s$. The pumping time is decreasing with the Rabi frequency: 90 % of the population is transferred to the ground state in 3.5 μs for a) compared to 350 ns for b).

However for large Ω_c, the pumping time is limited by the decay rate Γ of the excited state.

As mentioned earlier, the control beam is not coupled to the detectors. Light from stimulated emission is thus not detected and only the spontaneous emission is responsible for false clicks in our cryptographic protocol. The fluorescence rate emitted by the gas is equal to ΓN_e. Therefore, the evolution of the excited-state population over time determines the fluorescence temporal profile observed experimentally in figure 3.11. As we are considering a hot vapor, Doppler broadening has to be taken into account in the process. Therefore, the populations need to be averaged over all possible atom velocities weighted by the Maxwell-Boltzmann distribution. Figure 3.14 presents the evolution of the excited-state population over time for different gas temperature. N_e is normalized on both figures to study its dynamics. The subplot a) does not include the transit effect whereas b) does. The Rabi frequency of the control beam for both figures is $\Omega_c = 2\pi \cdot 15$ MHz. On figure 3.14(a), one can notice that the pumping time is increasing with the temperature of atoms. Indeed, the absorption rate depends on the velocity: fast atoms will absorb control photons with a lower rate than slow atoms as the formula of B_{es} given above shows. When the finite size of the beam is taken into account, N_e is not converging to zero (see figure 3.14(b)). The waist of the control beam is set to 0.7 mm corresponding to the experimental value.

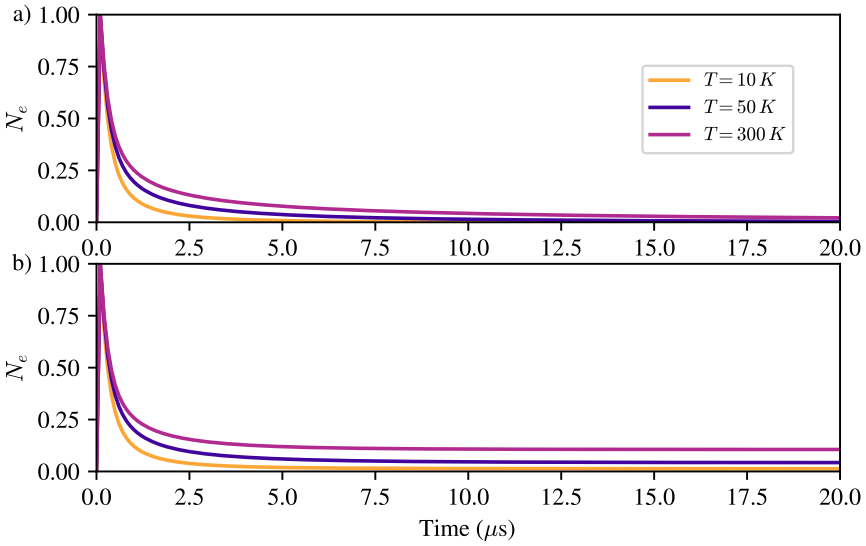

FIGURE 3.14: **Evolution of the excited-state population over time for different gas temperature.** N_e is normalized on both figures to study its dynamics. *a*) does not include the transit effect whereas *b*) does. The Rabi frequency of the control beam for both figures is $\Omega_c = 2\pi \cdot 15$ MHz. On figure *b*), the time to reach the steady-state regime is determined by $1/\Gamma_t$ which is inversely proportional to the square root of the gas temperature. The waist of the control beam is set to 0.7 mm.

The time to reach the steady-state regime is determined by $1/\Gamma_t$ which is inversely proportional to the square root of the gas temperature. This feature is illustrated on the second subplot: the steady-state value is reached earlier for $T = 300\,\mathrm{K}$ than for $T = 50\,\mathrm{K}$ and $T = 10\,\mathrm{K}$.

In order to compare the fluorescence profile measured in figure 3.11 with the evolution of the excited state population described by our model, some experimental elements have to be considered.

3.4.2 Simulation of the control noise in experimental conditions

The control noise is filtered by a Fabry-Perot cavity (FPE001A, Quantaser). This Fabry-Perot cavity (FPC) has a free-spectral range about 16 GHz and a 60 MHz bandwidth (45 dB rejection at the control frequency). Fluorescence resulting from the decay $|e\rangle \rightarrow |s\rangle$ is at the control frequency and is thus filtered by the FPC. However, scattered photons produced by the decay $|e\rangle \rightarrow |g\rangle$ are at the signal frequency. These photons are experiencing strong Doppler broadening as they are emitted by the hot vapor. The FPC attenuates fluorescence from fast atoms compared to slow ones due to their Doppler shift. Therefore, the spectral filtering of the cavity has to be taken into account as it determines the velocity range of atoms participating to the noise detected by the single-photon counters.

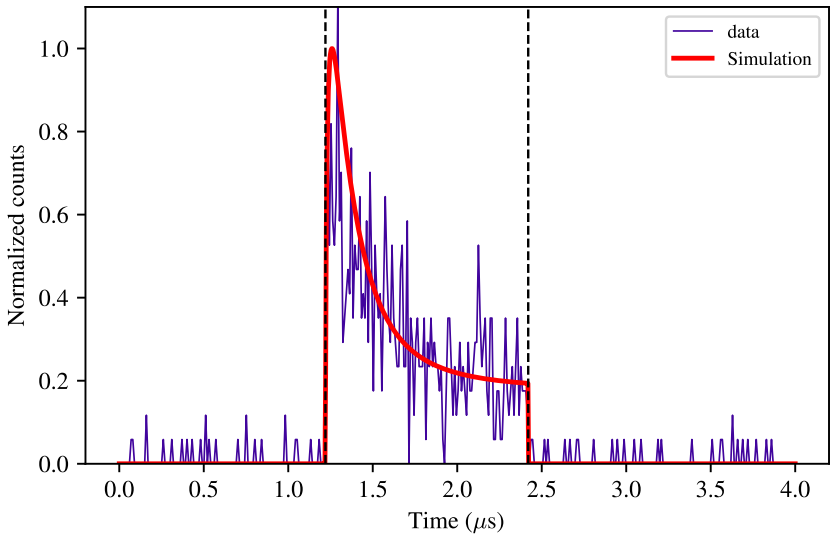

FIGURE 3.15: **Simulation of the control noise profile.** The control noise is simulated in the time range defined by the vertical dashed line, i.e. when the control beam is turned on. This simulation takes into account the impact of spectral and spatial filtering on the fluorescence emitted by the hot vapor. The vapor is assumed to be at room temperature. Experimental data of the control noise is represented in the background.

Moreover, the control noise is also spatially filtered as the signal is coupled to a single-mode fiber before going to the detection setup. This single-mode fiber collects photons emitted in spatial mode of the signal. As a result, atoms interacting with the control field must be located on the signal path to contribute to the noise detected during the cryptographic protocol. In this case, the transit rate perceived after spatial filtering is not the same than the one before, due to the projection on the signal's spatial mode (the waist of the signal beam is $w_0 = 126\,\mu$m).

The temporal profile of the fluorescence emitted by the cesium gas after spatial and spectral filtering is illustrated in figure 3.15. The control noise is simulated in the time range defined by the vertical dashed line, i.e. when the control beam is turned on. The vapor is assumed to be at room temperature. Experimental data of the control noise is represented in the background. The fluorescence decay calculated from the model seems to be in good agreement with the measurement data. The temporal profile of the control noise predicted by our model is thus consistent with experimental observations.

3.5 Conclusion

This chapter reports the first experimental implementation of the quantum money protocol including a memory layer. The experimental setup was outlined, emphasizing the fine-tuning of the voltage sequence sent to the Pockels cell, resulting in a 99.5 % conditional fidelity for the encoded qubits. The visibility obtained for the Mach-Zehnder interferometer exceeds 99 %, and its stability over time was evaluated, showing a stable visibility over a period of 20 minutes. The secure regime of the protocol was achieved for three different photon numbers $\mu = 0.5$, 1 and 1.5. Based on our 15 μs memory lifetime, the storage time limit for which the data point $\mu = 1$ remains below the security threshold is $\delta t_{\text{lim}} = 6\,\mu$s. Finally, an analysis of the control noise was conducted in order to understand the physical mechanisms responsible for errors in our cryptographic protocol.

An improvement of the experiment would be to store the whole sequence of random polarizations at once. This could be possible by spatially multiplexing our quantum memory. This topic is studied in the next chapter.

CHAPTER 4

TOWARDS THE IMPLEMENTATION OF SPATIAL MULTIPLEXING

Contents

As for classical communication, multiplexing is useful for the field of quantum communication. A critical challenge is to go beyond single-mode quantum memories and to store many modes at the same time. It could be used to improve the achievable rates for creating entanglement between light and quantum memories in a quantum network, as it is equivalent to running the protocol for each mode in parallel [Collins et al., 2007]. Several multiplexing methods can be explored depending on the degrees of freedom available for a specific storage platform, such as multiplexing in time [Jobez et al., 2016; Lago-Rivera et al., 2021], frequency [Seri et al., 2019], and space [Nicolas et al., 2014; Pu et al., 2017]. Temporal multiplexing is not compatible with the EIT scheme due to the control field which cannot store an excitation without reading the previous one. However, the EIT scheme is compatible with spatial multiplexing, as [Jiang et al., 2019] demonstrated by addressing 210 different memory cells spatially separated with acousto-optic deflectors (AODs). Another method would be to store

multiple transverse modes of light, which are orthogonal between each others and superposed in one beam. This is possible using spatially superposed Hermite-Gaussian modes (HG) created for instance by devices based on multi-plane light conversion (MPLC). The multimode capacity characterises the number of modes that a memory can store and retrieve with a high efficiency ($\eta > 50\,\%$ for instance). The goal of this chapter is to numerical simulate the multimode capacity of our quantum memory with theses two methods.

4.1 Multiplexing with spatially-superposed Hermite-Gaussian modes

Space division multiplexing (SDM) was first employed in classical communications by simultaneously transmitting multiple spatial modes through multimode or multicore fibers [Richardson et al., 2013]. This technique could be used in the context of quantum networks and the storage of spatial modes in quantum memories is thus a relevant topic to investigate. This section presents the case of spatially-superposed Hermite-Gaussian modes interfaced with a cold-atom based quantum memory.

4.1.1 Hermite-Gaussian modes

Hermite-Gaussian modes are a set of solutions to the paraxial wave equation in optics that describe the transverse spatial modes of an optical resonator. These modes are named after Charles Hermite and Carl Friedrich Gauss. They constitute an orthogonal basis which could be used for multiplexing.

The electric field distribution of a Hermite-Gaussian mode are described as a product of Hermite polynomials and Gaussian functions. The transverse spatial profiles of these modes have a rectangular symmetry, which is characterized by the number of nodes and antinodes in the horizontal and vertical directions. The mode indices, often denoted as m and n, specify the number of peaks (antinodes) along the x and y axes, respectively. The amplitude of the electric field can be written as:

$$E_{mn}(x, y, z) = u_m(x, z)u_n(y, z)e^{-ikz} \tag{4.1}$$

where u_j ($j = \{m, n\}$) is equal to:

$$u_j(x, z) = \left(\frac{\sqrt{2/\pi}}{2^j j! w_0}\right)^{\frac{1}{2}} \left(\frac{q_0}{q(z)}\right)^{\frac{1}{2}} \left(\frac{-q(z)^*}{q(z)}\right)^{\frac{j}{2}} H_j\left(\frac{\sqrt{2}x}{w(z)}\right) e^{-i\frac{kx^2}{2q(z)}} \tag{4.2}$$

with the waist of the fundamental Gaussian mode $w(z) = w_0\sqrt{1 + (z/z_R)^2}$ and the complex beam parameter $q(z) = z + iz_R$, $z_R = \pi w_0^2/\lambda$ being the Rayleigh range.
H_j is the j-th order Hermite polynomial and is defined as (physicist form[1]):

[1]Two versions of Hermite polynomials exist. For instance, $H_1(x) = 2x$ in the physicist form whereas $H_1(x) = x$ in the probabilistic form. In this work, we are using the physicist form.

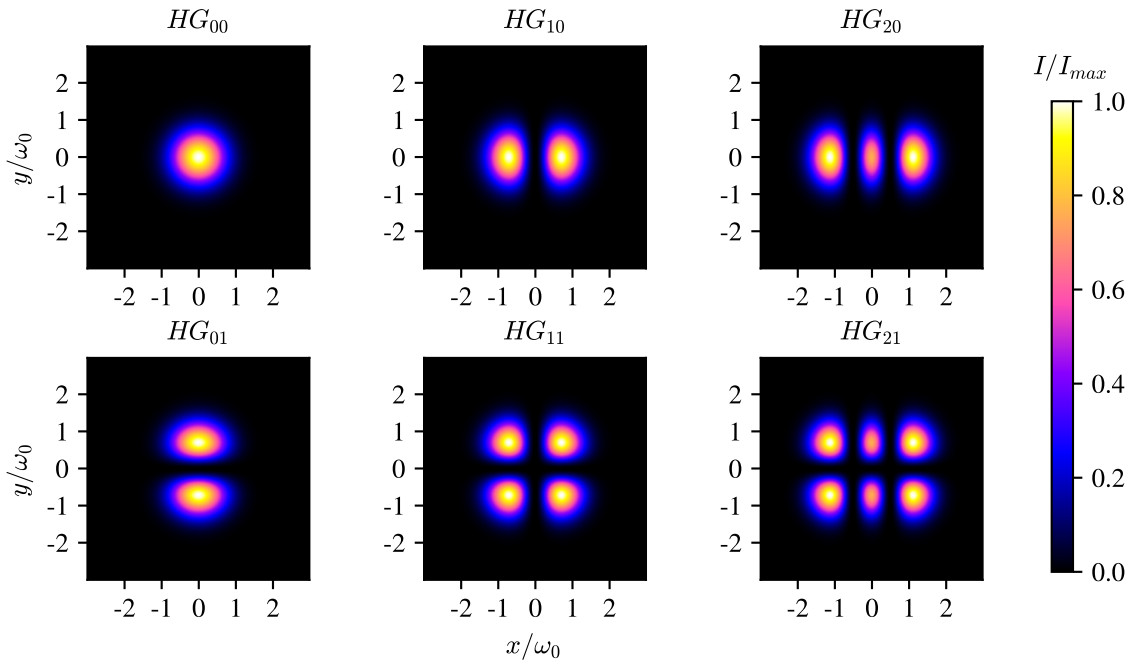

FIGURE 4.1: **Transverse intensity profiles of the first Hermite-Gaussian modes in the xOy plane.** The HG$_{mn}$ modes exhibit a rectangular symmetry with $m+1$ maxima in the direction x and $n+1$ maxima in the direction y which gives a total of $(m+1)(n+1)$ intensity peaks.

$$H_j(x) = (-1)^j e^{x^2} \frac{d^j}{dx^j} e^{-x^2}. \tag{4.3}$$

The transverse intensity profiles of the first Hermite-Gaussian modes are represented on figure 4.1 at $z = 0$. The modes HG$_{\mathrm{m0}}$ exhibit $m+1$ maxima in the direction x as it is shown on the profiles of HG$_{00}$ (one maximum), HG$_{10}$ (two maxima) and HG$_{20}$ (three maxima). The modes HG$_{\mathrm{0n}}$ exhibit $n+1$ maxima in the direction y as it is shown on the profiles of HG$_{00}$ (one maximum) and HG$_{01}$ (two maxima). The modes HG$_{mn}$ thus have $m+1$ maxima in the direction x and $n+1$ maxima in the direction y which gives a total of $(m+1)(n+1)$ peaks as illustrated on the profiles of HG$_{11}$ (four peaks) and HG$_{21}$ (six peaks).

The longitudinal intensity profiles of Hermite-Gaussian modes are represented on figure 4.2 in the xOz plane. The index n of HG$_{mn}$ modes is not given because it does not have an impact on the longitudinal profiles in the xOz plane. Their waists (red curves) define the evolution of the transverse beam size over the z-axis. The waist $w_m(z)$[2] of HG$_{mn}$ modes in xOz plane can be expressed as [Carter, 1980]:

$$w_m(z) = \sqrt{m + \frac{1}{2}} \cdot w(z) \tag{4.4}$$

[2]The waist $w_m(z)$ is defined as the $1/e^2$ half-width of the transverse intensity profile at z position.

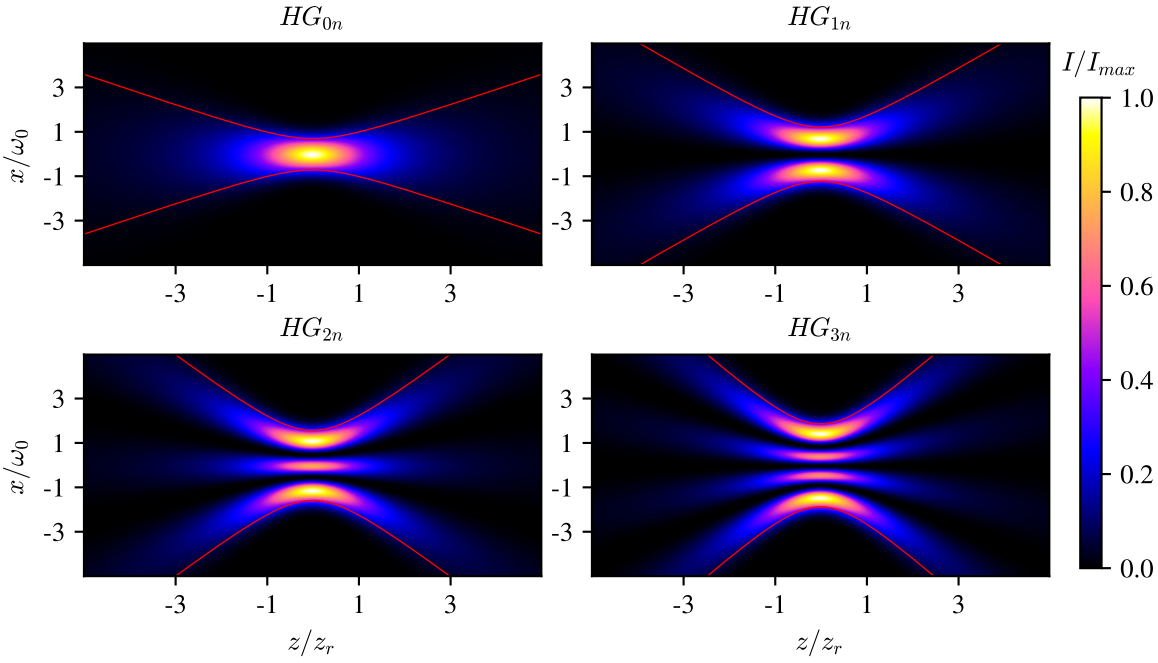

FIGURE 4.2: **Longitudinal intensity profiles of Hermite-Gaussian modes in the xOz plane.** The index n of HG_{mn} modes is not given here because it does not have an impact on the longitudinal profiles in the $x0z$ plane. Their waists (red curves) define the evolution of the transverse beam size over the z-axis and scales as $\sqrt{m+1/2}$ in this specific plane.

with $w(z)$ the waist of the fundamental Gaussian beam HG_{00}. In the yOz plane, HG_{mn} modes thus have a waist $w_n(z)$. Their radial divergence are given by a linear combination of the two waists $w_m(z)$ and $w_n(z)$.

4.1.2 Generation of spatially-superposed HG modes using MPLC

Hermite-Gaussian modes can be generated from a Gaussian mode by reflecting on a phase mask controlled by a spatial light modulator (SLM). However if one wants to map spatially separated Gaussian modes into a combination of HG modes and inversely, the solution is more complex. One method is called multi-plane light conversion (MPLC). This technique was first developed in [Morizur et al., 2010] by the founders of the company Cailabs. The principle is to use a multipass cavity composed of reflective phase plates positioned in front of a mirror. Each input beam is reflected multiple times on the phase plates but at different position as they were initially separated. Therefore, they acquire different phase profiles during their propagation in the cavity: one Gaussian beam is transformed into a particular HG mode after the last reflection. The phase masks are designed with a very high resolution (millions of pixels) to perform this operation. The separation between the beams is decreasing after each reflection leading to HG modes perfectly superposed at the output of the cavity.

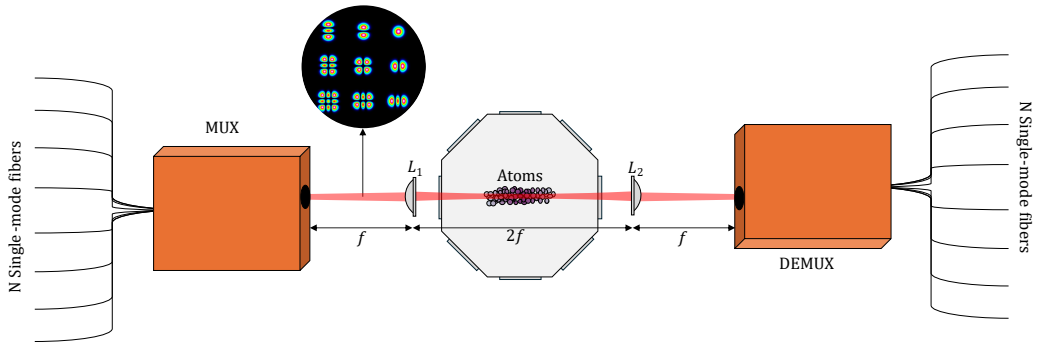

FIGURE 4.3: **Simplified setup of a spatially multiplexed quantum memory using MPLC devices from Cailabs.** Several fundamental Gaussian beams are propagating in single mode fibers and are transformed into a combination of multiple Hermite-Gaussian modes at the output of the multiplexer (MUX). This combination is stored in the atomic ensemble and retrieved on demand. The demultiplexer (DEMUX) performs the reverse operation, i.e. converting the HG modes into separated fundamental Gaussian modes. Each output fiber of the DEMUX device corresponds to a specific HG profile stored in the memory. In practice, a $4f$ optical system composed of two lenses (L_1 and L_2 with the same focal length f) images the plane located at the output of the multiplexer on the input of the demultiplexer.

Figure 4.3 shows a simplified setup of how one can employ Cailabs devices [Bade et al., 2018] based on MPLC to multiplex our quantum memory. Several fundamental Gaussian beams are propagating in single mode fibers which are coupled to the multipass cavity inside the multiplexer device (MUX). At the MUX output, one beam containing the combination of multiple Hermite-Gaussian modes (as many as the number of input fibers) is sent to the cold atomic ensemble. After the storage-and-retrieval process, superposed HG modes are separated and converted into Gaussian beams coupled in optical fibers. One output fiber corresponds to one mode. This operation is done by using the MPLC device in the opposite direction, which acts as a demultiplexer (DEMUX). In practice, a $4f$ optical system composed of two lenses (L_1 and L_2 with the same focal length f) images the plane located at the output of the multiplexer on the input of the demultiplexer. The lens L_1 focuses HG modes on the atomic cloud in order to maximize the overlap between light and atoms, in other words to increase the optical depth seen by the modes. The importance of this last point on the multimode capacity of the memory is addressed in the next section.

A typical measure of cross-talks between modes without atoms is presented on figure 4.4(b) for a MUX+DEMUX system with 15 channels. For each input mode $\mathrm{HG_{i,j}}$, we measured the power $P_{i,j}$ in this mode at the output of the demultiplexer and the leakage in the other channels $P_{i',j'}$. Cross-talks between modes in decibels are defined as $10\log(P_{i,j}/P_{i',j'})$. The average cross-talk is -21.03 dB. Figure 4.4(a) shows the coupling efficiency of each channel, defined as the ratio between the power before and after the MUX+DEMUX devices for a specific mode. The average coupling efficiency is -10.25 dB.

a)

(dB)	Coupling efficiency
HG=00 input	-9.32
HG=10 input	-7.89
HG=01 input	-10.39
HG=20 input	-8.35
HG=11 input	-9.63
HG=02 input	-8.78
HG=30 input	-9.65
HG=21 input	-12.22
HG=12 input	-11.98
HG=03 input	-9.64
HG=40 input	-9.54
HG=04 input	-10.90
HG=22 input	-17.36
HG=31 input	-12.21
HG=13 input	-13.38

b)

(dB)	HG=00 output	HG=10 output	HG=01 output	HG=20 output	HG=11 output	HG=02 output	HG=30 output	HG=21 output	HG=12 output	HG=03 output	HG=40 output	HG=04 output	HG=22 output	HG=31 output	HG=13 output
HG=00 input		-39,09	-36,59	-22,99	-28,65	-28,80	-19,16	-22,44	-28,58	-37,34	-23,06	-21,54	-29,62	-19,02	-20,46
HG=10 input	-37,51		-21,42	-20,23	-37,21	-24,23	-16,17	-19,51	-19,04	-27,95	-19,82	-35,94	-17,97	-21,26	-33,52
HG=01 input	-37,61	-22,94		-30,58	-37,30	-22,18	-24,27	-22,39	-21,67	-23,33	-37,39	-18,38	-29,57	-27,10	-26,14
HG=20 input	-22,62	-21,24	-21,54		-23,62	-28,77	-13,92	-14,36	-21,69	-37,31	-18,95	-36,05	-13,22	-17,46	-26,16
HG=11 input	-37,40	-38,83	-36,33	-25,06		-28,54	-24,06	-17,72	-28,33	-37,08	-37,18	-35,82	-29,36	-17,22	-17,82
HG=02 input	-37,54	-38,97	-21,45	-30,52	-23,54		-30,40	-22,32	-17,48	-13,16	-37,33	-16,53	-13,13	-27,04	-26,08
HG=30 input	-26,03	-23,50	-25,74	-22,00	-29,16	-38,70		-22,95	-35,51	-21,69	-11,36	-25,25	-15,54	-13,10	-26,70
HG=21 input	-37,33	-38,76	-24,90	-20,05	-19,58	-37,87	-30,19		-34,68	-23,05	-25,93	-24,41	-14,70	-15,13	-17,75
HG=12 input	-38,10	-20,47	-37,03	-39,07	-24,09	-24,81	-22,30	-32,73		-37,78	-37,88	-20,15	-15,47	-35,21	-15,85
HG=03 input	-25,56	-25,93	-19,65	-38,67	-23,69	-17,57	-30,55	-34,79	-35,04		-37,48	-11,87	-15,07	-21,44	-13,81
HG=40 input	-25,46	-18,23	-36,52	-18,06	-28,59	-28,74	-15,31	-34,69	-34,94	-28,03		-36,02	-13,18	-27,09	-33,60
HG=04 input	-37,63	-25,87	-21,55	-21,47	-37,33	-24,35	-37,31	-32,27	-28,56	-12,98	-26,24		-18,09	-34,75	-33,64
HG=22 input	-22,93	-23,27	-36,87	-23,28	-28,93	-22,51	-24,60	-22,72	-35,29	-23,67	-26,54	-36,36		-19,30	-26,47
HG=31 input	-37,81	-39,24	-36,74	-23,15	-21,54	-38,35	-15,97	-19,81	-28,74	-23,54	-37,60	-36,24	-29,78		-18,23
HG=13 input	-37,88	-23,21	-25,46	-23,22	-21,61	-24,60	-24,54	-34,98	-17,82	-15,62	-37,67	-19,94	-15,26	-27,38	

FIGURE 4.4: **Coupling efficiencies and cross-talks between channels for a MUX+DEMUX system with 15 channels without atoms.** Figure *a*) shows the coupling efficiency of each channel, being defined as the ratio between the power before and after the MUX+DEMUX devices for a specific mode. The average coupling efficiency is -10.25 dB. Cross-talks between modes are represented on figure *b*). The average cross-talk is -21.03 dB.

4.1.3 Multimode capacity of EIT-based quantum memory with HG modes

In the context of quantum memories, the Fresnel number is defined as $F = \sigma^2/(\lambda L)$ and characterises the ability for a memory to efficiently store multiple modes depending on its geometry (σ being its transverse size and L its length, see figure 4.5). First the Fresnel number is inversely proportional to L. Indeed, as the modes are diverging, a long ensemble will induce leakage on the edges leading to a decrease in memory efficiency. Moreover F is proportional to σ: a large transverse section enables to store a large amount of high-order modes as their divergence increases as the square root of the mode order. The multimode capacity of a memory thus scales with the Fresnel number. This section gives a theoretical description of the storage-and-retrieval process for superposed HG modes and assesses the multimode capacity of the memory for different experimental parameters to find the optimal configuration for our cold-atom experiment. The theory is based on two papers from Anders Sørensen's group [Grodecka-Grad et al., 2012; Zeuthen et al., 2011]. Their work was about spatial multiplexing with Bessel beams and I applied it to other multiplexing techniques (with Hermite-Gaussian beams in this section and a 2D array of Gaussian beams in section 4.2).

Theory

This study is done in the Heisenberg picture (time-dependant operators) with quantized electromagnetic field for the signal and classical light for the control. The mathematical formalism is similar than the one used in the section 1.2.3, except the fact that we are considering a combination of transverse modes instead of multiple wavevectors. The signal field can thus be written as:

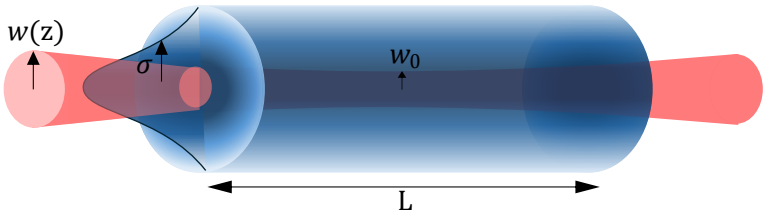

FIGURE 4.5: **Configuration for the multiplexing calculations.** The atomic density (blue area) is chosen constant over a distance L on the z-axis and Gaussian on the transverse plane: $n(x,y) = n_0 e^{-2(x^2+y^2)/\sigma^2}$ with σ the "atomic waist". The fundamental HG_{00} mode is represented, $w(z)$ being its waist at a position z and w_0 at $z = 0$. The overlap between the beam and the atomic ensemble is only determined by σ, w_0 and L.

$$\hat{E}_s = \sum_{mn} E_{mn} \hat{a}_{mn} \tag{4.5}$$

where $\hat{a}_{mn}$ is the annihilation operator of a specific HG_{mn} mode and E_{mn} its amplitude. The atomic density is chosen constant over z-axis and Gaussian on the transverse plane: $n(x,y) = n_0 e^{-2(x^2+y^2)/\sigma^2}$ with σ the "atomic waist". The fundamental HG_{00} mode is represented with the atomic ensemble on figure 4.5. L is the length of the ensemble, $w(z)$ is the waist at a position z of HG_{00} and w_0 at $z = 0$. As HG modes are orthogonal, one might think that their spin-waves are also orthogonal while they are stored in the memory. However, their orthogonality is not preserved due to the atomic density profile which induces cross-talks between stored modes. The cross-talk between different orders (m,n) and (m',n') is modeled by the coupling term $B_{mn,m'n'}$:

$$B_{mn,m'n'} = \frac{1}{n_0 L} \int_{x,y,z} E_{mn}(x,y,z) E^*_{m'n'}(x,y,z) n(x,y) dx dy dz \tag{4.6}$$

with E_{mn} the amplitude of HG_{mn} given by (4.1) and $E_{m'n'}$ the amplitude of $HG_{m'n'}$. The overlap between HG_{mn} and the atomic ensemble is determined by $B_{mn,mn}$ ($m = m'$ and $n = n'$). The expression (4.6) is averaged over the z-axis in order to take into account the mode divergence over the cloud length.

The equations (1.32), (1.34) and (1.37) of the first chapter can be used again with a slight modification (the vacuum Rabi frequency Ω_0 has to be transformed into $\Omega_0 \sum_{m'n'} B_{mn,m'n'}$ to include couplings between different modes) to describe the storage-and-retrieval process of superposed HG beams:

$$\begin{cases} \dfrac{\partial \hat{\sigma}^{mn}_{ge}}{\partial t} = -\gamma_{ge} \hat{\sigma}^{mn}_{ge} + \dfrac{i}{2} \Omega_c \hat{\sigma}^{mn}_{gs} + \dfrac{i}{2} \Omega_0 \sum_{m'n'} B_{mn,m'n'} \hat{a}_{m'n'} & (4.7) \\ \dfrac{\partial \hat{\sigma}^{mn}_{gs}}{\partial t} = \dfrac{i}{2} \Omega_c \hat{\sigma}^{mn}_{ge} & (4.8) \\ \left(\dfrac{\partial}{\partial t} + c \dfrac{\partial}{\partial z} \right) \cdot \hat{a}_{mn} = i \dfrac{\Omega_0}{2} N \sum_{m'n'} B_{mn,m'n'} \hat{\sigma}^{m'n'}_{ge} & (4.9) \end{cases}$$

with Ω_c the control Rabi frequency, $\gamma_{ge} = \Gamma/2$ the relaxation rate of the coherences between the excited and the ground state. $\hat{\sigma}^{mn}$ are the atomic operators for a specific HG_{mn}.

In a first step, a few changes on the variables are going to be operated. We take a comoving frame $t' = t - z/c$ and new dimensionless variables in order to simplify these equations: $\tilde{z} = z/L$, $\tilde{t} = \Gamma t'$ and $\tilde{\Omega} = \Omega/\Gamma$. The definition of the operators $\hat{\sigma}$ and $\hat{a}$ are modified by a constant: $\hat{\sigma}^{mn} \rightarrow \hat{\sigma}^{mn}\sqrt{L}/\sqrt{N}$ and $\hat{a}_{mn} \rightarrow \hat{a}_{mn}/\sqrt{\Gamma}$. Moreover, the excited state is considered as adiabatically eliminated ($\partial\hat{\sigma}^{mn}_{ge}/\partial t \approx 0$). To ease the transition to numerical simulations, we introduce the operator vectors $\vec{a} = (\hat{a}_{mn})$, $\vec{\sigma} = (\hat{\sigma}^{mn})$ which group all the modes together and the coupling matrix $\mathbb{B} = (B_{mn,m'n'})$. It leads to:

$$\begin{cases} \vec{\sigma}_{ge}(\tilde{z},\tilde{t}) = i\tilde{\Omega}_c\vec{\sigma}_{gs}(\tilde{z},\tilde{t}) + i\sqrt{d_0}\mathbb{B}\vec{a}(\tilde{z},\tilde{t}) & (4.10) \\ \dfrac{\partial}{\partial\tilde{t}}\vec{\sigma}_{gs}(\tilde{z},\tilde{t}) = \dfrac{i}{2}\tilde{\Omega}_c\vec{\sigma}_{ge}(\tilde{z},\tilde{t}) & (4.11) \\ \dfrac{\partial}{\partial\tilde{z}}\vec{a}(\tilde{z},\tilde{t}) = \dfrac{i}{2}\sqrt{d_0}\mathbb{B}\vec{\sigma}_{ge}(\tilde{z},\tilde{t}) & (4.12) \end{cases}$$

where $d_0 = \frac{\Omega_0^2 NL}{c\Gamma}$ is the peak optical depth. One can note that $\sqrt{d_0}$ appears as a prefactor of the coupling matrix in the above equations. If we look at the diagonal terms of $\sqrt{d_0}\mathbb{B}$, they define the square root of the optical depth perceived by each mode. High-order modes have a low overlap with the cloud due to their larger divergence and will result into low OD. This divergence thus limits the multimode capacity of the quantum memory [Grodecka-Grad et al., 2012].

The expression of $\vec{\sigma}_{ge}$ in (4.10) can be injected into (4.11) and (4.12). Then, we define the Laplace transform in the space coordinate $\tilde{z}$ as $\mathscr{L}(f)(u) = \int_{\tilde{z}=0}^{+\infty} f(\tilde{z})e^{-iu\tilde{z}}d\tilde{z}$ where the momentum u is a real number. This Laplace transform is applied to the above equations:

$$\begin{cases} \dfrac{\partial}{\partial\tilde{t}}\vec{\sigma}_{gs}(u,\tilde{t}) = -\dfrac{1}{2}\tilde{\Omega}_c^2\vec{\sigma}_{gs}(u,\tilde{t}) - \dfrac{1}{2}\tilde{\Omega}_c\sqrt{d_0}\mathbb{B}\vec{a}(u,\tilde{t}) & (4.13) \\ iu\vec{a}(u,\tilde{t}) - \vec{a}(\tilde{z}=0,\tilde{t}) = -\dfrac{1}{2}\tilde{\Omega}_c\sqrt{d_0}\mathbb{B}\vec{\sigma}_{gs}(u,\tilde{t}) - \dfrac{1}{2}d_0\mathbb{B}^2\vec{a}(u,\tilde{t}) & (4.14) \end{cases}$$

using the property of the Laplace transform about derivatives, $\mathscr{L}(\frac{df}{dz})(u) = iu\mathscr{L}(f)(u) - f(0^+)$. First, we consider the storage part ($\tilde{t} < 0$) where $\vec{a}(\tilde{z}=0,\tilde{t}<0) = \vec{a}_{\mathrm{in}}(\tilde{t})$ is the initial pulse before interacting with the atoms. These two differential equations can be written as:

$$\begin{cases} \dfrac{\partial}{\partial\tilde{t}}\vec{\sigma}_{gs}(u,\tilde{t}) = \mathbb{N}(u)\vec{\sigma}_{gs}(u,\tilde{t}) + \mathbb{Q}(u)\vec{a}_{\mathrm{in}}(\tilde{t}) & (4.15) \\ \vec{a}(u,\tilde{t}) = \mathbb{Q}(u)\vec{\sigma}_{gs}(u,\tilde{t}) + \mathbb{T}^{-1}(u)\vec{a}_{\mathrm{in}}(\tilde{t}) & (4.16) \end{cases}$$

with the matrices $\mathbb{T}(u) = iu + \frac{1}{2}d_0\mathbb{B}^2$, $\mathbb{Q}(u) = -\frac{1}{2}\tilde{\Omega}_c\sqrt{d_0}\mathbb{T}^{-1}(u)\mathbb{B}$ and $\mathbb{N}(u) = -\frac{1}{2}\tilde{\Omega}_c^2 + \frac{1}{4}\tilde{\Omega}_c^2 d_0\mathbb{B}\mathbb{T}^{-1}(u)\mathbb{B}$. The solution to this first order differential equation (4.15) is found by applying a well-known method called variation of constants. At the end of the storage time ($\tilde{t} = 0$), the spin-wave operator is equal to:

$$\vec{\sigma}_{gs}(u,0) = \int_{-\infty}^{0} \mathbb{M}^{\intercal}[-\tilde{t},u]\vec{a}_{\text{in}}(\tilde{t})d\tilde{t} \tag{4.17}$$

where we introduce the transfer matrix $\mathbb{M}[\tilde{t},u] = \mathbb{Q}(u)e^{\mathbb{N}(u)\tilde{t}}$. The retrieval process happens at $\tilde{t} > 0$. Equations (4.15) and (4.16) can be expressed without the input field $\vec{a}_{\text{in}}$ as $\vec{a}(\tilde{z} = 0, \tilde{t} > 0) = 0$. It leads to $\vec{a}(u, \tilde{t} > 0) = \mathbb{M}[\tilde{t},u]\vec{\sigma}_{gs}(u,0)$. The output pulse $\vec{a}_{\text{out}}(\tilde{t}) = \vec{a}(\tilde{z} = 1, \tilde{t} > 0)$ is calculated via the inverse Laplace transform $\vec{a}_{\text{out}}(\tilde{t}) = \mathscr{L}^{-1}(\vec{a}(u, \tilde{t} > 0))(\tilde{z} = 1)$:

$$\vec{a}_{\text{out}}(\tilde{t}) = \frac{1}{2\pi i}\int_{-\infty}^{+\infty} \mathbb{M}[\tilde{t},u]e^{iu}\vec{\sigma}_{gs}(u,0)du. \tag{4.18}$$

The storage-and-retrieval efficiency is defined as:

$$\eta = \frac{\int_0^{+\infty} \vec{a}_{\text{out}}^{\dagger}(\tilde{t})\vec{a}_{\text{out}}(\tilde{t})d\tilde{t}}{\int_{-\infty}^{0} \vec{a}_{\text{in}}^{\dagger}(\tilde{t})\vec{a}_{\text{in}}(\tilde{t})d\tilde{t}}. \tag{4.19}$$

The intensity of the input pulse is normalized to 1. The final expression of η is thus given by injecting (4.18) and (4.17) into (4.19):

$$\eta = \frac{1}{4\pi^2}\int_0^{+\infty}d\tilde{t}_1\int_{-\infty}^{+\infty}du_1\int_{-\infty}^{+\infty}du_0\int_{-\infty}^{0}d\tilde{t}_2\int_{-\infty}^{0}d\tilde{t}_0\ \vec{a}_{\text{in}}^{\dagger}(\tilde{t}_2)\mathbb{M}^{*}[-\tilde{t}_2,u_1]\mathbb{M}_u^{\dagger}[\tilde{t}_1,u_1] \times \mathbb{M}_u[\tilde{t}_1,u_0]\mathbb{M}^{\intercal}[-\tilde{t}_0,u_0]\vec{a}_{\text{in}}(\tilde{t}_0) \tag{4.20}$$

with $\mathbb{M}_u[\tilde{t},u] = \mathbb{M}[\tilde{t},u]e^{iu}$. The next task is to compute numerically this expression in order to access to the memory efficiency for a set of different experimental parameters.

Numerical method to compute the storage-and-retrieval efficiency

The first matrix required to calculate all the others is the coupling matrix $\mathbb{B}$ whose elements are defined in (4.6). In these numerical simulations, the integrals are discretized into sums with steps and bounds of integration. These steps need to be small enough and bounds of integration high enough to approximate the infinite integrals. There are no theoretical rules to determine if these two criteria are respected. However, a good method to ensure their validity is to decrease the steps (or increase the bounds) and see how the results are modified: they shoud remain the same. Considering N Hermite-Gaussian modes, the dimension of the matrix $\mathbb{B}$ is N^2. Thanks to the coupling matrix, we can compute the matrices $\mathbb{T}(u) = iu + \frac{1}{2}d_0\mathbb{B}^2$, $\mathbb{Q}(u) = -\frac{1}{2}\tilde{\Omega}_c\sqrt{d_0}\mathbb{T}^{-1}(u)\mathbb{B}$ and $\mathbb{N}(u) = -\frac{1}{2}\tilde{\Omega}_c^2 + \frac{1}{4}\tilde{\Omega}_c^2 d_0\mathbb{B}\mathbb{T}^{-1}(u)\mathbb{B}$. These matrices depend on the momentum u. They lead to the transfer matrix $\mathbb{M}[\tilde{t},u] = \mathbb{Q}(u)e^{\mathbb{N}(u)\tilde{t}}$ which is a function of time $\tilde{t}$ and momentum u. In the simulations, we create a new

transfer matrix $\mathcal{M}$ containing the elements of $\mathbb{M}[\tilde{t}, u]$ evaluated for a range of time and momentum. For each mode, time is indexed on the columns of $\mathbb{M}$ and momentum on the rows. The time interval is defined as $[0, \tilde{t}_{\text{lim}}]$ with steps $\Delta\tilde{t}$ and the momentum interval as $[-u_{\text{lim}}, u_{\text{lim}}]$ with steps Δu. The dimension of $\mathcal{M}$ thus is $Nl_{\tilde{t}} \times Nl_u$ with $l_{\tilde{t}}$ and l_u the lengths of time and momentum intervals. As seen on the previous section, $\mathcal{M}_u$ is the matrix $\mathcal{M}$ including the factor e^{iu}. The memory efficiency expressed in (4.20) can be simply written as:

$$\eta = \frac{\Delta\tilde{t}^2\Delta u^2}{4\pi^2}\vec{a}_{\text{in}}^{\dagger}(\mathcal{M}^* \times \mathcal{M}_u^{\dagger} \times \mathcal{M}_u \times \mathcal{M}^{\intercal})\vec{a}_{\text{in}} \tag{4.21}$$

with $\vec{a}_{\text{in}}$ the vector representing the input temporal waveform of all the HG modes (the vector dimension is $Nl_{\tilde{t}}$). The integrals displayed in (4.20) are accounted for in the matrix products by the discretized sums over u and $\tilde{t}$. One can think that the prefactor must be $\Delta\tilde{t}^3\Delta u^2$ instead of $\Delta\tilde{t}^2\Delta u^2$ due to the five integrals. However, we chose a normalized input pulse intensity $\int_{-\infty}^{0}\vec{a}_{\text{in}}^{\dagger}(\tilde{t})\vec{a}_{\text{in}}(\tilde{t})d\tilde{t} = 1$ which includes the step $\Delta\tilde{t}$ after discretization. Therefore, the correct prefactor is $\Delta\tilde{t}^2\Delta u^2$.

Numerical simulations

The aim is to determine the memory efficiency using (4.21) for N Hermite-Gaussian modes to characterise the multimode capacity of our quantum memory. One issue I had to deal with was the required time to calculate the coupling matrix $\mathbb{B}$. Indeed, this triple integral of the HG profiles is costly in calculation time as the discretized steps need to be small enough to accurately represent all the peaks of high-order HG modes: a simulation for $N = 10$ modes lasts two days on a 50-core computer. The evaluation of the efficiency for 100 modes is not possible with this strategy, especially if one wants multiple versions of it for different parameters.

As a result, we only considered the diagonal modes HG_{kk} knowing that their divergence is higher than all the HG_{mn} modes with indices $m \leq k$ and $n \leq k$ (see expression (4.4)). For example, supposing that the efficiency of the mode HG_{11} is 80%, the memory can store and retrieve four modes (HG_{00}, HG_{01}, HG_{10} and HG_{11}) with an efficiency at least equals to 80% because the optical depth perceived by HG_{11} is lower than the others due to its divergence and waist.

This method enables to simulate the multimode capacity of our memory for a set of different peak optical depths d_0 on 100 modes as shown on figure 4.6. The data points correspond to the efficiency of the diagonal modes HG_{kk} ($k \in [0, 9]$) which is equivalent to the minimal efficiency among the $(k+1)^2$ modes HG_{mn} with indices $m \leq k$ and $n \leq k$. The waist of the fundamental Gaussian beam is set to $w_0 = 90\,\mu\text{m}$, the atomic waist to $\sigma = 600\,\mu\text{m}$, the length of the atomic ensemble to $L = 2\,\text{cm}$ and the Rabi frequency of the control beam to $\Omega_c = 2\Gamma$. The temporal shape of the signal pulse (included in $\vec{a}_{\text{in}}$) is chosen to be Gaussian to fit the shape of the EIT window. Its

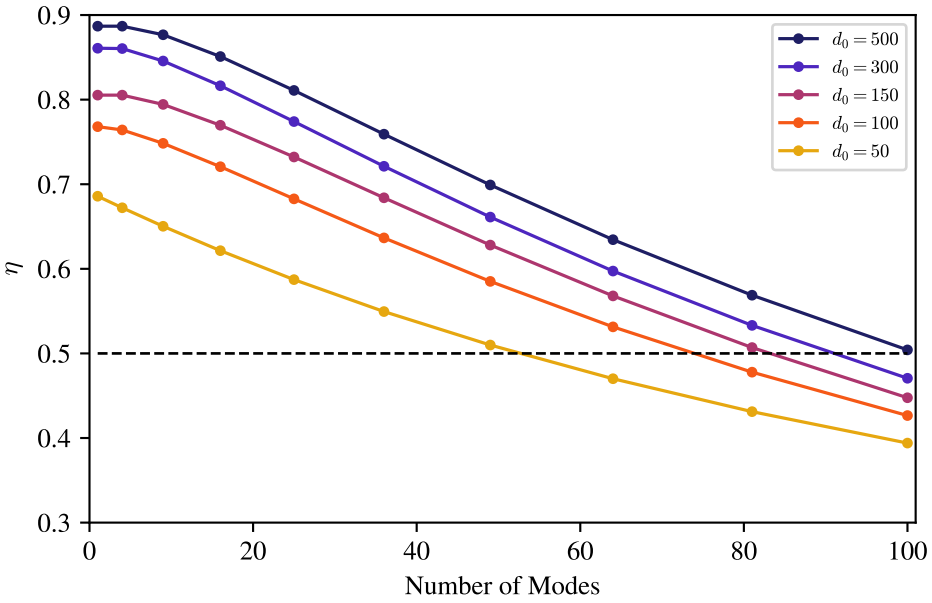

FIGURE 4.6: **Multimode capacity for a set of different peak optical depths d_0.** The data points correspond to the efficiency of the diagonal modes $\mathrm{HG}_{\mathrm{kk}}$ ($k \in [0, 9]$) which is equivalent to the minimal efficiency among the $(k+1)^2$ modes HG_{mn} with indices $m \leq k$ and $n \leq k$. The waist of the fundamental Gaussian beam is set to $w_0 = 90\,\mu$m, the atomic waist to $\sigma = 600\,\mu$m, the length of the atomic ensemble to $L = 2\,$cm and the Rabi frequency of the control beam to $\Omega_c = 2\Gamma$. The temporal shape of the signal pulse is chosen to be Gaussian and its FWHM is optimized to maximize the memory efficiency for this specific control Rabi frequency and for each peak optical depth. The black dashed line represents the 50 % threshold.

FWHM is optimized to maximize the memory efficiency for this specific control Rabi frequency and for each peak optical depth (see the section 1.2.3 for more details). For instance, the optimal width given by the simulation for $\Omega_c = 2\Gamma$ and $d_0 = 500$ is $\Delta t_{pulse} = 500\,$ns which is consistent with the optimal values found experimentally in the laboratory for this set of parameters. The black dashed line represents the 50 % threshold. One can define the multimode capacity C as the number of modes for which $\eta > 50\,\%$. On figure 2.7(b) in Chapter 2 (Cesium D1 line), the memory efficiency increases quite importantly with the optical depth for $d_0 \in [0, 100]$ and this fact is underlined by figure 4.6 with the evolution between $d_0 = 50$ and 100. The capacity goes from $C = 52$ modes for $d_0 = 50$ to $C = 74$ modes for $d_0 = 100$. It is improved to $C = 83$ for $d_0 = 150$, to $C = 91$ for $d_0 = 300$ and to $C = 101$ for $d_0 = 500$.

An interesting point to investigate is the optimization on the value of the signal waist w_0 as the size of the fundamental mode determines the size of every HG beam and their divergence. One can clearly see from figure 4.5 that the optimal w_0 to maximize the overlap between the signal and the atomic ensemble only depends on

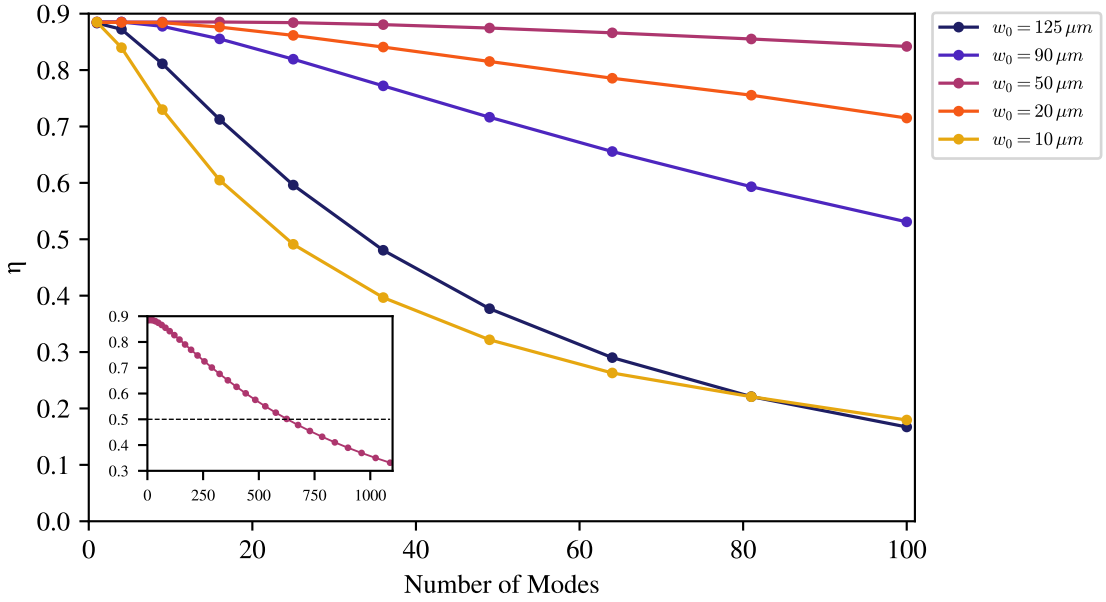

FIGURE 4.7: **Multimode capacity for a set of different signal waists w_0.** The data points correspond to the efficiency of the diagonal modes HG_{kk} ($k \in [0, 9]$ for the main figure and $k \in [0, 32]$ for the inset) which is equivalent to the minimal efficiency among the $(k+1)^2$ modes HG_{mn} with indices $m \leq k$ and $n \leq k$. The black dashed line is the 50 % threshold. The optical depth is set to $d_0 = 500$, the atomic waist to $\sigma = 600\,\mu$m, the length of the atomic ensemble to $L = 2\,$cm, the Rabi frequency of the control beam to $\Omega_c = 2\Gamma$ and the signal FWHM to $\Delta t_{pulse} = 500\,$ns. The inset exhibits a capacity $C = 625$ modes over the 50 % threshold for $w_0 = 50\,\mu$m.

the atomic waist σ and the length of the cloud L. In our simulation, σ and L are fixed and match the values of the characteristic transverse and longitudinal sizes of our experimental MOT: $\sigma = 600\,\mu$m and $L = 2\,$cm resulting in a Fresnel number $F = 18$. The multimode capacity has been computed for a set of different signal waists w_0 on figure 4.7. The optical depth is set to $d_0 = 500$, the Rabi frequency of the control beam to $\Omega_c = 2\Gamma$ and the signal FWHM to $\Delta t_{pulse} = 500\,$ns. First, the capacity is plotted for the current beam waist on the experiment $w_0 = 125\,\mu$m corresponding to $C = 34$ modes above $\eta = 50\,\%$. The waist is reduced to $90\,\mu$m, which increases the capacity to $C = 105$. Indeed, high-order HG beams are more focused inside the cloud in this case and achieve a better overlap with the atomic ensemble. Then, the best result is reached at $w_0 = 50\,\mu$m, with 100 modes stored-and-retrieved with an efficiency above $\eta_{100} = 84\,\%$ (η_{100} being the efficiency of the 100-th mode). However if we continues to decrease the waist, the divergence is becoming too important leading to leakage over the length of the cloud. This is exactly the phenomenon observed on figure 4.7, going from $\eta_{100} = 84\,\%$ for $w_0 = 50\,\mu$m to $\eta_{100} = 71\,\%$ for $20\,\mu$m and to $\eta_{100} = 17\,\%$ for $10\,\mu$m. As a result, there is a trade-off on the value of w_0: it needs to be small enough to fit in the center of the Gaussian atomic density but not too small as it results in higher divergence. One can note that the efficiency of the fundamental

mode remained the same among this set of waist values. The real difference is made on the high-order modes.

The comparison shows that $w_0 = 50\,\mu$m is the optimal waist among the set of values studied, given the geometry of the cloud chosen. Indeed, it led to the greatest capacity for 100 modes stored-and-retrieved with an efficiency at least equals to $\eta_{100} = 84\,\%$. I wanted to go a step further and compute the efficiency for higher number of modes. Therefore, a simulation was done for $\{HG_{kk}, k \in [0, 32]\}$ which is equivalent to 1089 modes (see the inset of figure 4.7). The inset exhibits $C = 625$ modes over the $50\,\%$ threshold. The difference between the results obtained for $w_0 = 125\,\mu$m ($C = 34$) and the one for $w_0 = 50\,\mu$m ($C = 625$) underlines the importance of the parameter w_0 on the multimode capacity of the quantum memory.

Another important topic to discuss is the cross-talks between modes. HG modes constitute an orthogonal basis, but their orthogonality is not preserved while they are stored in the memory due to the atomic density profile. The cross-talk between two orders (m, n) and (m', n') is the fractional power coupling from the mode (m, n) into the mode (m', n'). The mathematical definition is given by $B^2_{mn,m'n'}$, i.e. the square of the coupling term defined in (4.6). The highest cross-talk for these simulations is on the order of $10^{-4}\,\%$ and the mean value is $10^{-5}\,\%$. These low cross-talks are explained by the atomic density $n(x, y)$ that has small variations compared to the transverse structure of HG modes.

4.2 Multiplexing with a 2D array of micro-ensembles

In this section, we study another multiplexing technique based on Gaussian beams that are separated in space and addressing different areas of the atomic cloud (see figure 4.9). This approach has been first implemented in Kuzmich's group with an one-dimension array of micro-ensembles [Lan et al., 2009] and widely employed in Duan's group in two dimensions with the DLCZ scheme [Pu et al., 2017] and the EIT scheme [Jiang et al., 2019], albeit with low memory efficiency.

4.2.1 Generating a 2D array of light beams using AODs

One important task realised by Duan's group was to create a two-dimension array of Gaussian modes as presented on figure 4.9. All the Gaussian beams are not generated at the same time: one beam is displaced at specific positions on the transverse section of the cloud in the x and y directions thanks to two acousto-optic deflectors (AODs). The principle of AODs is the following: an acoustic wave propagates into a crystal and creates a grating that diffracts incident light. The diffracted orders k have a frequency $\omega + k\Omega$ where ω is the frequency of the incident light and Ω the one of the acoustic wave. In the case of their experiment, only the first order is used and its angle θ can be modified by changing Ω (the relation between these two parameters is

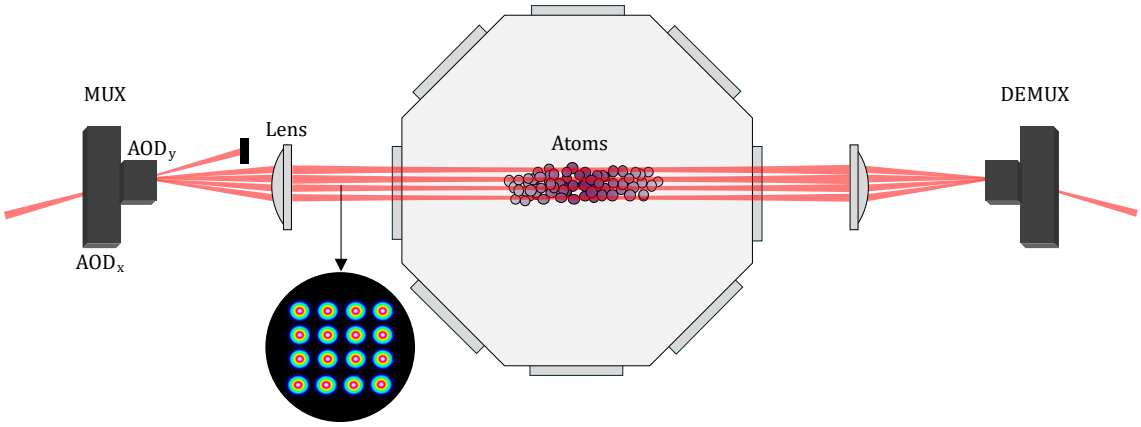

FIGURE 4.8: **Simplified setup of a spatially multiplexed quantum memory using two-dimensional AODs.** The signal beam is displaced at specific positions on the transverse section of the cloud in the x and y directions thanks to two acousto-optic deflectors (AODs). More specifically, the angle of the first diffraction order is controlled by the frequencies of the acoustic waves propagating inside the crystals of both AODs, and is mapped onto a micro-ensemble of the atomic cloud thanks to a lens. The control beam is also addressing individually the same micro-ensemble than the signal beam, thanks to two other AODs (not represented on the figure for clarity). Therefore, the read-out of the multiple spin-waves can be done separately and at different time.

$\theta \approx \lambda\Omega/v$ with v the speed of the sound wave in the crystal). One employs two AODs (one aligned on the x-axis and the other on the y-axis) and a lens, whose focal point is placed at the AODs position, to create a 2D array of parallel beams generated at different time as it is shown on figure 4.8. The frequency shift introduced by the two AODs is usually compensated by a double-pass acousto-optic modulator positioned before on the signal path. The control beam is also addressing individually the same areas of the cloud than the signal beam, thanks to two other AODs. Therefore, the read-out of the multiple spin-waves can be done separately and at different time. This feature is crucial as, after demultiplexing, all the paths are recombined into one and thus, the time difference between the output signal pulses coming from different micro-ensembles enables to distinguish them.

This multiplexing technique based on AODs is not only used in the field of quantum communication but also in quantum simulation [Bernien et al., 2017] and quantum computing [Debnath et al., 2016]. The next step is to evaluate the multimode capacity of our cold-atom based quantum memory with this method.

4.2.2 Multimode capacity of EIT-based quantum memory using separated memory cells

As a reminder, we define the multimode capacity C as the number of modes a quantum memory stores and retrieves with an efficiency above 50 %. The goal of this section is to find the optimal parameters which maximize C while maintaining

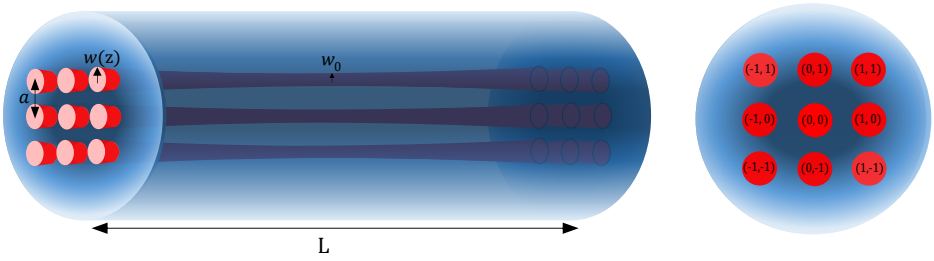

FIGURE 4.9: **Configuration for the 2D array of micro-ensembles.** The signal beams have a waist $w(z)$ (w_0 at $z = 0$) and are spaced by a length a in the x and y direction. The spacing value determines cross-talks between the spin-waves of neighboring micro-ensembles. The left figure represents the propagation of the Gaussian beams along the cloud and the one on the right is a view of the cloud transversal section. The beams are annotated by two indices defining the 2D array (m, n) (on this example $m, n \in \{-1, 0, 1\}$). As in the previous section, the atomic density has a Gaussian profile on the transverse axis x, y and is constant on the longitudinal axis z on a length L.

reasonable cross-talks between modes. The geometrical configuration of this problem is presented on figure 4.9. The signal beams have a waist $w(z)$ (w_0 at $z = 0$) and are spaced by a length a in the x and y direction. The spacing value determines cross-talks between the spin-waves of neighboring micro-ensembles. The left figure represents the propagation of the Gaussian beams along the cloud and the one on the right is a view of the cloud transversal section. The beams are annotated by two indices defining the 2D array (m, n) (on this example $m, n \in \{-1, 0, 1\}$). The atomic density has a Gaussian profile with an atomic waist σ on the transverse axis x, y and is constant on the longitudinal axis z on a length L.

The mathematical formalism is exactly the same than the one used to describe multiplexing with Hermite-Gaussian modes (see section 4.1.3). The only difference is the input signal which is a 2D array of Gaussian beams instead of a combination of HG functions. The modes composing the array can be written as:

$$E_{mn}(x, y, z) = u_m(x, z)u_n(y, z)e^{-ikz} \tag{4.22}$$

where u_j ($j = \{m, n\}$) is equal to

$$u_j(x, z) = \left(\frac{1}{q(z)}\right)^{\frac{1}{2}} e^{-i\frac{k(x-ja)^2}{2q(z)}} \tag{4.23}$$

with the complex beam parameter $q(z) = z + iz_R$, $z_R = \pi w_0^2/\lambda$ being the Rayleigh range. As before, the calculation of the coupling matrix $\mathbb{B}$ is quite long due to the triple integral over space (see relation (4.6)). Therefore, we need to define an efficient way to calculate it. If one looks at figure 4.9, the overlap between the mode $(0, 1)$ and the cloud is the same than for the mode $(-1, 0)$,$(0, -1)$ and $(1, 0)$ as the atomic density is Gaussian on the transverse section. If we extend this reasoning, the calculation of

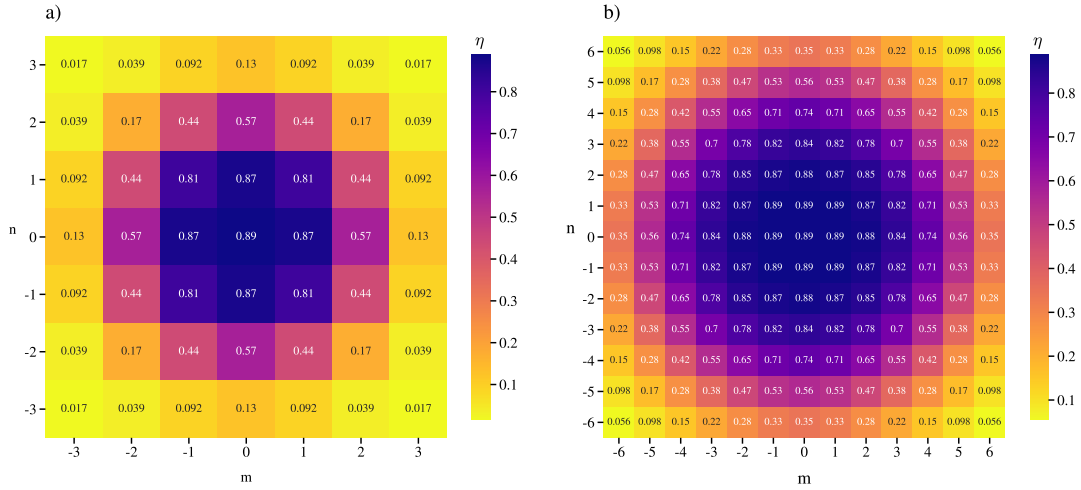

FIGURE 4.10: **Multimode capacity of EIT-based quantum memory using separated memory cells in the case of a compressed MOT.** This figure shows the storage-and-retrieval efficiency for a 2D array of micro-ensembles. The atomic waist is equal to $\sigma = 600\,\mu$m for a peak optical depth $d_0 = 500$. The length of the ensemble is set to $L = 2\,$cm, the Rabi frequency of the control beam to $\Omega_c = 2\Gamma$ and the signal FWHM to $\Delta t_{pulse} = 500\,$ns. The waist of each Gaussian beam is equal to $w_0 = 50\,\mu$m for figure a) and $w_0 = 20\,\mu$m for figure b). The spacing between modes is $a = 2.5\,w_0$ in the two directions (x and y) for a) and b). The multimode capacity, defined as the number of modes a quantum memory stores and retrieves with an efficiency above $50\,\%$, corresponds to $C = 13$ for a) and $C = 89$ for b).

the matrix $\mathbb{B}$ can be reduced to three modes instead of nine in the case illustrated on the figure (for example $(0,0)$,$(0,1)$ and $(1,1)$). The coupling matrix enables the computation of the transfer matrix $\mathcal{M}$ defined in the section 4.1.3. The memory efficiency is then determined using (4.21).

The simulations were performed in multiple configurations. The first case corresponds to a compressed MOT, i.e. a trap with a compression phase as described in 2.1.3. This phase enables to achieve a higher peak optical depth d_0 at the price of reducing the transverse size σ of the cloud. In this case, $\sigma = 600\,\mu$m and $d_0 = 500$ (the previous simulations using HG modes were performed in this configuration). The length of the ensemble is $L = 2\,$cm. The choice of the waist w_0 at $z = 0$ and the spacing a between the modes are crucial to achieve a high multimode capacity C while maintaining reasonable cross-talks between modes. Two configurations were tested: $w_0 = 50\,\mu$m with $a = 125\,\mu$m and $w_0 = 20\,\mu$m with $a = 50\,\mu$m. The results corresponding to these sets of parameters are presented on figure 4.10. The Rabi frequency of the control beam is set to $\Omega_c = 2\Gamma$ and the signal temporal length to $\Delta t_{pulse} = 500\,$ns (FWHM). This figure shows the storage-and-retrieval efficiency for a 2D array of micro-ensembles. The efficiency is maximal at the center of the cloud ($89\,\%$) and decreases when the micro-ensemble moves away from the center. The temporal shape of the signal pulse is chosen to be Gaussian to fit the shape of the EIT

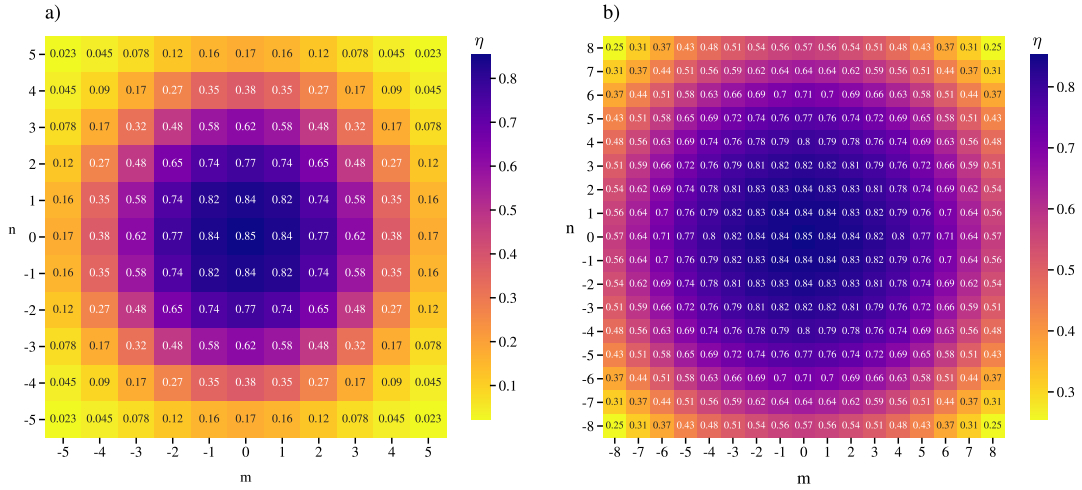

FIGURE 4.11: **Multimode capacity of EIT-based quantum memory using separated memory cells in the case of an uncompressed MOT.** This figure shows the storage-and-retrieval efficiency for a 2D array of micro-ensembles. The atomic waist is equal to $\sigma = 1.2\,\text{mm}$ for a peak optical depth $d_0 = 300$. The length of the ensemble is set to $L = 2\,\text{cm}$, the Rabi frequency of the control beam to $\Omega_c = 2\Gamma$ and the signal FWHM to $\Delta t_{pulse} = 350\,\text{ns}$. The waist of each Gaussian beam is equal to $w_0 = 50\,\mu\text{m}$ for figure *a*) and $w_0 = 20\,\mu\text{m}$ for figure *b*). The spacing between modes is $a = 2.5\,w_0$ in the two directions (x and y) for *a*) and *b*). The multimode capacity, defined as the number of modes a quantum memory stores and retrieves with an efficiency above 50 %, corresponds to $C = 37$ for *a*) and $C = 241$ for *b*).

window. Its width is optimized to maximize the memory efficiency given the values of control Rabi frequency and peak optical depth (see the section 1.2.3 for more details). As a result, the signal's temporal length is adapted to the beams crossing the center area of the cloud transverse section: the optical depths seen by these beams are close to the peak value d_0. The ones located at the borders thus experience two downsides: a low OD and high leakage of the signal pulse. These two factors are responsible for the evolution of the memory efficiency over the transverse plane. The multimode capacity, defined as the number of modes a quantum memory stores and retrieves with an efficiency above 50 %, is equal to $C = 13$ for the configuration $w_0 = 50\,\mu\text{m}$ with $a = 125\,\mu\text{m}$ and $C = 89$ for $w_0 = 20\,\mu\text{m}$ with $a = 50\,\mu\text{m}$.

The second case corresponds to an uncompressed MOT, i.e. a trap without a compression phase. The transverse size σ of the cloud is higher compared to the previous case at the price of reducing the peak optical depth d_0. We thus consider $\sigma = 1.2\,\text{mm}$ and $d_0 = 300$ for this uncompressed trap. The results are presented on figure 4.11. As mentioned earlier, the efficiency is maximal at the center of the cloud and decreases when the micro-ensemble moves away from the center. The peak efficiency (85 %) is lower compared to the compressed MOT as d_0 went from 500 to 300. However, the multimode capacity increased quite importantly: $C = 37$ for

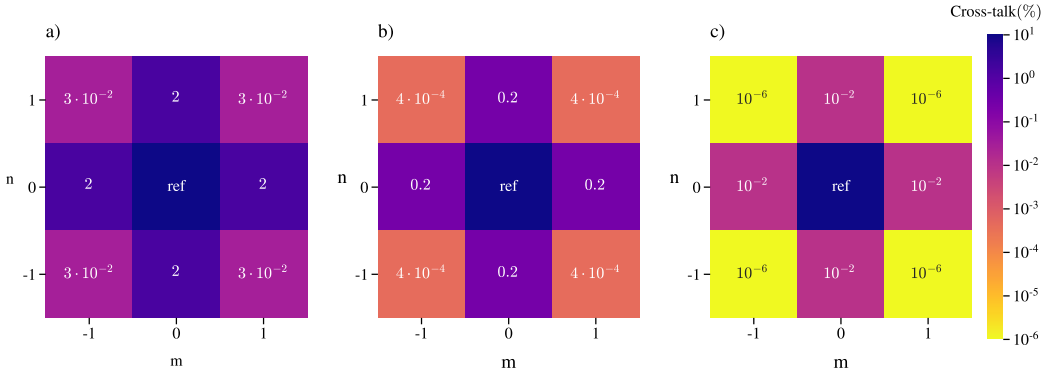

FIGURE 4.12: **Cross-talks between neighbouring cells for different spacing values.** This figure presents cross-talks of the micro-ensemble $(m = 0, n = 0)$ with its neighbouring cells. The waist of each Gaussian beam is $w_0 = 20\,\mu$m and the spacing value is $a = 2w_0$ for figure *a*), $a = 2.5w_0$ for figure *b*) and $a = 3w_0$ for figure *c*). The atomic waist is set to $\sigma = 1.2$ mm. Cross-talks with the four closest micro-ensembles $(m', n') = (0, 1),(1, 0),(0, -1)$ and $(-1, 0)$ are equal to 2 % for $a = 2w_0$, 0.2 % for $a = 2.5w_0$ and 0.01 % for $a = 3w_0$.

the configuration $w_0 = 50\,\mu$m with $a = 125\,\mu$m and $C = 241$ for $w_0 = 20\,\mu$m with $a = 50\,\mu$m. It is almost three times more than the previous results for both waist values.

One can increase the capacity C by reducing the spacing but at the price of increasing cross-talks. The cross-talk between two modes (m, n) and (m', n') is the fractional power coupling from the mode (m, n) into the mode (m', n'). The mathematical definition is given by $B^2_{mn,m'n'}$, i.e. the square of the coupling term defined in (4.6). Figure 4.12 presents cross-talks of the micro-ensemble $(m = 0, n = 0)$ with its neighbouring cells. The waist of each Gaussian beam is $w_0 = 20\,\mu$m and the spacing value is $a = 2w_0$ for figure *a*), $a = 2.5w_0$ for figure *b*) and $a = 3w_0$ for figure *c*). The atomic waist is set to $\sigma = 1.2$ mm. Cross-talks with the four closest micro-ensembles $(m', n') = (0, 1),(1, 0),(0, -1)$ and $(-1, 0)$ are equal to 2 % for $a = 2w_0$, 0.2 % for $a = 2.5w_0$ and 0.01 % for $a = 3w_0$. The optimal spacing value thus depends on the performances required by the experiment we are performing. For instance, in the context of the quantum money protocol, the best option would be to set the spacing at $a = 3w_0$ as the aim is to minimize cross-talks in order to reduce the error rate of the communication. The configuration $a = 2.5w_0$ is a good compromise to achieve a high multimode capacity and reasonable cross-talks.

The simulations were performed with a constant control Rabi frequency over space. In the real experiment using AODs, the control beam has a Gaussian profile with a small waist to independently address each micro-ensemble. If the control field overlaps a neighbouring memory cell, it creates additional cross-talks between the

different channels. However, only the tail of the control beam leaks on the closest modes leading to negligible EIT window and thus induces low cross-talks.

4.3 Conclusion

These simulated multimode capacities are promising for the future experiment. Multiplexing with superposed HG modes leads to a better capacity than the one with separated memory cells ($C = 625$ for Hermite-Gaussian modes with $w_0 = 50\,\mu$m compared to $C = 241$ for the 2D array of micro-ensembles with $w_0 = 20\,\mu$m and $a = 2.5w_0$ in the case of an uncompressed trap). This point could be explained by the geometry of our cloud which has a small transverse size and thus is more adapted to the storage of superposed beams than separated ones. Cross-talks are also higher for the 2D array of micro-ensembles (0.2 % between closest cells with $a = 2.5w_0$) than HG modes (maximum value: 10^{-4} %). However, MPLC devices create Hermite-Gaussian beams with non-negligible cross-talks (0.8 % in average, see section 4.1.2) and current Cailabs multiplexers are limited to 50 modes. Other experimental considerations may have to be taken into account in our model. Indeed, we also supposed the waist w_0 is centered compared to the atomic ensemble. Any experimental displacement between the focus of the beam and the center of the cloud leads to a weaker overlap and would result in a reduced capacity. The algorithm employed to produce the simulations can evaluate the impact of these imperfections on the final result. It will remain a useful tool for the team to establish a comparison with experimental data and try to understand which parameters are relevant to optimize the multimode capacity of our cold-atom based quantum memory.

CONCLUSION

Summary

This thesis reports the first demonstration of the unforgeable quantum money including an intermediate quantum memory layer. The cryptographic protocol was challenging to perform as a high-efficiency and low-noise storage platform is required to complete a secure transaction. The constraints are also very demanding on the fidelity of the qubits encoded. After optimizing the generation of random qubits and the properties of our cold-atom-based quantum memory, we reached the secure regime of the protocol.

We provided an overview of memory platforms in Chapter 1, with a specific focus on EIT-based quantum memories. The EIT scheme was illustrated with the dark state polariton picture demonstrating the adiabatic transfer from a photonic state to a collective excitation of the cloud. The decoherence of this excitation was assessed in the presence of residual magnetic fields and dephasing induced by atomic motion. After a reminder on magneto-optical traps, we explained how to achieve sub-Doppler temperatures thanks to polarization gradient cooling. In Chapter 2, we described the implementation of the cold-atomic ensemble in our setup with the new coils generating large magnetic field gradients. The memory efficiency was optimized by maximizing the optical depth of the medium and the EIT transmission at resonance. The lifetime measurement emphasized the good performances of the new current drivers cancelling the residual magnetic field. After optimizing the memory efficiency and lifetime, the cold-atomic ensemble had the required properties to be implemented as a memory layer in a quantum cryptographic protocol. Chapter 3 introduced the quantum money protocol and its security analysis. We succeeded to encode high-fidelity qubits thanks to the optimization of the sequence sent to the Pockels cell. One challenge was to maintain a good visibility for the Mach-Zehnder interferometer during the seven hours of data taking. We finally achieved the secure regime of the protocol by combining together all these efforts. The sources of noise in our experiment were identified and carefully analyzed. In Chapter 4, we performed

numerical simulations for two spatial multiplexing techniques. The simulated multimode capacities are promising for both methods. Multiplexing with superposed HG modes leads to a better capacity and lower cross-talks than the one with separated memory cells. However, MPLC devices create Hermite-Gaussian beams with non-negligible cross-talks and current commercial multiplexers are providing typically up to 50 modes.

Perspectives

Below, we outline two main directions we aim to explore further in the next years.

Implementation of spatial multiplexing
As described in Chapter 4, a critical challenge is to go beyond single-mode quantum memories and to store many modes at the same time. Several methods can be explored depending on the degree of freedoms available for a specific storage platform, such as multiplexing in time, frequency, and space. Spatial multiplexing is the best option for EIT-based memories. In the context of the quantum money protocol, an improvement of the experiment would be to store the whole sequence of random polarizations at once. Our group owns two Cailabs devices (one used as a multiplexer and the other employed to demultiplex) with 15 channels corresponding to 15 different Hermite-Gaussian modes. These MUX and DEMUX devices have been characterised but the interfacing with the cold-atom quantum memory has not yet been done due to time constraints. The aim would be to measure the efficiency achieved for these HG modes and the cross-talks between them. Spatial multiplexing using separated memory cells is another approach that is also considered in the future experiments as two-dimensional AODs can generate several hundred modes and the multimode capacity simulated in this case is promising.

Quantum repeater link demonstration
Our experiment is part of an European project called the Quantum Internet Alliance (QIA). The ultimate goal of this project is to create long distance quantum communications between different countries in Europe. One milestone is to implement a 50 km repeater link including two quantum memories, two entangled photon pair sources and one Bell-state measurement platform. The purpose of this implementation is to establish entanglement between the two QMs. One quantum memory will be located in our research laboratory and the other is provided by the start-up Welinq, a spin-off from our group hosted at Sorbonne Université. Both QMs are going to be based on a cold rubidium cloud. In a quantum network, the lifetime of QMs should at least be equal to the propagation time of light along the entire communication line. The memory lifetime required to perform a 50 km communication is thus in the range of $200\,\mu$s. In order to reach this targeted value, the decoherence induced by the residual magnetic field has to be suppressed. This can be done by applying Zeeman pumping

into a specific m_F level combined with magnetically insensitive clock transition. The pumping process is more effective for Rubidium atoms than Cesium as the ground state only contains three Zeeman levels ($F = 1$) instead of seven in the case of Cesium. The entangled photon pairs will be generated by type II SPDC sources that are under development in our team. One photon from the pair is going to be sent in free-space to the QMs at the wavelength compatible for storage (795 nm, Rubidium D1 line) and the other at telecom wavelength will be coupled to a 25 km fiber leading to the BSM platform. An important step is to interface the source with our cold-atom-based quantum memory.

APPENDIX A

APPENDIX

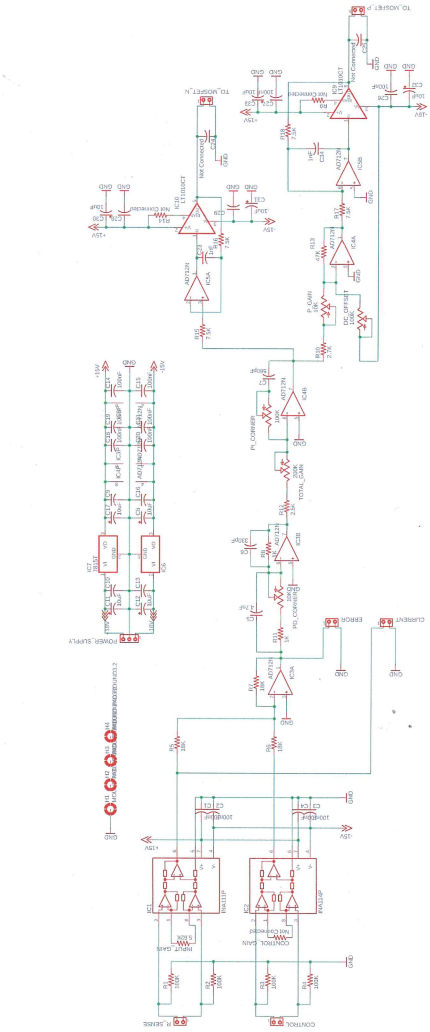

FIGURE A.1: Electronic circuit of the PID controllers used for the current drivers compensating the residual magnetic field. This circuit was designed in collaboration with the electronic workshop of our laboratory.

BIBLIOGRAPHY

Afzelius, M., Simon, C., de Riedmatten, H., & Gisin, N. (2009). Multimode quantum memory based on atomic frequency combs. *Phys. Rev. A*, *79*, 052329. https://doi.org/10.1103/PhysRevA.79.052329 (cit. on p. 13).

Afzelius, M., Usmani, I., Amari, A., Lauritzen, B., Walther, A., Simon, C., Sangouard, N., Minář, J., de Riedmatten, H., Gisin, N., & Kröll, S. (2010). Demonstration of atomic frequency comb memory for light with spin-wave storage. *Phys. Rev. Lett.*, *104*, 040503. https://doi.org/10.1103/PhysRevLett.104.040503 (cit. on p. 13).

Aspect, A., Dalibard, J., & Roger, G. (1982). Experimental test of bell's inequalities using time-varying analyzers. *Phys. Rev. Lett.*, *49*, 1804–1807. https://doi.org/10.1103/PhysRevLett.49.1804 (cit. on p. 1).

Bade, S., Denolle, B., Trunet, G., Riguet, N., Jian, P., Pinel, O., & Labroille, G. Fabrication and characterization of a mode-selective 45-mode spatial multiplexer based on multi-plane light conversion. In: In *2018 optical fiber communications conference and exposition (ofc)*. 2018, 1–3. https://doi.org/10.1364/OFC.2018.Th4B.3 (cit. on p. 98).

Bao, X.-H., Reingruber, A., Dietrich, P., Rui, J., Dück, A., Strassel, T., Li, L., Liu, N.-L., Zhao, B., & Pan, J.-W. (2012). Efficient and long-lived quantum memory with cold atoms inside a ring cavity. *Nature Physics*, *8*(7), 517–521. https://doi.org/10.1038/nphys2324 (cit. on p. 65).

Bernien, H., Schwartz, S., Keesling, A., Levine, H., Omran, A., Pichler, H., Choi, S., Zibrov, A. S., Endres, M., Greiner, M., Vuletić, V., & Lukin, M. D. (2017). Probing many-body dynamics on a 51-atom quantum simulator. *Nature*, *551*(7682), 579–584. https://doi.org/10.1038/nature24622 (cit. on p. 107).

Boller, K.-J., Imamoğlu, A., & Harris, S. E. (1991). Observation of electromagnetically induced transparency. *Phys. Rev. Lett.*, *66*, 2593–2596. https://doi.org/10.1103/PhysRevLett.66.2593 (cit. on p. 11).

Bouwmeester, D., Pan, J.-W., Mattle, K., Eibl, M., Weinfurter, H., & Zeilinger, A. (1997). Experimental quantum teleportation. *Nature*, *390*(6660), 575–579. https://doi.org/10.1038/37539 (cit. on p. 1).

Bozzio, M. (2019, December). *Security and implementation of advanced quantum cryptography : quantum money and quantum weak coin flipping* (Publication No. 2019SACLT045) [Theses]. Université Paris Saclay. https://pastel.hal.science/tel-03096433 (cit. on pp. 70, 73).

Bozzio, M., Diamanti, E., & Grosshans, F. (2019). Semi-device-independent quantum money with coherent states. *Phys. Rev. A*, *99*, 022336. https://doi.org/10.1103/PhysRevA.99.022336 (cit. on pp. 70, 71).

Bozzio, M., Orieux, A., Trigo Vidarte, L., Zaquine, I., Kerenidis, I., & Diamanti, E. (2018). Experimental investigation of practical unforgeable quantum money. *npj Quantum Information*, *4*(1), 5. https://doi.org/10.1038/s41534-018-0058-2 (cit. on pp. 70, 86).

Briegel, H.-J., Dür, W., Cirac, J. I., & Zoller, P. (1998). Quantum repeaters: The role of imperfect local operations in quantum communication. *Phys. Rev. Lett.*, *81*, 5932–5935. https://doi.org/10.1103/PhysRevLett.81.5932 (cit. on p. 2).

Cao, M., Hoffet, F., Qiu, S., Sheremet, A. S., & Laurat, J. (2020). Efficient reversible entanglement transfer between light and quantum memories. *Optica*, *7*(10), 1440–1444. https://doi.org/10.1364/OPTICA.400695 (cit. on pp. 11, 12, 46, 70).

Carter, W. H. (1980). Spot size and divergence for hermite gaussian beams of any order. *Appl. Opt.*, *19*(7), 1027–1029. https://doi.org/10.1364/AO.19.001027 (cit. on p. 96).

Choi, K. S., Deng, H., Laurat, J., & Kimble, H. J. (2008). Mapping photonic entanglement into and out of a quantum memory. *Nature*, *452*(7183), 67–71. https://doi.org/10.1038/nature06670 (cit. on p. 81).

Chu, S., Hollberg, L., Bjorkholm, J. E., Cable, A., & Ashkin, A. (1985). Three-dimensional viscous confinement and cooling of atoms by resonance radiation pressure. *Phys. Rev. Lett.*, *55*, 48–51. https://doi.org/10.1103/PhysRevLett.55.48 (cit. on p. 31).

Cirac, J. I., Zoller, P., Kimble, H. J., & Mabuchi, H. (1997). Quantum state transfer and entanglement distribution among distant nodes in a quantum network. *Phys. Rev. Lett.*, *78*, 3221–3224. https://doi.org/10.1103/PhysRevLett.78.3221 (cit. on p. 2).

Collins, O. A., Jenkins, S. D., Kuzmich, A., & Kennedy, T. A. B. (2007). Multiplexed memory-insensitive quantum repeaters. *Phys. Rev. Lett.*, *98*, 060502. https://doi.org/10.1103/PhysRevLett.98.060502 (cit. on p. 94).

Dalibard, J., & Cohen-Tannoudji, C. (1989). Laser cooling below the doppler limit by polarization gradients: Simple theoretical models. *J. Opt. Soc. Am. B*, *6*(11), 2023–2045. https://doi.org/10.1364/JOSAB.6.002023 (cit. on pp. 36, 37).

Debnath, S., Linke, N. M., Figgatt, C., Landsman, K. A., Wright, K., & Monroe, C. (2016). Demonstration of a small programmable quantum computer with atomic qubits. *Nature*, *536*(7614), 63–66. https://doi.org/10.1038/nature18648 (cit. on p. 107).

Dideriksen, K. B., Schmieg, R., Zugenmaier, M., & Polzik, E. S. (2021). Room-temperature single-photon source with near-millisecond built-in memory. *Nature Communications*, *12*(1), 3699. https://doi.org/10.1038/s41467-021-24033-8 (cit. on pp. 13, 30, 54).

Duan, L.-M., Lukin, M. D., Cirac, J. I., & Zoller, P. (2001). Long-distance quantum communication with atomic ensembles and linear optics. *Nature*, *414*(6862), 413–418. https://doi.org/10.1038/35106500 (cit. on p. 12).

Dudin, Y. O., Li, L., & Kuzmich, A. (2013). Light storage on the time scale of a minute. *Phys. Rev. A*, *87*, 031801. https://doi.org/10.1103/PhysRevA.87.031801 (cit. on p. 11).

Duranti, S., Wengerowsky, S., Feldmann, L., Seri, A., Casabone, B., & de Riedmatten, H. (2023). Efficient cavity-assisted storage of photonic qubits in a solid-state quantum memory. https://doi.org/10.48550/arXiv.2307.03509 (cit. on p. 13).

Eckel, S., Barker, D. S., Norrgard, E. B., & Scherschligt, J. (2022). Pylcp: A python package for computing laser cooling physics. *Computer Physics Communications*, *270*, 108166. https://doi.org/https://doi.org/10.1016/j.cpc.2021.108166 (cit. on p. 37).

England, D. G., Michelberger, P. S., Champion, T. F. M., Reim, K. F., Lee, K. C., Sprague, M. R., Jin, X.-M., Langford, N. K., Kolthammer, W. S., Nunn, J, & Walmsley, I. A. (2012). High-fidelity polarization storage in a gigahertz bandwidth quantum memory. *Journal of Physics B: Atomic, Molecular and Optical Physics*, *45*(12), 124008. https://doi.org/10.1088/0953-4075/45/12/124008 (cit. on p. 12).

Feynman, R. P. (1982). Simulating physics with computers. *International Journal of Theoretical Physics*, *21*(6), 467–488. https://doi.org/10.1007/BF02650179 (cit. on p. 1).

Fleischhauer, M., & Lukin, M. D. (2000). Dark-state polaritons in electromagnetically induced transparency. *Phys. Rev. Lett.*, *84*, 5094–5097. https://doi.org/10.1103/PhysRevLett.84.5094 (cit. on pp. 11, 22, 23).

Freedman, S. J., & Clauser, J. F. (1972). Experimental test of local hidden-variable theories. *Phys. Rev. Lett.*, *28*, 938–941. https://doi.org/10.1103/PhysRevLett.28.938 (cit. on p. 1).

Giner, L. (2013). *Etude de la transparence électromagnétiquement induite dans un ensemble d'atomes froids et application aux mémoires quantiques* [PhD thesis]. Université Pierre et Marie Curie - Paris VI. (Cit. on pp. 40, 43).

Grodecka-Grad, A., Zeuthen, E., & Sørensen, A. S. (2012). High-capacity spatial multimode quantum memories based on atomic ensembles. *Phys. Rev. Lett.*,

109, 133601. https://doi.org/10.1103/PhysRevLett.109.133601 (cit. on pp. 99, 101).

Grover, L. K. A fast quantum mechanical algorithm for database search. In: In *Proceedings of the twenty-eighth annual acm symposium on theory of computing*. STOC '96. Philadelphia, Pennsylvania, USA: Association for Computing Machinery, 1996, 212–219. ISBN: 0897917855. https://doi.org/10.1145/237814.237866 (cit. on p. 1).

Guan, J.-Y., Arrazola, J. M., Amiri, R., Zhang, W., Li, H., You, L., Wang, Z., Zhang, Q., & Pan, J.-W. (2018). Experimental preparation and verification of quantum money. *Phys. Rev. A*, *97*, 032338. https://doi.org/10.1103/PhysRevA.97.032338 (cit. on pp. 70, 86).

Harris, S. E., & Yamamoto, Y. (1998). Photon switching by quantum interference. *Phys. Rev. Lett.*, *81*, 3611–3614. https://doi.org/10.1103/PhysRevLett.81.3611 (cit. on p. 22).

Hau, L. V., Harris, S. E., Dutton, Z., & Behroozi, C. H. (1999). Light speed reduction to 17 metres per second in an ultracold atomic gas. *Nature*, *397*(6720), 594–598. https://doi.org/10.1038/17561 (cit. on p. 20).

Heshami, K., England, D. G., Humphreys, P. C., Bustard, P. J., Acosta, V. M., Nunn, J., & Sussman, B. J. (2016). Quantum memories: emerging applications and recent advances. *J. Mod. Opt.*, *63*, 2005 (cit. on p. 69).

Hoffet, F. (2022, March). *Highly-efficient entanglement transfer into and out of cold-atom quantum memories* (Publication No. 2022SORUS144) [Theses]. Sorbonne Université. https://theses.hal.science/tel-03813606 (cit. on pp. 38, 40, 53).

Horsley, A., Du, G.-X., Pellaton, M., Affolderbach, C., Mileti, G., & Treutlein, P. (2013). Imaging of relaxation times and microwave field strength in a microfabricated vapor cell. *Phys. Rev. A*, *88*, 063407. https://doi.org/10.1103/PhysRevA.88.063407 (cit. on p. 66).

Hsiao, Y.-F., Tsai, P.-J., Chen, H.-S., Lin, S.-X., Hung, C.-C., Lee, C.-H., Chen, Y.-H., Chen, Y.-F., Yu, I. A., & Chen, Y.-C. (2018). Highly efficient coherent optical memory based on electromagnetically induced transparency. *Phys. Rev. Lett.*, *120*, 183602. https://doi.org/10.1103/PhysRevLett.120.183602 (cit. on p. 46).

Hänsch, T., & Schawlow, A. (1975). Cooling of gases by laser radiation. *Optics Communications*, *13*(1), 68–69. https://doi.org/https://doi.org/10.1016/0030-4018(75)90159-5 (cit. on p. 31).

Jenkins, S. D., Zhang, T, & Kennedy, T. A. B. (2012). Motional dephasing of atomic clock spin waves in an optical lattice. *Journal of Physics B: Atomic, Molecular and Optical Physics*, *45*(12), 124005. https://doi.org/10.1088/0953-4075/45/12/124005 (cit. on pp. 31, 65).

Jiang, N., Pu, Y.-F., Chang, W., Li, C., Zhang, S., & Duan, L.-M. (2019). Experimental realization of 105-qubit random access quantum memory. *npj Quantum*

Information, *5*(1), 28. https://doi.org/10.1038/s41534-019-0144-0 (cit. on pp. 11, 94, 106).

Jobez, P, Usmani, I, Timoney, N, Laplane, C, Gisin, N, & Afzelius, M. (2014). Cavity-enhanced storage in an optical spin-wave memory. *New Journal of Physics*, *16*(8), 083005. https://doi.org/10.1088/1367-2630/16/8/083005 (cit. on p. 13).

Jobez, P., Timoney, N., Laplane, C., Etesse, J., Ferrier, A., Goldner, P., Gisin, N., & Afzelius, M. (2016). Towards highly multimode optical quantum memory for quantum repeaters. *Phys. Rev. A*, *93*, 032327. https://doi.org/10.1103/PhysRevA.93.032327 (cit. on pp. 13, 94).

Kent, A., & Pitalúa-García, D. (2020). Flexible quantum tokens in spacetime. *Phys. Rev. A*, *101*, 022309. https://doi.org/10.1103/PhysRevA.101.022309 (cit. on p. 70).

Kimble, H. J. (2008). The quantum internet. *Nature*, *453*(7198), 1023–1030. https://doi.org/10.1038/nature07127 (cit. on pp. 9, 69).

Lago-Rivera, D., Grandi, S., Rakonjac, J. V., Seri, A., & de Riedmatten, H. (2021). Telecom-heralded entanglement between multimode solid-state quantum memories. *Nature*, *594*(7861), 37–40. https://doi.org/10.1038/s41586-021-03481-8 (cit. on pp. 13, 94).

Lan, S.-Y., Radnaev, A. G., Collins, O. A., Matsukevich, D. N., Kennedy, T. A. B., & Kuzmich, A. (2009). A multiplexed quantum memory. *Opt. Express*, *17*(16), 13639–13645. https://doi.org/10.1364/OE.17.013639 (cit. on p. 106).

Laurat, J., de Riedmatten, H., Felinto, D., Chou, C.-W., Schomburg, E. W., & Kimble, H. J. (2006). Efficient retrieval of a single excitation stored in an atomic ensemble. *Opt. Express*, *14*(15), 6912–6918. https://doi.org/10.1364/OE.14.006912 (cit. on p. 12).

Lett, P. D., Watts, R. N., Westbrook, C. I., Phillips, W. D., Gould, P. L., & Metcalf, H. J. (1988). Observation of atoms laser cooled below the doppler limit. *Phys. Rev. Lett.*, *61*, 169–172. https://doi.org/10.1103/PhysRevLett.61.169 (cit. on p. 36).

Lin, Y.-W., Chou, H.-C., Dwivedi, P. P., Chen, Y.-C., & Yu, I. A. (2008). Using a pair of rectangular coils in the mot for the production of cold atom clouds with large optical density. *Opt. Express*, *16*(6), 3753–3761. https://doi.org/10.1364/OE.16.003753 (cit. on p. 42).

Liu, C., Dutton, Z., Behroozi, C. H., & Hau, L. V. (2001). Observation of coherent optical information storage in an atomic medium using halted light pulses. *Nature*, *409*(6819), 490–493. https://doi.org/10.1038/35054017 (cit. on p. 11).

Lo, H.-K., & Preskill, J. (2005). Phase randomization improves the security of quantum key distribution. (Cit. on p. 73).

Lukin, M. D., & Imamoglu, A. (2000). Nonlinear optics and quantum entanglement of ultraslow single photons. *Phys. Rev. Lett.*, *84*, 1419–1422. https://doi.org/10.1103/PhysRevLett.84.1419 (cit. on p. 22).

Ma, L., Lei, X., Yan, J., Li, R., Chai, T., Yan, Z., Jia, X., Xie, C., & Peng, K. (2022). High-performance cavity-enhanced quantum memory with warm atomic cell. *Nature Communications*, *13*(1), 2368. https://doi.org/10.1038/s41467-022-30077-1 (cit. on p. 12).

Macfarlane, R. M. (2002). High-resolution laser spectroscopy of rare-earth doped insulators: A personal perspective. *Journal of Luminescence*, *100*(1), 1–20. https://doi.org/https://doi.org/10.1016/S0022-2313(02)00450-7 (cit. on p. 13).

Massar, S., & Popescu, S. (1995). Optimal extraction of information from finite quantum ensembles. *Phys. Rev. Lett.*, *74*, 1259–1263. https://doi.org/10.1103/PhysRevLett.74.1259 (cit. on p. 10).

Molina, A., Vidick, T., & Watrous, J. Optimal counterfeiting attacks and generalizations for wiesner's quantum money (K. Iwama, Y. Kawano, & M. Murao, Eds.). In: *Theory of quantum computation, communication, and cryptography* (K. Iwama, Y. Kawano, & M. Murao, Eds.). Ed. by Iwama, K., Kawano, Y., & Murao, M. Berlin, Heidelberg: Springer Berlin Heidelberg, 2013, 45–64. ISBN: 978-3-642-35656-8 (cit. on p. 75).

Morizur, J.-F., Nicholls, L., Jian, P., Armstrong, S., Treps, N., Hage, B., Hsu, M., Bowen, W., Janousek, J., & Bachor, H.-A. (2010). Programmable unitary spatial mode manipulation. *J. Opt. Soc. Am. A*, *27*(11), 2524–2531. https://doi.org/10.1364/JOSAA.27.002524 (cit. on p. 97).

Namazi, M., Kupchak, C., Jordaan, B., Shahrokhshahi, R., & Figueroa, E. (2017a). Ultralow-noise room-temperature quantum memory for polarization qubits. *Phys. Rev. Appl.*, *8*, 034023. https://doi.org/10.1103/PhysRevApplied.8.034023 (cit. on pp. 30, 54).

Namazi, M., Vallone, G., Jordaan, B., Goham, C., Shahrokhshahi, R., Villoresi, P., & Figueroa, E. (2017b). Free-space quantum communication with a portable quantum memory. *Phys. Rev. Appl.*, *8*, 064013. https://doi.org/10.1103/PhysRevApplied.8.064013 (cit. on p. 69).

Nicolas, A., Veissier, L., Giner, L., Giacobino, E., Maxein, D., & Laurat, J. (2014). A quantum memory for orbital angular momentum photonic qubits. *Nature Photonics*, *8*(3), 234–238. https://doi.org/10.1038/nphoton.2013.355 (cit. on p. 94).

Nicolas, A. (2014, September). *Optical quantum memories with cold atomic ensembles : a free space implementation for multimode storage, or a nanofiber-based one for high collection efficiency* (Publication No. 2014PA066494) [Theses]. Université Pierre et Marie Curie - Paris VI. https://theses.hal.science/tel-01127631 (cit. on p. 40).

Ortu, A., Holzäpfel, A., Etesse, J., & Afzelius, M. (2022). Storage of photonic time-bin qubits for up to 20 ms in a rare-earth doped crystal. *npj Quantum Information*, *8*(1), 29. https://doi.org/10.1038/s41534-022-00541-3 (cit. on p. 13).

Petrich, W., Anderson, M. H., Ensher, J. R., & Cornell, E. A. (1994). Behavior of atoms in a compressed magneto-optical trap. *J. Opt. Soc. Am. B*, *11*(8), 1332–1335. https://doi.org/10.1364/JOSAB.11.001332 (cit. on p. 44).

Pu, Y.-F., Jiang, N., Chang, W., Yang, H.-X., Li, C., & Duan, L.-M. (2017). Experimental realization of a multiplexed quantum memory with 225 individually accessible memory cells. *Nature Communications*, *8*(1), 15359. https://doi.org/10.1038/ncomms15359 (cit. on pp. 12, 94, 106).

Raab, E. L., Prentiss, M., Cable, A., Chu, S., & Pritchard, D. E. (1987). Trapping of neutral sodium atoms with radiation pressure. *Phys. Rev. Lett.*, *59*, 2631–2634. https://doi.org/10.1103/PhysRevLett.59.2631 (cit. on p. 34).

Raimond, J.-M., & Perrin, H. (2020). Atoms and photons [Accessed 28-03-2024]. http://www-lpl.univ-paris13.fr/bec/bec/Teaching/m2icfpatomsphotons.pdf (cit. on p. 89).

Reim, K. F., Michelberger, P., Lee, K. C., Nunn, J., Langford, N. K., & Walmsley, I. A. (2011). Single-photon-level quantum memory at room temperature. *Phys. Rev. Lett.*, *107*, 053603. https://doi.org/10.1103/PhysRevLett.107.053603 (cit. on pp. 30, 54).

Reim, K. F., Nunn, J., Lorenz, V. O., Sussman, B. J., Lee, K. C., Langford, N. K., Jaksch, D., & Walmsley, I. A. (2010). Towards high-speed optical quantum memories. *Nature Photonics*, *4*(4), 218–221. https://doi.org/10.1038/nphoton.2010.30 (cit. on p. 12).

Richardson, D. J., Fini, J. M., & Nelson, L. E. (2013). Space-division multiplexing in optical fibres. *Nature Photonics*, *7*(5), 354–362. https://doi.org/10.1038/nphoton.2013.94 (cit. on p. 95).

Sangouard, N., Simon, C., de Riedmatten, H., & Gisin, N. (2011). Quantum repeaters based on atomic ensembles and linear optics. *Rev. Mod. Phys.*, *83*, 33–80. https://doi.org/10.1103/RevModPhys.83.33 (cit. on pp. 9, 51).

Schiansky, P., Kalb, J., Sztatecsny, E., Roehsner, M.-C., Guggemos, T., Trenti, A., Bozzio, M., & Walther, P. (2023). Demonstration of quantum-digital payments. *Nature Communications*, *14*(1), 3849. https://doi.org/10.1038/s41467-023-39519-w (cit. on p. 70).

Seri, A., Lago-Rivera, D., Lenhard, A., Corrielli, G., Osellame, R., Mazzera, M., & de Riedmatten, H. (2019). Quantum storage of frequency-multiplexed heralded single photons. *Phys. Rev. Lett.*, *123*, 080502. https://doi.org/10.1103/PhysRevLett.123.080502 (cit. on pp. 13, 94).

Shor, P. Algorithms for quantum computation: Discrete logarithms and factoring. In: In *Proceedings 35th annual symposium on foundations of computer science*. 1994, 124–134. https://doi.org/10.1109/SFCS.1994.365700 (cit. on p. 1).

Simon, J., Tanji, H., Thompson, J. K.,, familyi=c., given=Vladan, giveni=V., „ &. (2007). Interfacing collective atomic excitations and single photons. *Phys. Rev. Lett.*, *98*, 183601. https://doi.org/10.1103/PhysRevLett.98.183601 (cit. on p. 12).

Steck, D. A. (1998). *Cesium d line data* [Available at https://steck.us/alkalidata/ (revision 2.3.2, 10 September 2023)]. (Cit. on pp. 16, 28, 52).

Stefanov, A., Gisin, N., Guinnard, O., Guinnard, L., & Zbinden, H. (2000). Optical quantum random number generator. *Journal of Modern Optics*, *47*(4), 595–598. https://doi.org/10.1080/09500340008233380 (cit. on p. 79).

Tippenhauer, N. O., Pöpper, C., Rasmussen, K. B., & Capkun, S. On the requirements for successful gps spoofing attacks. In: In *Proceedings of the 18th acm conference on computer and communications security*. CCS '11. Chicago, Illinois, USA: Association for Computing Machinery, 2011, 75–86. ISBN: 9781450309486. https://doi.org/10.1145/2046707.2046719 (cit. on p. 70).

Urvoy, A, Carr, C, Ritter, R, Adams, C. S., Weatherill, K. J., & Löw, R. (2013). Optical coherences and wavelength mismatch in ladder systems. *Journal of Physics B: Atomic, Molecular and Optical Physics*, *46*(24), 245001. https://doi.org/10.1088/0953-4075/46/24/245001 (cit. on p. 89).

Veissier, L. (2013). *Quantum memory protocols in large cold atomic ensembles* [PhD thesis]. Université Pierre et Marie Curie - Paris VI. (Cit. on p. 40).

Vendeiro, Z. (2021). *Raman cooling to high phase space density* [PhD thesis]. Massachusetts Institute of Technology [p168]. https://hdl.handle.net/1721.1/142847 (cit. on p. 59).

Vernaz-Gris, P. (2018, January). *Preparation of large cold atomic ensembles and applications in efficient light-matter interfacing* (Publication No. 2018SORUS060) [Theses]. Sorbonne Université ; Australian national university. https://theses.hal.science/tel-02012964 (cit. on pp. 40, 64).

Vernaz-Gris, P., Huang, K., Cao, M., Sheremet, A. S., & Laurat, J. (2018). Highly-efficient quantum memory for polarization qubits in a spatially-multiplexed cold atomic ensemble. *Nature Communications*, *9*(1), 363. https://doi.org/10.1038/s41467-017-02775-8 (cit. on pp. 11, 46, 81).

Wang, X.-J., Yang, S.-J., Sun, P.-F., Jing, B., Li, J., Zhou, M.-T., Bao, X.-H., & Pan, J.-W. (2021). Cavity-enhanced atom-photon entanglement with subsecond lifetime. *Phys. Rev. Lett.*, *126*, 090501. https://doi.org/10.1103/PhysRevLett.126.090501 (cit. on p. 12).

Wang, Y., Li, J., Zhang, S., Su, K., Zhou, Y., Liao, K., Du, S., Yan, H., & Zhu, S.-L. (2019). Efficient quantum memory for single-photon polarization qubits. *Nature Photonics*, *13*(5), 346–351. https://doi.org/10.1038/s41566-019-0368-8 (cit. on pp. 11, 46).

Watrous, J. S. P. (2011). *Theory of quantum information (notes from fall 2011)* [https://cs.uwaterloo.ca/ watrous/LectureNotes.html]. (Cit. on p. 75).

Wiesner, S. (1983). Conjugate coding. *ACM Sigact News*, *15*, 78 (cit. on p. 70).

Wootters, W. K., & Zurek, W. H. (1982). A single quantum cannot be cloned. *Nature*, *299*(5886), 802–803. https://doi.org/10.1038/299802a0 (cit. on pp. 2, 70).

Xu, Z., Wu, Y., Tian, L., Chen, L., Zhang, Z., Yan, Z., Li, S., Wang, H., Xie, C., & Peng, K. (2013). Long lifetime and high-fidelity quantum memory of photonic polarization qubit by lifting zeeman degeneracy. *Phys. Rev. Lett.*, *111*, 240503. https://doi.org/10.1103/PhysRevLett.111.240503 (cit. on p. 65).

Zeuthen, E., Grodecka-Grad, A., & Sørensen, A. S. (2011). Three-dimensional theory of quantum memories based on Λ-type atomic ensembles. *Phys. Rev. A*, *84*, 043838. https://doi.org/10.1103/PhysRevA.84.043838 (cit. on p. 99).

Zhang, Z., Wang, X., & Lin, Q. (2009). A novel way for wavelength locking with acousto-optic frequency modulation. *Opt. Express*, *17*(12), 10372–10377. https://doi.org/10.1364/OE.17.010372 (cit. on p. 47).

Zhao, R., Dudin, Y. O., Jenkins, S. D., Campbell, C. J., Matsukevich, D. N., Kennedy, T. A. B., & Kuzmich, A. (2009). Long-lived quantum memory. *Nature Physics*, *5*(2), 100–104. https://doi.org/10.1038/nphys1152 (cit. on pp. 31, 65).

Hadriel MAMANN 17 Mai 2024

Sujet : Mémoire quantique optique efficace à base d'atomes froids servant de plateforme de stockage dans un protocole de cryptographie

Résumé : Une étape importante pour le développement des réseaux quantiques est de combiner les protocoles de cryptographie avec les mémoires quantiques afin d'établir des communications sécurisées où les informations peuvent être stockées et récupérées sur demande. Un cas d'utilisation possible de ces réseaux est d'effectuer des transactions authentifiées synchronisées par l'utilisation de mémoires. Cependant, les pertes et le bruit ajoutés par les dispositifs de stockage peuvent être exploités par des agents malveillants pour dissimuler leurs tentatives de fraude. Les contraintes pour opérer dans un régime sécurisé sont donc très exigeantes en termes d'efficacité et de fidélité de la mémoire. Cette thèse se concentre sur l'implémentation d'un ensemble d'atomes froids, utilisé en tant que mémoire quantique basée sur l'EIT, dans un protocole de cryptographie. Les ingrédients clés pour optimiser l'efficacité de stockage ainsi que la méthode employée pour atténuer les sources de décohérence sont détaillés. Ce travail représente la première démonstration du protocole cryptographique nommé "quatum money" incluant une étape intermédiaire de stockage, tirant parti de notre mémoire quantique hautement efficace et à faible bruit. L'étape suivante consisterait à multiplexer spatialement le nuage atomique afin de stocker toute la séquence de qubits aléatoires en une seule fois. Dans ce contexte, la capacité multimode de notre mémoire a été simulée numériquement en utilisant deux techniques différentes de multiplexage spatial.

Mots clés : Atomes froids, Mémoires quantiques, Réseaux quantiques, Protocoles de cryptographie quantique, Monnaie quantique, Multiplexage spatial

Subject: Cold-atomic ensemble implemented as an efficient optical quantum memory layer in a cryptographic protocol

Abstract: Combining cryptographic protocols with quantum memories is an important step for quantum network development in order to establish secure communications where information can be stored and retrieved on demand. One possible use case of these networks is to perform authenticated transactions synchronized by the use of memories. However, the losses and noise added by storage devices can be exploited by dishonest agents to hide their cheating attempts. The constraints to operate in a secure regime are thus very demanding in terms of memory efficiency and fidelity. This thesis focuses on the implementation of a cold-atomic ensemble used as an EIT-based quantum memory in a cryptographic protocol. The key ingredients to optimize the storage-and-retrieval efficiency and the method employed to mitigate the decoherence sources are detailed. This work reports the first demonstration of the unforgeable quantum money including an intermediate quantum memory layer, taking advantage of our highly-efficient and low-noise storage platform. The next step would be to spatially multiplex the atomic cloud in order to store the whole sequence of random qubits at once. In this scenario, the multimode capacity of our memory has been numerically simulated using two different spatial multiplexing techniques.

Keywords: Cold atoms, Quantum memories, Quantum networks, Quantum cryptographic protocols, Quantum money, Spatial multiplexing